ELSEVIER

Coordination Chemistry Reviews
204 (2000) 1–112

COORDINATION CHEMISTRY REVIEWS

www.elsevier.com/locate/ccr

Electron spin echo envelope modulation (ESEEM) spectroscopy as a tool to investigate the coordination environment of metal centers

Yiannis Deligiannakis [a,1], Maria Louloudi [b], Nick Hadjiliadis [b,*]

[a] *Institute of Materials Science, National Center for Scientific Research 'Demokritos', 15310 Aghia Paraskevi Atiikis, Greece*
[b] *Laboratory of General and Inorganic Chemistry, Department of Chemistry, University of Ioannina, 45110 Ioannina, Greece*

Received 1 April 1999; received in revised form 6 August 1999; accepted 27 August 1999

Contents

* Corresponding author. Tel.: +30-651-9-8420; fax: +30-651-4-4831.
[1] Also corresponding author.

PII: S0010-8545(99)00218-0

Abstract

The applications of electron spin echo envelope modulation (ESEEM) spectroscopy to study paramagnetic metal centers in metalloproteins and bioinorganic complexes are reviewed, with special attention to the novel spectroscopic techniques applied and the

structural information obtained. We summarize the physical principles and experimental techniques of ESEEM, the spectral shapes and the methods for their analysis. The physical meaning of the spin Hamiltonian parameters is highlighted in conjunction with their utilization for obtaining structural information.

Keywords: ESEEM; HYSCORE; Metalloproteins; ^{13}C, ^{15}N, ^{17}O

1. Introduction

For more than 30 years electron paramagnetic resonance (EPR) techniques have been major tools in efforts to characterize metal centers in model compounds or metalloenzyme active sites. Much of the information EPR provides about the composition, structure and bonding of paramagnetic metal centers, is obtained by analysis of hyperfine- and occasionally quadrupole-couplings that arise from interactions between the electron spin and the nuclear spin associated with either the ligands or nuclei from its immediate environment (e.g. $^{1}H(I=1/2)$, $^{14}N(I=1)$, $^{31}P(I=1/2)$, $^{19}F(I=1/2)$, $^{23}Na(I=3/2)$, $^{133}Cs(I=7/2)$). The treatise of Abragam and Bleaney [1] covers most aspects of the theory of the EPR of metal complexes, and is updated in the comprehensive textbook of Pilbrow [2].

An objective of the application of EPR to the study of paramagnetic centers is to determine, as fully as possible, the value of the various spin couplings — the hyperfine and quadrupole interactions — of the nuclei in the nearest environment of the center. Properly interpreted, the spin couplings provide a wealth of detailed information about the chemical, electronic, and molecular structure of the system under investigation. For powder or frozen solution samples, called polycrystalline or orientationally disordered samples, the EPR spectra are the envelope of elementary resonance lines, corresponding to all possible orientations of the paramagnetic centers with respect to the external magnetic field. The profile of a powder EPR spectrum is determined by several parameters, the most important being the symmetry of the **g** and **A** tensors, the values of their components and the linewidth. Quadrupole interactions, which are non-zero for nuclei with $I > 1/2$, usually have second order effects in the polycrystalline EPR spectra. In principle the hyperfine and quadrupole couplings are manifested as splitting in the EPR spectra.

However, the EPR spectra of metal compounds and metalloproteins are usually inhomogenously broadened [3]. Within the exception of single-crystal studies, nuclear hyperfine and quadrupole splitting are not resolved in the EPR spectra, see Fig. 1, and consequently the ensuing information is lost.

There are two EPR-based spectroscopies which can recover this information: (a) electron nuclear double resonance (ENDOR) [4,5] and (b) electron spin echo envelope modulation (ESEEM) [6,7]. In both ENDOR and ESEEM experiments, the nuclear transition (NMR) frequencies are monitored indirectly through EPR transitions. In the ESEEM experiment the NMR transitions are observed due to

mixing of the frequencies of the semi-forbidden and allowed EPR transitions, respectively [7,11], which have been coherently excited using short, intense microwave pulses. In contrast, in the ENDOR experiment the signal arises from the combined use of both microwave and radiofrequency irradiation which directly excites the EPR and the NMR transitions simultaneously. The ESEEM experiment is a time-domain experiment [7,11,12] while ENDOR is a frequency-domain experiment. Moreover, the ESEEM experiment always involves pulsed-EPR while both pulsed- and c.w. ENDOR are currently employed. Variants of these techniques, include coherent Raman beat [13,14] which results in modulation analogous to that obtained by three pulse ESEEM [13], and coherence-transfer Fourier transform pulsed-ENDOR (see Refs. [15,16] and references therein), but their practical applications have been fairly limited.

Although the shapes of ESEEM and ENDOR spectra generally differ [7–9], ESEEM and ENDOR give complementary information [10]: ESEEM is very well suited for measuring weak hyperfine couplings, e.g. of the order of the free nuclear Larmor frequency, while continuos wave ENDOR works better for strong hyperfine couplings. A typical example is the case of Cu^{2+}-imidazole complex, where X-band (9.0–9.5 GHz) ENDOR spectroscopy allows better resolution of the magnetic couplings for ^{14}N directly coordinated to Cu^{2+}, while X-band ESEEM is more appropriate for the weaker coupling of the remote ^{14}N of the imidazole. Weak nuclear couplings can also be resolved by Mims pulsed-ENDOR [16], or by the dead-time independent 'refocused' Mims (ReMims) ENDOR [17]. In this review we limit our consideration to ESEEM with the aim being to highlight its value in determining weak magnetic interactions in coordination compounds in metalloproteins and synthetic complexes.

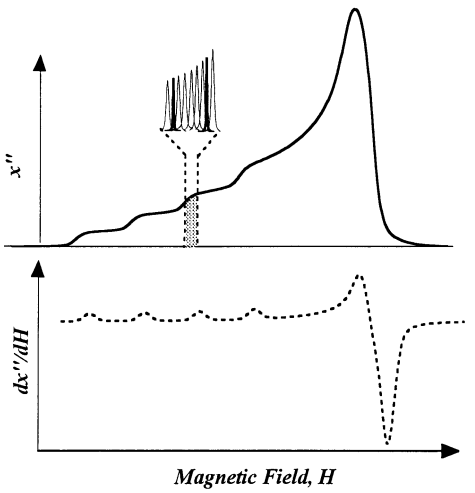

Fig. 1. Continuos wave (c.w.) EPR spectrum for a powder sample. Absorption (solid line), first derivative (dashed line). Part of the absorption spectrum is expanded, illustrating spin packets from individual centers that add together to give the inhomogenously broadened powder EPR pattern. The bold lines depict a pair of spin packets representing a hyperfine splitting of a $I = 1/2$ nucleus.

The principles, procedures and applications of ESEEM have been reviewed in the comprehensive book of Dikanov and Tsvetkov [7] and in Refs. [3,12,18–22]. The study of metalloproteins and model compounds by ESEEM, up to 1989, has been reviewed in Refs. [23–25]. These refer to one-dimensional ESEEM at frequencies around X-band, based on two- and three-pulse experiments.

The application of ESEEM to paramagnetic metals can be broadly classified into two categories. One concerns paramagnetic metal sites substituted on oxide surfaces to generate a catalytic reactive species, such as silica gel and zeolites — which are crystalline aluminisilicates — (for reviews see Refs. [26–28]). A second area, which is the subject of the review, concerns metals in biological systems, metalloproteins or bioinorganic compounds. In this article, we review the up-to-date applications of ESEEM in this area, including the application of four-pulse ESEEM, 2D-HYSCORE, high-field ESEEM, multifrequency-ESEEM spectroscopy and application of ESEEM to non-Kramer spin systems. Section 2 presents the background, fundamental physical principles and experimental aspects of ESEEM. Section 3 provides information about the methods used in the analysis of the spectra. The benefits of isotopic labeling and multifrequency ESEEM are discussed in Section 4. Section 5 outlines the utilization of the spin-Hamiltonian parameters in conjunction with structural information. Finally, in Section 6 a survey of the up-to-date published work is presented.

2. ESEEM background

2.1. Two-, three-, four-pulse ESEEM, HYSCORE

ESEEM experiments are performed by recording the echo intensity generated by a sequence of resonant microwave pulses, separated by evolution times i.e. periods where the microwave power is off; the recorded echo-envelope is the time-domain ESEEM signal. In the presence of nuclear spins weakly coupled with the electron-spin, the intensity of the echo is modulated at the nuclear transition frequencies of the interacting nucleus [6,7].

The standard one-dimensional ESEEM experiments, consist of two- and three-pulse sequences, Fig. 2, respectively. These are based on two kinds of echo, e.g. the primary- or the stimulated-echo for the two- and three-pulse, respectively, both discovered by Hahn [29]. The two-pulse ESEEM experiment was first introduced by Rowan, Hahn and Mims [6]; Mims subsequently further developed the theory and techniques [3,11] for two- and three-pulse ESEEM.

In the two-pulse experiment, Fig. 2(A), at time τ after the second pulse, an electron spin-echo is generated. The modulation envelope, obtained as τ is incremented, is related to the nuclear transition frequencies within an electron spin manifold; in addition, the sum and difference of the basic nuclear frequencies also appear in the two-pulse ESEEM. For nuclear spin $I = 1/2$, which is the simplest case, the expression for two-pulse ESEEM is [11]

Two-pulse: $E_{2p}(\tau)$

$$= -k/4[2 - 2\cos(\omega_\alpha\tau) - 2\cos(\omega_\beta\tau) + \cos((\omega_\alpha + \omega_\beta)\tau) + \cos((\omega_\alpha - \omega_\beta)\tau)] \quad (1)$$

where the modulation depth k [11,19] is

$$k = 4c^2s^2 \quad (2)$$

with c^2 and s^2 being the transition probabilities of the allowed and semi-forbidden transitions, respectively [19]

$$I_{\text{allowed}} = c^2\left|\frac{\omega_I^2 - (\omega_\alpha - \omega_\beta)^2/4}{\omega_\alpha\omega_\beta}\right| \quad (3a)$$

$$I_{\text{forb}} = s^2\left|\frac{\omega_I^2 - (\omega_\alpha + \omega_\beta)^2/4}{\omega_\alpha\omega_\beta}\right| \quad (3b)$$

For rhombic g- and A-tensors, which is often the case for metal centers, the fundamental nuclear frequencies are

$$\omega_{\alpha(\beta)} = 2\pi\sqrt{\{[m_s A_1 - \nu_I I_1]^2 + [m_s A_2 - \nu_I I_2]^2 + [m_s A_3 - \nu_I I_3]^2\}} \quad (4)$$

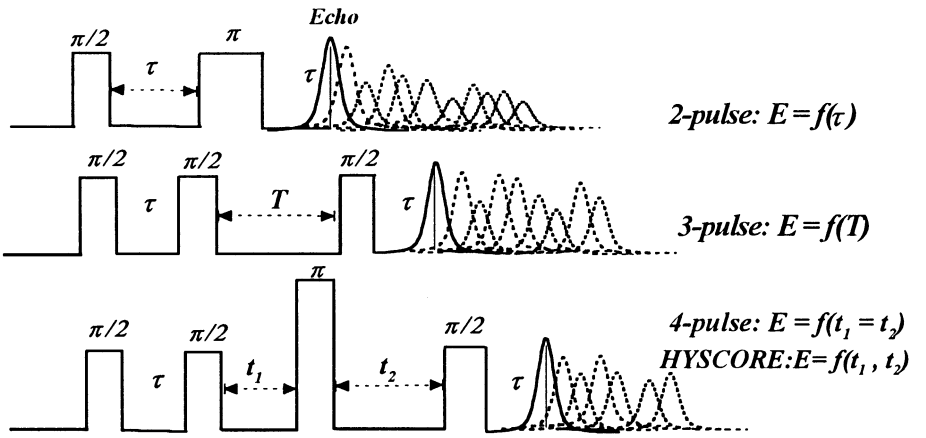

Fig. 2. Pulse sequences used for two-, three- and four-pulse ESEEM and HYSCORE experiments. In the two-pulse experiment at time τ after the second pulse, a spin echo is generated. The modulation envelope is obtained as τ is incremented. In the three-pulse sequence, two pulses separated by time τ are applied, followed by a third pulse after time T, and the stimulated-echo is observed at time τ after the third pulse. The echo envelope obtained as T is incremented. Four-pulse ESEEM and HYSCORE are based on a three-pulse sequence with an additional π-pulse applied between the second and third π/two-pulse. As in the three-pulse sequence, the first two π/two-pulses separated by the time interval t, generate nuclear coherences. Then, the π-pulse transfers populations from one M_S manifold to the other and mixes nuclear coherences in one M_S manifold with those of the other manifold. The last π/two-pulse leads to the formation of the stimulated echo. In the four pulse experiment the nuclear coherences evolve during the two variable time intervals t_1 and t_2, stepped under the constraint $t_1 = t_2 = T$. In the HYSCORE experiment the echo intensity is recorded as a function of the interpulse time t_1, e.g. between the time the second and third pulses, and t_2, e.g. between the time the third and fourth pulses.

where $m_s = +1/2$ and $-1/2$ correspond to the α and β spin manifolds, respectively. The direction cosines $(l_1, l_2, l_3) = (\sin\theta\ \cos\phi,\ \sin\theta,\ \sin\phi, \cos\theta)$ define the orientation of the laboratory magnetic field, $\boldsymbol{B}$, in the principal axis system of the g-tensor [30], Fig. 3.

$$\boldsymbol{B} = B(l_1, l_2, l_3) \tag{5}$$

The matrix of the hyperfine tensor $\boldsymbol{A}$ in its principal axes system is $\boldsymbol{A} = (A_1, A_2, A_3)$. Its particular form depends on the reference axis system. For systems where the g-anisotropy exceeds the anisotropy of the hyperfine interactions, the convenient reference axes system is that of principal axes of the $\boldsymbol{g}$-tensor. In the point-dipole approximation, the dipolar component is $|T| = g_n\beta_n\beta/hr^3$ where $r = |\boldsymbol{r}|$ is the effective electron–nucleus distance, and the hyperfine tensor may be expressed in the form [30]

$$A_i = \frac{T}{g_{eff}} \times \left\{ g_i l_i \left(g_i(3n_i^2 - 1) + \frac{A_{\mathrm{iso}}}{T} \right) + 3g_j^2 l_j n_i n_j + 3g_k^2 l_k n_i n_k \right\} \tag{6a}$$

where $i,\ j,\ k = 1,\ 2,\ 3\ (i \neq j \neq k)$ and $n_{i,j,k}$ are the direction cosines of the electron–nuclear vector $\boldsymbol{r}$, Fig. 3. The measured g-value is

$$g_{\mathrm{eff}} = \sqrt{(g_1 l_1)^2 + (g_2 l_2)^2 + (g_3 l_3)^2} \tag{6b}$$

The modulation depth parameter becomes [31]

$$k = \frac{4}{3} I(I+1) \left(\frac{v_I}{v_\alpha v_\beta} \right)^2 \{ [A_1 l_2 - A_2 l_1]^2 + [A_2 l_3 - A_3 l_2]^2 + [A_1 l_3 - A_3 l_1]^2 \} \tag{6c}$$

A major shortfall of the two-pulse method for metal spins, is that the phase memory time, T_{M}, is usually short thereby limiting the time when modulations can be obtained. In cases where the periodicity of the modulations is low or where the

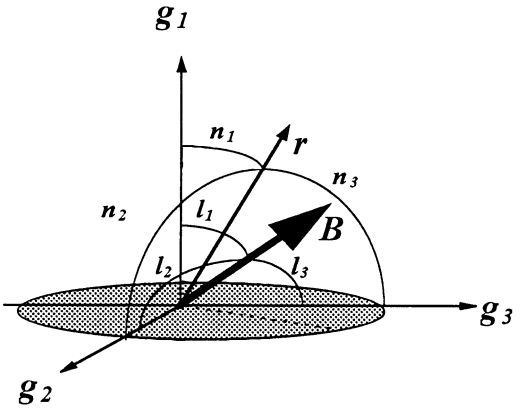

Fig. 3. Definition of the direction cosines (l_1, l_2, l_3) determining the vector of the external magnetic field $\boldsymbol{B}$, and (n_1, n_2, n_3) determining the electron–nuclear vector $\boldsymbol{r}$, both with respect to the principal axes system of the g-tensor.

modulations are quickly damped, the lines in the frequency-domain spectrum tend to be broad. With more than a single type of nucleus is coupled to the electron spin, spectral resolution may therefore be compromised [7]. Additionally, a small contact interaction may broaden lines. The two-pulse ESEEM spectra may thus be difficult to analyze.

An alternative procedure is one utilizing the three-pulse ESEEM experiment [11]. Here two pulses, separated by time τ, are applied followed by a third pulse after time T, and the stimulated echo is observed at time τ after the third pulse, Fig. 2. The echo envelope, obtained as T is incremented, is modulated by the nuclear transition frequencies of nuclei coupled with the electron spin; in contrast with the two-pulse experiment, no sums and differences of the basic nuclear frequencies are observed in the three-pulse ESEEM spectrum. For $I = 1/2$ the normalized three-pulse ESEEM is [11]

$$\text{Three-pulse: } E_{3p}(\tau, T)$$
$$= 1 - k/4\{[1 - \cos(\omega_\alpha \tau)][1 - \cos(\omega_\beta T)] + [1 - \cos(\omega_\beta \tau)][1 - \cos(\omega_\alpha T)]\} \quad (7)$$

where the various parameters have the same meaning and definitions as in the two-pulse case.

There are some advantages of the three-pulse over the two-pulse procedure. Most important is that the phase-memory limitations associated with the two-pulse experiment are largely obviated. Thus, modulations of the stimulated-echo envelope persist for longer times, leading to narrower lines in the frequency-domain spectrum. Another advantage is that the spectral lines in three-pulse ESEEM spectrum correspond to the nuclear frequencies, with no interference from their combination frequencies and this usually simplifies the spectrum.

Four-pulse ESEEM is based on a three-pulse sequence with an additional π-pulse applied between the second and third π/two-pulse, Fig. 2, [32]. As in the three-pulse sequence, the first two π/two-pulses separated by the time interval t, generate nuclear coherence [18,19]. Then, the π-pulse transfers populations from one M_S manifold to the other and mixes nuclear coherence in one M_S manifold with those of the other manifold. The nuclear coherences evolve during the two variable time intervals t_1 and t_2, stepped under the constraint $t_1 = t_2 = T$, [32] Fig. 2. The last $\pi/2$-pulse leads to the formation of the stimulated echo. At appropriate separation τ between the first two pulses, the four-pulse sequence may lead to deep modulations at the basic nuclear frequencies and higher harmonics corresponding to combinations of the basic nuclear frequencies and this is useful in estimating weak dipolar couplings [33–36]. For $I = 1/2$ the four-pulse ESEEM is given by the expression

$$\text{Four-pulse: } E_{4p}(\tau, T)$$
$$= 1 - k/4\{A + B(c^2 \cos[1/2(\omega_\alpha + \omega_\beta)(\tau + T)] + s^2 \cos[1/2(\omega_\alpha - \omega_\beta)(\tau + T)])$$
$$+ C_\alpha \cos[1/2\omega_\alpha(\tau + T)] + C_\beta \cos[1/2\omega_\beta(\tau + T)]\} \quad (8a)$$

where

$$A = 3 - \cos(\omega_\alpha \tau) - \cos(\omega_\alpha \tau) - s^2 \cos((\omega_\alpha + \omega_\beta)\tau) - c^2 \cos(\omega_\alpha - \omega_\beta)\tau) \quad (8b)$$

$$B = -4 \sin(1/2\omega_\alpha \tau) \sin(1/2\omega_\beta \tau) \quad (8c)$$

$$C_{\alpha(\beta)} = 2\{c^2 \cos[(\omega_{\beta(\alpha)} - \omega_{\alpha(\beta)}/2)\tau] + s^2 \cos[(\omega_{\alpha(\beta)} + \omega_{\beta(\alpha)}/2)\tau] + \cos(1/2\omega_{\alpha(\beta)}\tau)\} \quad (8d)$$

The four-pulse ESEEM is currently used to measure 'combination frequencies', i.e. the sum $(\omega_\alpha + \omega_\beta)$, or difference $(\omega_\alpha - \omega_\beta)$ of basic nuclear transition frequencies in different M_S manifolds of the electron spin [33–36]. In disordered systems the basic nuclear transition frequencies are often broad and weak, that is difficult to resolve. In both two- and four-pulse ESEEM, combination peaks appear as narrow features in the spectrum, since orientation-dependent hyperfine interactions are partially refocused [33,34]. The four-pulse procedure is more advantageous for measuring combination lines than the two-pulse since it is free from phase-memory limitations, but also suffers from τ-dependent blind spots [25,32]. To overcome this problem, a blind-spot free two-dimensional ESEEM method for measuring sum combination-frequencies has recently been developed [37].

HYperfine Sublevel COrRElation spectroscopy (HYSCORE) is a two-dimensional ESEEM technique based on a four-pulse sequence, see Fig. 2, introduced by Höfer et al. [38]. The π-pulse exchanges the nuclear coherences from one M_S manifold to another [18,19]. The nuclear coherences evolve during the time intervals t_1 and t_2, which are stepped independently. The echo intensity is recorded as a function of the interpulse time t_1, i.e. the time between the second and third pulses, and t_2, i.e. the time between the third and fourth pulses. The frequency-domain HYSCORE, obtained after Fourier transforming the time-domain spectrum in both dimensions, e.g. t_1 and t_2, contains cross-peaks which provide correlations between nuclear transitions from the different M_S manifolds [19,38]. For $S = 1/2$, $I = 1/2$ the expression of the time-domain HYSCORE related to the cross-peaks are given by the following formula [19].

$$\begin{aligned} &E_{\mathrm{HYSCORE}}(\tau, t_1, t_2) \\ &\sim k/4B\{c^2 \cos(\omega_\alpha t_1 + \omega_\beta t_2 + \delta_+) \\ &\quad - s^2 \cos(\omega_\alpha t_1 - \omega_\beta t_2 + \delta_-) c^2 \cos(\omega_\alpha t_2 + \omega_\beta t_1 + \delta_+) \\ &\quad - s^2 \cos(\omega_\alpha t_2 - \omega_\beta t_1 + \delta_-)\} \end{aligned} \quad (9)$$

where the phase factors are $\delta_\pm = 1/2(\omega_\alpha \pm \omega_\beta)\tau$.

The pulse schemes described in the preceding paragraphs, are currently used as standard ESEEM experiments. Moreover, a number of other improved excitation/detection ESEEM sequences have been developed (for a review see Ref. [39]) some of them resulting in considerable resolution enhancement [40]. Recently, a generalized hyperfine sublevel coherence transfer experiment in one- and two-dimensions [41] was developed by Schweiger and co-workers. Song, Pilbrow and co-workers [42–44] have analysed the advantages of alternative interpulse incrementation schemes and suggested a six-pulse ESEEM sequence in one- and two-dimensions which is essentially a variant of the HYSCORE experiment. Such experiments

improve the standard experiments in several respects. Nevertheless, the experimental ESEEM results that exist in the literature and are presented in this review, have been obtained almost exclusively by two-, three- or four-pulse ESEEM in one dimension and the four-pulse HYSCORE in two-dimensions; thus we focus attention on these experiments.

2.2. Practical aspects and limitations of ESEEM in metal centers

The two-pulse echo decay is determined by its phase-memory time, T_M, instead of its intrinsic linewidths. The stimulated echo decay is limited by the electron spin-lattice relaxation time T_1 and by the nuclear relaxation time T_2. At low-temperatures ($T < 10$ K) T_1 may be longer than T_M. Therefore, at low temperatures the three-pulse echo of slow-relaxing $S = 1/2$ metal centers (Fe^{3+}, Cu^{2+}, VO^{2+}) may be observed up to 3–4 μs. For fast-relaxing spin systems, for example high-spin Fe^{3+} ($S = 5/2$), sub-liquid He temperatures ($T < 4$ K) are often required in order to perform ESEEM experiments.

In three-pulse ESEEM, by setting the τ value equal to whole number of the periodicity of the Larmor frequency of certain nuclei, i.e. for example protons, one can suppress their spectral contribution [25]. This 'suppression effect' although it may be advantageous in simplifying the spectrum, on the other hand it may result in 'blind spots', that is suppression of wanted spectral features. This τ-dependent suppression also occurs in four-pulse and HYSCORE experiments [24,39]. Only the approaches based on probe-pulse detection [45] and some methods that use selective pulses [46] or combinations of selective and non-selective microwave pulses [47] are free of blind spots. In principle, to circumvent the blind-spot influence, a large number of three-pulse, four-pulse ESEEM or HYSCORE spectra for a series of τ values needs to be recorded. A one-dimensional ESEEM experiment then actually becomes a two-dimensional one [48], and the two-dimensional HYSCORE becomes a three-dimensional experiment [49]. As a consequence the ESEEM experiments are time-consuming, in particular the two-dimensional approaches. Nevertheless, in certain cases, e.g. metal centers with fast relaxation times, the data acquisition time may be reduced by the use of fast pulsing rates.

The spectrometer dead time, which prevents detection of the initial portion of the ESEEM signal, results in line-shape distortions or even disappearance of broad lines in the frequency-domain ESEEM spectra [7]. Dead-time problems can be rectified to some extent by digital reconstruction of the experimental spectrum according to the method of Mims [50]. Experimentally, dead-time can be reduced by a pulse-swapping technique [51] or virtually be eliminated by remote echo detection [52]. Recently, Ponti and Schweiger suggested an experiment (DEFENCE) based on a four-pulse sequence that provides spectra free from dead-time distortions [53].

The excitation range of the refocusing π-pulse is a crucial factor in determining the resolution of the four-pulse and HYSCORE spectra. A common problem is that this excitation range is too small (usually < 10 G) to fully transfer the nuclear coherence created by the first two pulses from one M_S manifold to the other. As a

result, in the four-pulse ESEEM peaks at the double basic frequency overlap with combination peaks, while in the HYSCORE peaks appear on the diagonal at the expense of the cross-peaks. For ^{14}N-couplings close to the cancellation condition at X-band and quadrupole coupling constants up to ~ 4 MHz, pulse durations of up to 20 ns, usually employed in HYSCORE experiments, may be considered as ideal pulses [54].

3. Analysis of ESEEM spectra

3.1. Time versus frequency-domain ESEEM

The generic ESEEM spectrum is recorded in the time domain and is characterized by (a) the amplitude of the various echo-modulations and (b) the frequencies of the modulations. The frequency-domain ESEEM spectrum, which can be obtained after Fourier transforming the time-domain trace, contains peaks at the modulation frequencies with their intensities being proportional to modulation amplitude. The advantages of the frequency-domain over the parameter estimation procedure in the time-domain have been first analysed by Merks and DeBeer [55]. The maximum entropy method (MEM) is another method, for obtaining the frequency-domain; MEM is more advantageous than Fourier transforms for short-segments of time-domain data [56] although it has the drawback that it may result in artificial shifts and splitting of the frequencies (for a review see Ref. [57]).

The method of choice for analysis of the ESEEM data, i.e. analysis in the time- or the frequency-domain, is dictated by the relative size of the hyperfine coupling versus the nuclear Zeeman frequency [7]; weak dipolar couplings ($A_{\rm iso} \sim 0, |T| < \nu_I$) can be determined either from analysis of the time-domain ESEEM [12] or from the combination-lines in the frequency domain of two- or four-pulse ESEEM [33–36]. Stronger couplings result in distinct basic frequencies, which can be more easily analysed in frequency-domain ESEEM and HYSCORE spectra.

For very weak nuclear couplings $A_{\rm iso} \sim 0, |T| < \nu_I$, and negligible quadrupole interaction, the powder average of the modulation amplitude, calculated directly from the time-domain ESEEM spectrum, may be used to estimate the distance between the electron and weakly coupled nuclei [58]. This method is valid only for (a) small values of k, i.e. very weak nuclear couplings and (b) even for small values of k it is valid only for small nuclear spins $I = 1/2$, 1 [59]. At increasing values of I higher order terms in k become important and the modulation amplitude becomes strongly non-linear in k [58,59].

A method for extracting a particular normalized modulation from a complicated pattern [25] is based on the quotient of time-domain ESEEM traces recorded for similar samples under similar conditions but with certain proton(s) being replaced by deuterium(s). For weak hyperfine couplings the deuteron versus proton modulation depth is $k(^2\mathrm{H})/k(^1\mathrm{H}) = 8/3$, therefore deuteration improves the modulation depth by a factor of 8/3 [57]. An exemplary application of this technique may be found in Ref. [60]. A variant of this technique, involving band-pass filtration/nor-

malization/Fourier-transform of two-pulse ^{1}H- and ^{2}H-ESEEM was recently introduced [61].

More accurate analysis of the time-domain ESEEM may be performed by numerical simulations of the time-domain spectrum and, based on a spherical model [62] the number of interacting nuclei may be determined. Recently a new algorithm for analysis of ESEEM from weakly coupled distant nuclei has been developed by Astashkin and Tsvetkov [63].

3.2. Sum-combination harmonics (2p, 4p) ESEEM: a tool for measuring weak anisotropic hyperfine couplings for $A_{iso} \sim 0$

Nuclei with zero isotropic couplings, might have non-zero dipolar hyperfine couplings if their distance from the electron spin is low enough. In this case the fundamental nuclear transitions are centered at the free Larmor frequency and have broad line-widths determined by the dipolar interaction. The large line-width associated with the fundamental frequency peaks is effectively cancelled in the sum-combination harmonics, which are governed by the relative size of the anisotropic and isotropic couplings [64]. Combination harmonics are generated in the two- [64] and four-pulse ESEEM [33–36], thus enabling their observation by ESEEM spectroscopy. Furthermore, the frequency shift of the sum-combination peak is predominantly governed by the anisotropic hyperfine coupling rather than the isotropic hyperfine coupling [33–36,64]. Accordingly, measurement of the shift of the sum-combination peak, in two- and four-pulse ESEEM, allows accurate estimations of the distances between the electron spin and neighboring weakly coupled nuclei.

For nuclei $I = 1/2$, at small values for hyperfine coupling, $|T + 2A_{\rm iso}| < 4\nu_I$, the shift of the maxima of the sum combination harmonic $\Delta_{\|} = |(\nu_\alpha + \nu_\beta) - \nu_I|$ at the $g_{\|}$ component of the EPR spectrum, is [32]

$$\Delta_{\|} = (9T_{\perp}^2 \sin^2\theta_{\rm II} \cos^2\theta_{\rm II})/4\nu_I \tag{10a}$$

At the $g_{\perp}$ component of the EPR spectrum the shift is [32]

$$\Delta_{\perp} = \begin{cases} (9T_{\perp}^2 \sin^2\vartheta_{\rm II} \cos^2\vartheta_{\rm II})/4\nu_I & \text{for } \vartheta_{\rm II} \le 45^\circ \text{ or } \vartheta_{\rm II} \ge 135^\circ \\ 9T_{\perp}^2/16\nu_I & 45^\circ \le \vartheta_{\rm II} \le 135^\circ \end{cases} \tag{10b}$$

where $\theta_{\rm II}$ is the angle between the principal axis of the axial hyperfine tensor and the electron g tensor.

In non-orientation selective case, the maximum shift becomes [64]

$$\Delta = 9T_{\perp}^2/16\nu_I \tag{10c}$$

The effective electron-nuclear distance r is calculated from the dipolar hyperfine coupling $T_{\perp} = g\beta g_n\beta_n/hr^3$, which is calculated from the shift of the combination lines according to 10. Some consequences of 10 are worth noting; in as much the ratio in 10 is proportional to the nuclear g_n factor, shifts of sum-combination peaks should be most evident for nuclei with large g_n factors. Therefore, the practical

utilization of sum-combination frequency shifts to measure $T_{\perp}$ is best suited for protons. Second, the inverse relation of the shift to the external magnetic field strength suggests that ESEEM experiments at decreasing microwave frequencies would enhance the shifts of the combination harmonics. This has been verified experimentally in measurements of the shift of sum-combination harmonics for protons in VO-apoferritin [65]; a combination line shifted by $\Delta \sim 0.5$ MHz, corresponding to $T \sim 4.3$ MHz, which was clearly resolved at 9.6 GHz, was nullified at 11.6 GHz. The shift of the sum-combination harmonic has been applied in the resolution of weak dipolar couplings of protons in the primary semiquinone of Photosystem II [66], in a dinuclear Mn complex [67], in aqua-vanadyl complexes [33,34] and to resolve axial water ligation to a Ni^{3+} complex [36]. In VO^{2+}-D-xylose isomerase, resolution and analysis of the sum-combination harmonics allowed the detection of two proton couplings from a histidine ligand to VO^{2+} [68]. The analysis of the combination harmonics in the four-pulse ESEEM of ^{15}N-labelled superoxide dismutase allowed the resolution of weak couplings from the remote ^{15}N [69]. In multifrequency ESEEM of silica supported vanadyl [70] and molybdenum [71] oxide catalysts, proton dipolar couplings of 3.6–3.7 MHz — corresponding to proton–metal distance of ~ 2.8 Å — were determined through analysis of two-pulse combination lines. In the case of ^{27}Al ($I = 5/2$), simulations showed that under certain conditions, the sum combination lines of ^{27}Al ($I = 5/2$) may exhibit fine structure from which the quadrupole interaction may be determined [35].

3.3. Aspects of the general theoretical formalism of ESEEM

Recently, Ponti [59] based on the original work of Dikanov et al. [72] showed that the primary and stimulated ESEEM due to a nucleus of arbitrary spin $I \geq 1/2$ can be expressed as a function of Chebychev polynomials of the second kind, in which the independent variable is the expression for ESEEM of a hypothetical $I = 1/2$ nucleus with the same coupling parameters as the real one [59]. These expressions have been derived under the high-field approximation for negligible quadrupole interaction. The introduction of non-negligible quadrupole interaction usually complicates the analysis [73]; for such a case an analytical solution does not exist and numerical simulations are required for the simulation of the ESEEM spectra.

The general problem of theoretical description of the ESEEM spectra for $S = 1/2$ coupled to an arbitrary nuclear spin with no-negligible quadrupole interaction can be addressed only by numerical simulations. Since in experimental work the three-pulse ESEEM experiment is the standard tool for measuring basic nuclear frequencies, we outline the general formula and procedure for simulating three-pulse ESEEM spectra of an arbitrary spin with non-negligible quadrupole interaction. The salient features of representative spectra are exemplified through theoretical three-pulse ESEEM spectra, calculated numerically according to the general formulation [11].

The spin Hamiltonian for a $\boldsymbol{S} = 1/2$ system is

$$\boldsymbol{H} = \boldsymbol{g}\cdot\beta\boldsymbol{B}\cdot\boldsymbol{S} + g_n\,\beta_n\,\boldsymbol{I}\cdot\boldsymbol{B} + \boldsymbol{I}\cdot\boldsymbol{A}\cdot\boldsymbol{S} + \boldsymbol{I}\cdot\boldsymbol{Q}\cdot\boldsymbol{I} \tag{11}$$

In the most general case a metal center has rhombic the g-tensor; at a given orientation $(l_1, l_2, l_3) = (\sin\theta\cos\phi, \sin\theta\sin\phi, \cos\theta)$ of the external magnetic field $\boldsymbol{B}$ relative to the g-tenor axes system, Fig. 3. The matrix of the hyperfine tensor $\boldsymbol{A}$ is described in relation (6a). The quadrupole interaction term is non zero only for $I > 1/2$; the nuclear quadrupole tensor $\boldsymbol{Q}$ in its principal axes system has the form [1]

$$\boldsymbol{Q} = \begin{pmatrix} Q_{XX} & 0 & 0 \\ & Q_{YY} & 0 \\ 0 & 0 & Q_{ZZ} \end{pmatrix} \tag{12}$$

$$\boldsymbol{Q} = \frac{qe^2Q}{4I(2I-1)h} \begin{pmatrix} -(1-\eta) & 0 & 0 \\ 0 & -(1+\eta) & 0 \\ 0 & 0 & 2 \end{pmatrix} \tag{13}$$

where $\eta = (Q_{XX} - Q_{YY})/Q_{ZZ}$ is the asymmetry parameter, and Q is the quadrupole moment interacting with the electric field gradient q at the nucleus. The principal axes systems of the tensors $\boldsymbol{g}$, $\boldsymbol{A}$ and $\boldsymbol{Q}$ are related by the appropriate Euler angles [73].

In cases when the electron spin manifolds are well separated in energy, which is valid for $S = 1/2$ metal complexes with the electron Zeeman interaction being much stronger than the metal hyperfine and all the nuclear interaction, spin Hamiltonian $\boldsymbol{H}$ in matrix form consists of two blocks H^{α} and H^{β} corresponding to the α and β electron spin states, then the general expression for the three-pulse stimulated echo modulation may be calculated according to the expression (14a) [11].

$$\begin{aligned} &E(\tau, T) \\ &= \frac{1}{(1+2I)} \left\{ \sum_{i,k} |M_{ik}|^4 + \frac{1}{2} \sum_{i \neq j} X_{ij}^{\alpha} [\cos\omega_{ij}^{\alpha}\tau + \cos\omega_{ij}^{\alpha}(\tau + T)] \right. \\ &\quad + \frac{1}{2} \sum_{k \neq n} X_{kn}^{\beta} [\cos\omega_{kn}^{\beta}\tau + \cos\omega_{kn}^{\beta}(\tau + T)] \\ &\quad \left. + \sum_{i \neq j} \sum_{k \neq n} X_{ij,kn}^{(\alpha,\beta)} [\cos\omega_{ij}^{\alpha}(\tau + T)\cos\omega_{kn}^{\beta}\tau + \cos\omega_{ij}^{\alpha}\tau\cos\omega_{kn}^{\beta}(\tau + T)] \right\} \end{aligned} \tag{14a}$$

$$X_{ij}^{\alpha} = 2 \sum_{k} |M_{ik}|^2 |M_{jk}|^2$$

$$X_{kn}^{\beta} = 2 \sum_{i} |M_{ik}|^2 |M_{in}|^2 \tag{14b}$$

$$X_{ij,kn}^{(\alpha,\beta)} = 2\mathrm{Re}[M_{ik}^* M_{in}^* M_{jn}^* M_{jk}] \tag{14c}$$

In this expression ω_{ij}^{α} are the nuclear transition frequencies $\omega_i^{\alpha} - \omega_j^{\alpha}$ belonging to the α electron-spin manifold and similarly ω_{kn}^{β} belonging to the β manifold with the

various $\omega_{i,}^{\alpha}$ ω_{i}^{β} being the eigenvalues of the H^{α} and H^{β} hamiltonians, respectively. The eigenvector of the ith eigenstate of the α spin manifold ($m_s = +1/2$) is expressed as

$$\psi_{\mathrm{i}}^{\alpha} = c_{i,m_I}^{\alpha}|+1/2,\ +m_I> + c_{i,m_I-1}^{\alpha}|+1/2,\ m_I-1> + \cdots + c_{I,-m_I+1}^{\alpha}|+1/2,\ -m_I+1> + c_{I,-m_I}^{\alpha}|+1/2,\ -m_I> \quad (15)$$

Using the vector C_i^{α} which has components of complex numbers $c_{i,k}^{\alpha}$ we construct the matrix elements M_{kn} [3,11]

$$M_{kn} = \mathrm{C}_k^{\alpha +} \cdot \mathrm{C}_m^{\beta} \quad (16)$$

The matrix element M_{kn} gives the EPR transition amplitude from the kth sublevel within the α spin manifold to the nth sublevel within the β spin manifold. By using these matrix elements the modulation coefficients X_{ij} are calculated for each spin manifold according to 14(b,c). From 14 it is seen that the non-zero modulation requires simply non-zero X_{ij} values, i.e. non-zero M_{ij} values. Since the matrix-elements of the matrix **M** are the transition moments between allowed and semi-forbidden EPR transitions, see Eq. (16), non-zero ESEEM is produced only if these allowed and semi-forbidden transitions have some common character i.e. only if there are admixed to some extent [3,11]. For $I = 1/2$, the necessary admixing of the states can be produced only by anisotropic hyperfine interactions, i.e. for $I = 1/2$, purely isotropic interaction does dot give rise to ESEEM [3,7,11]. For $I = 1$, in the presence of quadrupole interaction admixing of the state occurs even in the case of purely isotropic hyperfine interaction [74]. Formulae 14(a,b,c) describe the three-pulse ESEEM appropriate for a $S = 1/2$ electron spin coupled to any nuclear spin I. In general, their utilization requires diagonalization of the pertinent spin hamiltonians, calculation of the **M**-matrix, and calculation of the modulation function, Eq. 14a.

In the case of several nuclei coupled to the same electron spin, the resulting three-pulse modulation functions for each spin manifold were multiplied in the time domain [11] according to

$$E(\tau, T) = 1/2\left(\prod_i E_{\alpha}(t, T) + \prod_i E_{\beta}(\tau, T)\right) \quad (17)$$

where i runs over all the interacting nuclei.

3.3.1. Orientation selection

Metal centers are often characterized by anisotropic **g** and/or **A** tensors resulting in broad EPR spectra [2]. On the other hand, the power of the microwave pulses is limited, e.g. typically $H_1 < 10$ G for most spectrometers; consequently at each resonant magnetic field only spins at certain orientations θ and ϕ contribute to the detected echo, that is the ESEEM experiment is 'orientation selective'. The total echo intensity is calculated by the formula

$$E_{\mathrm{tot}} = 1/N \int_{\phi_{\min}}^{\phi_{\max}} \int_{\theta_{\min}}^{\theta_{\max}} E(\theta, \phi) \sin\theta \, \mathrm{d}\theta \, \mathrm{d}\phi \quad (18)$$

where N is the normalization factor $N=[\phi_{max}-\phi_{min}][\cos(\theta_{min})-\cos(\theta_{max})]$, which in the non-orientation selective case equals 4π. The ranges of θ and ϕ that contribute the echo at each magnetic field within the EPR line shape can be determined by two methods: (a) by performing the integration over the orientations of H that fall on contour of constant g_{eff}. This line integral may be calculated by the method of Hoffman et al. [75] where the integral is transformed to a definite integral over ϕ by numerical evaluation of the integration factor

$$[(\partial\theta/\partial\phi)^2+\sin^2\theta]^{1/2}=\left[\frac{(g_1^2-g_2^2)^2\sin^6\theta(\phi,g)}{(g_1^2-g_2^2)^2\cos^6\theta(\phi,g)}\cos^2\phi\,\sin^2\phi+\sin^2\theta\right]^{1/2}$$

for a particular g_{eff} value. (b) Graphically, from the angular dependence of the EPR resonances as described by Goldfarb et al. [76]. Properly interpreted, the orientation selective ESEEM spectra may provide useful geometrical information about the coordination environment of the complex [75–77]. Another eventual advantage of the orientation selectivity is the narrowing of ESEEM lines whenever they are spread by anisotropic hyperfine interactions [78].

3.4. Representative ESEEM spectra

In a powder sample, the ESEEM spectrum is the superposition of spectra at different orientations. The shapes and maxima positions of the lines in the spectrum are defined by the angular dependence of the modulation frequencies, their amplitudes and the statistical weight of each orientation. In general, the line shape in ESEEM spectra does not permit the determination of the isotropic and anisotropic hyperfine interactions directly from the maxima of the spectrum, without numerical simulations [7]. A glorious exception is the case when the hyperfine coupling 'matches' the nuclear Zeeman interaction $A_{iso}=2\nu_I$ [78]. In the following, we discuss briefly the shapes of ESEEM spectra for characteristic coupling regimes.

The line shapes in ESEEM spectra of a disordered system have been analysed for $S=1/2$ interacting with one nucleus with $I=1/2$ [9,64,79], $I=1$ with negligible [80] and considerable quadrupole interaction [9,74], $I=3/2$ [9,81] and $I=5/2$ [82].

For ($I=1/2$), Lai et al. [79] demonstrated that the relative size of the hyperfine and nuclear Zeeman hamiltonians determines the shape ESEEM spectra. Reijerse and Keijzers [9] presented a numerical simulation of frequency-domain ESEEM in comparison with the corresponding ENDOR spectra. Reijerse and Dikanov [64] developed a general procedure for analyzing the basic and also the combination lines in ESEEM of $I=1/2$. Fig. 4 presents time- and the frequency-domain three-pulse ESEEM for three limiting coupling regimes.

In the case of an axial hyperfine tensor for

$$4\nu_I=2A_{iso}+T \tag{19a}$$

known as 'matching condition' [79] the ESEEM spectrum attains a characteristic shape i.e. it is characterized by two frequencies a dominant narrow feature at

$$\nu_\alpha\sim 3T/4 \tag{19b}$$

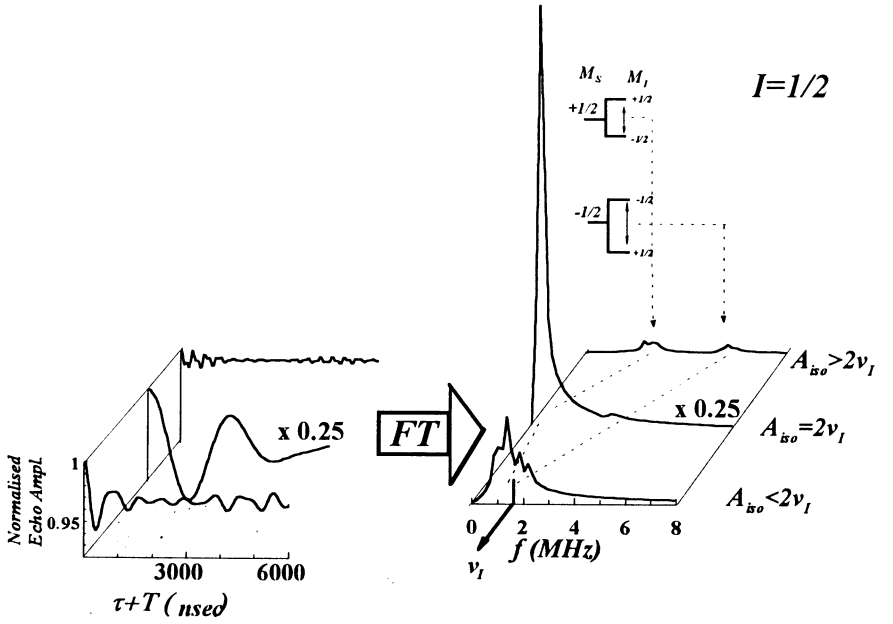

Fig. 4. Theoretical ESEEM spectra for a $S=1/2$ spin coupled to a single $I=1/2$ nucleus. The frequency-domain spectra are obtained by Fourier transforming (FT) the time-domain signals. The two nuclear transitions between the energy levels in the two M_S manifolds are also depicted. Simulation parameters: $A_{iso}=1.5$ MHz ($A_{iso}<2\nu_I$), $A_{iso}=3.1$ MHz ($A_{iso}=2\nu_I$) and $A_{iso}=6.3$ MHz ($A_{iso}>2\nu_I$). Common simulation parameters: anisotropic hyperfine coupling $T=0.45$ MHz, $\nu_I=1.56$ MHz; for each time-domain spectrum 512 time points in intervals of 20 ns were calculated. In the matching regime e.g. when $2A_{iso}+T=4\nu_I$, a dispersionless narrow feature dominates the spectrum with maximum at a frequency $\nu_\alpha=3T/4$, while its partner at $\nu_\beta \sim 2\nu_I$ is faint. For deviations either $A_{iso}<2\nu_I$ or $A_{iso}>2\nu_I$ the spectral intensities are weaker.

and a broad, weak one at

$$\nu_\beta \sim 2\nu_I \tag{19c}$$

see Fig. 4. For hyperfine couplings which deviate from the matching conditions the intensity and resolution of the spectral features decreases significantly. For weak couplings $A_{iso}<2\nu_I$ the main peaks are centered approximately at ν_I while for strong couplings $A_{iso}>2\nu_I$ the spectral features are centered at $A_{iso}/2$ [64], Fig. 4. A comprehensive geometrical representation of the nuclear modulation effects that enables facile understanding of ESEEM spectra for $I=1/2$ coupled to an electron spin in disordered systems, has been developed by Singel and his co-workers [83].

The published experimental ESEEM spectra for $I=1$ refer to either ^{14}N or ^{2}H modulations. Quadrupole interaction is usually negligible for ^{2}H, but is important for ^{14}N, at least for the X-band [7]. In Mims's pioneering description of ESEEM amplitudes [11], analytic expressions for $I=1$ nuclei were derived for the limiting case of small quadrupole couplings-appropriate for ^{2}H, for example, but not for ^{14}N. The characteristics of the ^{2}H-ESEEM line shapes have been fully explored by

Tyryshkin et al. [80]. ^{14}N-ESEEM was first analysed by Mims and Peisach [84]. A more universal approach to the interpretation of ^{14}N-ESEEM has been put forth by Astashkin et al. [85]. Based on this approach, Flanagan and Singel [74] performed a detailed theoretical investigation on the relative importance of the spin-Hamiltonian terms on the ^{14}N-ESEEM spectral lines. As in the case for $I = 1/2$, matching of the hyperfine and nuclear Zeeman terms, $A_{\mathrm{iso}} = 2\nu_I$, leads in line narrowing although the spectral shapes obtained for ^{14}N ($I = 1$), Fig. 5, are radically different than those for $I = 1/2$, Fig. 4.

In the so called 'cancellation condition' $A_{\mathrm{iso}} = 2\nu_I$, three narrow low-frequency components arise from the ^{14}N superhyperfine spin manifold, where the nuclear-Zeeman and electron–nuclear hyperfine interaction approximately cancel one another (see energy levels in Fig. 5), so that the level splitting are primarily determined by the ^{14}N nuclear quadrupole interaction (NQI). The three sharp low-frequency lines, with maxima at frequencies given by the relations

$$\nu_+ = 3K(1+\eta),\ \nu_- = 3K(1-\eta),\ \nu_0 = 2K\eta \tag{20}$$

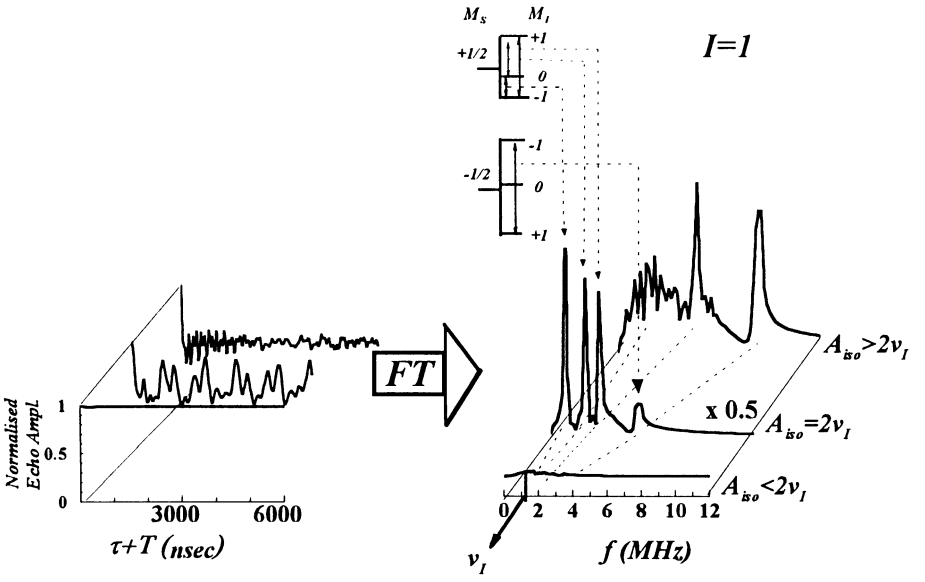

Fig. 5. Theoretical ESEEM spectra for a $S = 1/2$ spin coupled to a single ^{14}N($I = 1$) nucleus. The frequency-domain spectra are obtained by Fourier transforming (FT) the time-domain signals. The resolved nuclear transitions between the energy levels in the two M_S manifolds are also depicted. Simulation parameters: $A_{\mathrm{iso}} = 1.04$ MHz ($A_{\mathrm{iso}} < 2\nu_I$), $A_{\mathrm{iso}} = 2.08$ MHz ($A_{\mathrm{iso}} = 2\nu_I$) and $A_{\mathrm{iso}} = 4.16$ MHz ($A_{\mathrm{iso}} > 2\nu_I$). Common simulation parameters: anisotropic hyperfine coupling $T = 0.2$ MHz, $\nu_I = 1.04$ MHz; $e^2qQ/h = 3.2$ MHz, $\eta = 0.5$; for each time-domain spectrum 512 time points in intervals of 20 ns were calculated. In the cancellation condition e.g. when $A_{\mathrm{iso}} = 2\nu_I$, three narrow quadruple features (ν^0, ν^- and ν^+ all originating from the $M_S = +1/2$ spin manifold) plus a broader double quantum, $|\Delta m_I| = 2$, frequency (originating from the $M_S = -1/2$ spin manifold) dominate the spectrum. For $A_{\mathrm{iso}} > 2\nu_I$ two sharp features ν_{dqa} and ν_{dqb} are resolved form the two $|\Delta m_I| = 2$ transitions.

where $K = e^2qQ/4h$. The positions of the lines are determined by the values of K and η, while their relative intensities are sensitive to the relative orientation of the NQI principal axes system with respect to the hyperfine coupling tensor and the τ value used for the measurement [74]. The superhyperfine manifold, where the nuclear-Zeeman and the hyperfine interactions are additive, gives rise to much broader resonances [74] and the only resolvable component is a double quantum transition line, $\Delta m_I = 2$, occurring at higher frequencies. The double-quantum line has maximum intensity at a frequency that is approximated by

$$\nu_{\mathrm{dq}} \sim 2[(\nu_I + A/2)^2 + K^2(3 + \eta^2)]^{1/2} \tag{21}$$

where A is a secular component of the hyperfine coupling tensor determined mainly from its isotropic part; a modest anisotropy of the hyperfine interaction affects mainly the line shape but not the frequency of the double quantum line [9,74,86]. In the case of deviation from the exact cancellation condition under negligible anisotropy, the modulation depth is attenuated when $|\nu_I - A_{\mathrm{iso}}/2| < 2K/3$ while it is still possible to observe ^{14}N-ESEEM frequencies similar to that observed for exact cancellation [74]. In the limit of either weak hyperfine couplings, $A_{\mathrm{iso}} \ll \nu_I$, or in the presence of excessive anisotropy [9,86] the ESEEM features degrade. For strong hyperfine couplings, sharp features are always observed for isotropic couplings at the double quantum transitions in the two spin manifolds [74]. For the rhombic hyperfine tensor the double quantum frequencies are [87]

$$\nu_{\alpha(\mathrm{dq})} = 2[l_1^2(\nu_I - A_1/2)^2 + l_2^2(\nu_I - A_2/2)^2 + l_3^2(\nu_I - A_3/2)^2 + K^2(3 + \eta^2)]^{1/2} \tag{22a}$$

$$\nu_{\beta(\mathrm{dq})} = 2[l_1^2(\nu_I + A_1/2)^2 + l_2^2(\nu_{\mathrm{I}} + A_2/2)^2 + l_3^2(\nu_I + A_3/2)^2 + K^2(3 + \eta^2)]^{1/2} \tag{22b}$$

where l_i, $i = 1, 2, 3$ are the direction cosines of the magnetic field, see Fig. 3.

The two characteristic cases of ^{14}N couplings, e.g. $A = 2\nu_I$ and $A \gg 2\nu_I$, are often encountered in square planar Cu^{2+} and VO^{2+} complexes, respectively. In VO^{2+} complexes the single unpaired electron occupies a non-bonding d_{xy} orbital which has minimal overlap with the ligand orbitals [2]; in contrast, in square planar Cu^{2+} the unpaired electron occupies a $d_{x^2-y^2}$ orbital [2] and this allows a significant overlap with the ligand orbitals. This basic picture highlights the origin of the observed differences in ^{14}N couplings for isostructural Cu^{2+} versus VO^{2+} complexes: in most VO^{2+} systems studied so far, the ^{14}N hyperfine couplings are not within the cancellation condition of the X-band. For instance, A_{iso} of the remote ^{14}N of imidazole in VO^{2+}-[imidazole]$_4$ is very small e.g. 0.3 MHz, almost 20 times smaller than the $A_{\mathrm{iso}} \sim 6$ MHz, for the directly coordinated imidazole nitrogens [88]. Thus the X-band ESEEM spectra of VO^{2+}–^{14}N systems are characterized by two double quantum frequencies, 22, see Fig. 5, due to the directly coordinated nuclei, see Fig. 6.

The ratio of $\sim 1/20$ holds for the A_{iso} couplings of the remote ($A_{\mathrm{iso}} \sim 2$ MHz) [84] and coordinated ($A_{\mathrm{iso}} \sim 40$ MHz) [89,90] ^{14}N nuclei in Cu^{2+}-[imidazole]$_n$. Note however that the absolute values of A_{iso} in Cu^{2+} complexes are almost one order of magnitude larger than in VO^{2+} complexes. Thus, the X-band ESEEM spectra of Cu-imidazole are dominated by the 'three sharp plus a broad line' due to the

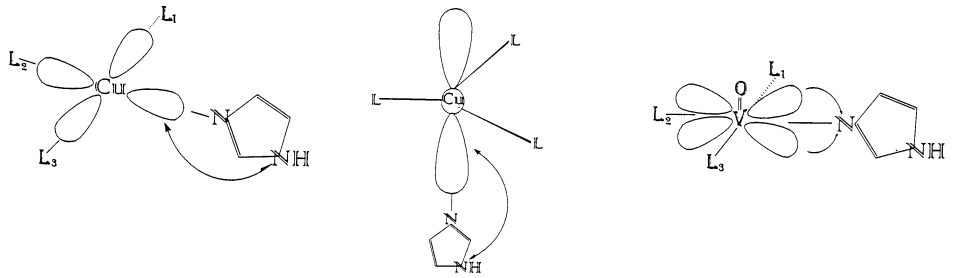

Fig. 6. In square planar Cu^{2+} complexes the unpaired electron occupies a $d_{x^2-y^2}$ orbital and this allows a significant overlap with the equatorially coordinated ligand orbitals. In trigonal bipyramidal Cu^{2+} complexes the unpaired electron occupies a d_{z^2} orbital and has significant overlap with the axially coordinated ligand orbitals. In square pyramidal VO^{2+} complexes the single unpaired electron occupies a non-bonding d_{xy} orbital which has minimal overlap with the ligand orbitals. In all cases, A_{iso} of the remote ^{14}N of imidazole is almost 20-times smaller than the A_{iso} for the directly coordinated imidazole nitrogens. The arrows in the figure indicate the ^{14}N nucleus, which is resolved by ESEEM at the X-band. In VO^{2+}-imidazole, the directly coordinated ^{14}N has $A_{iso} \sim 6$ MHz, and is detected by X-band ESEEM. In, Cu^{2+}-imidazole, the directly coordinated ^{14}N has $A_{iso} \sim 30$–40 MHz, and is not detected by the X-band ESEEM. In contrast the non-coordinated remote nitrogen has $A_{iso} \sim 1.5$–2 MHz and is detected by the X-band ESEEM.

remote non-coordinated nitrogen, Fig. 6, whose couplings fulfil the cancellation condition. The magnetic couplings for ^{14}N directly coordinated to Cu^{2+} are usually resolved by ENDOR spectroscopy, but not by ESEEM at the X-band.

In the case of one nucleus with $I = 3/2$, the salient features of the ESEEM spectra of disordered systems are dominated by the contribution from the nuclear transitions between the $m_I = +1/2$ and $m_I = -1/2$ levels [81]. Therefore, for modest quadrupole couplings the salient features of the ESEEM spectrum for $I = 3/2$ nuclei, resemble those of an effective $I = 1/2$ system, see Figs. 4 and 7 [81].

In $I = 3/2$ systems, matching of the hyperfine and nuclear Zeeman interactions leads to line-narrowing and a sharp feature close to zero-frequency is expected [81]. However, even for small deviations from the matching condition, the intensity of the spectral features degrade rapidly [9,81] and thus the line-narrowed sharp feature expected from theory, is rather difficult to observe in real experiments. Analogous considerations, as those for $I = 3/2$, hold for the ESEEM spectra of $I = 5/2$ nuclei [82].

3.5. 2D-HYSCORE: A tool for disentangling complicated ESEEM spectra

The concept of the two-dimensional Fourier transform technique in ESEEM was first introduced by Merks and DeBeer [48], based on the three-pulse procedure where the τ value is varied as the second time-axis. However, it was the HYSCORE experiment [49] as an analogue of the homonuclear correlation spectroscopy (COSY) in NMR [91], that showed forth the advantages of the two-dimensional spectroscopy in ESEEM. In the 2D-HYSCORE experiment the nuclear spin transitions in the two different M_S manifolds are correlated to each other non-diag-

onal by cross-peaks, appearing at (ν_α, ν_β), (ν_β, ν_α) and $(\nu_\alpha, -\nu_\beta)$, $(\nu_\beta, -\nu_\alpha)$ in the $(+, +)$ and $(+, -)$ quadrants, respectively, of the 2D-frequency domain spectrum [48,92]. In the case of anisotropic hyperfine interaction the correlation peaks of a powder 2D spectrum become ridges [87,92,93]. The characteristics of the HYSOCRE spectra have been described for $I = 1/2$ having either isotropic [93] or axial g-tensor [94], for $I = 1$ [54,87,92], and more recently for $I = 3/2$ [81,95].

For $I = 1/2$, Dikanov and Bowman [93] have derived analytical formula for the contour line forms of the correlation ridges in the frequency-domain HYSCORE:

$$\nu_{\alpha(\beta)} = [Q_{\alpha(\beta)}\nu^2_{a(\beta)} + G^2_{\alpha(\beta)}]^{1/2} \tag{23}$$

where

$$Q_{\alpha(\beta)} = (2A_{\mathrm{iso}} + 4\nu_I + T)/(2A_{\mathrm{iso}} \pm 4\nu_I + T)$$

and

$$G_{\alpha(\beta)} = \pm 2\nu_I(4\nu_I^2 - A^2_{\mathrm{iso}} + 2T^2 - TA_{\mathrm{iso}})/(2A_{\mathrm{iso}} + T \pm 4\nu_I)$$

These relations do not depend on the time τ between the first and the second pulse and thus correspond to ideal 'suppression free' 2D spectra [93]. The amplitude

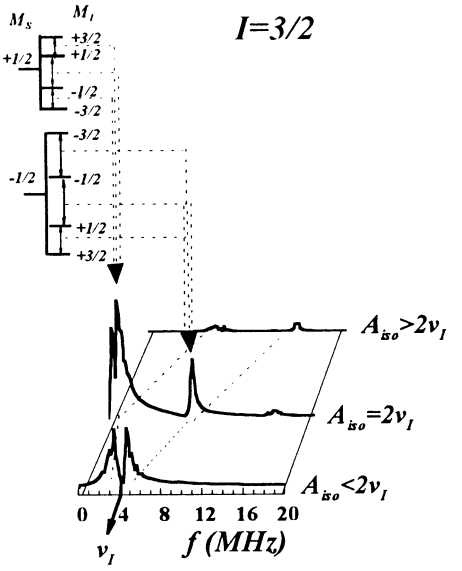

Fig. 7. Theoretical ESEEM spectra for a $S = 1/2$ spin coupled to a single $I = 3/2$ nucleus. The nuclear transitions between the energy levels in the two M_S manifolds are also depicted. Simulation parameters: $A_{\mathrm{iso}} = 3.9$ MHz ($A_{\mathrm{iso}} < 2\nu_I$), $A_{\mathrm{iso}} = 7.8$ MHz ($A_{\mathrm{iso}} = 2\nu_I$) and $A_{\mathrm{iso}} = 11.6$ MHz ($A_{\mathrm{iso}} > 2\nu_I$). Common simulation parameters: anisotropic hyperfine coupling $T = 0.9$ MHz, $\nu_I = 3.9$ MHz; $e^2qQ/h = 1.2$ MHz, $\eta = 0.5$; for each time-domain spectrum 512 time points in intervals of 20 ns were calculated. In the matching regime e.g. when $2A_{\mathrm{iso}} + T = 4\nu_I$, a narrow feature with a maximum close to zero frequency dominates the spectrum. The main contribution to the spectral intensity arises from transitions between the $m_I = \pm 1/2$ nuclear sublevels.

coefficients of the cross-peaks in the 2D-HYSCORE spectrum are given by the transition probabilities c^2 and s^2, relations 3(a,b), and they determine the sign of the phase modulation [92,93]: In the limit of weak hyperfine interaction, the contributions with positive phase modulation (which have an amplitude coefficient c^2) dominate; consequently in the frequency domain the cross-peaks are predominantly in the $(+, +)$ quadrant [92,93]. In the limit of strong hyperfine interaction, the contributions with negative phase modulation (which have an amplitude coefficient s^2) dominate; in this case, the cross peaks are predominantly in the $(+, -)$ quadrant. When the hyperfine and Zeeman coupling have similar magnitude i.e. in the matching regime $A_{iso} \sim 2\nu_I$, then the cross-peaks in the 2D-HYSCORE spectrum have comparable intensity in both quadrants. Representative correlation ridges calculated in this way for characteristic sets of hyperfine couplings by using Eq. (23) are displayed in Fig. 8; at each panel in this figure only the quadrant with the stronger lines is displayed.

According to relations 23, measurement of the anisotropic hyperfine coupling is straightforward from the frequencies of the edges of the correlation ridges. In many cases, however, a common problem is that the resolution at the edges is poor since the modulation intensity is minimal at the canonical orientation of the hyperfine tensor [7]. An alternative procedure for analysis of weak $I = 1/2$ couplings in HYSCORE spectra has been developed by Pöppl and Kevan [94]. In their method the axial hyperfine interaction can be calculated from the maximum shift of the correlation peaks with respect to the (ν_I, ν_I) peak. An additional advantage of this method is that in cases of the anisotropic g-tensor, the relative orientation of the hyperfine tensor versus the g-tensor can be deduced directly from the spectrum [94].

For $I = 1$ with non-negligible quadrupole coupling, i.e. the case of ^{14}N nucleus, analytical formulas describing the frequencies and shapes of the cross peaks for $I = 1$ have been derived [87]. For one ^{14}N nucleus 18 correlation ridges are predicted [87] but not all of them are resolved in experimental HYSCORE. In general, frequencies characterized by strong dispersion, due to anisotropy, are difficult to be resolved in ESEEM spectroscopy. In cases of non-negligible hyperfine anisotropy, ^{14}N-cross peaks involving the double quantum lines are usually less dispersed and dominate the HYSCORE spectrum [87,92]. Characteristic simulated HYSCORE spectra for one ^{14}N nucleus with weak $A_{iso} < 2\nu_I$ and strong $A_{iso} > 2\nu_I$ couplings are displayed in Fig. 9

The superiority of 2D-HYSCORE over the one-dimensional ESEEM for the determination of the basic nuclear frequencies has been demonstrated experimentally in complex systems: four strongly anisotropic ^{15}N couplings were resolved and fully assigned by 2D-HYSCORE for the pheophytin of Photosystem II [86]; analogous remarkable resolution has been achieved in the HYSCORE study of quinones in flavoproteins [96] and the primary donor of bacterial reaction centers [97]. In semimetherythrin, HYSCORE resolved five nitrogen couplings [98] whilst a three-pulse-ESEEM study of the analogous system had resolved only two couplings [99]. Noteworthy is that in these cases [86,96,98] very strong nitrogen couplings e.g. A_{iso} up to 15 MHz, were resolved by HYSCORE and this demonstrates how HYSCORE expends the hyperfine coupling window which can be investigated by

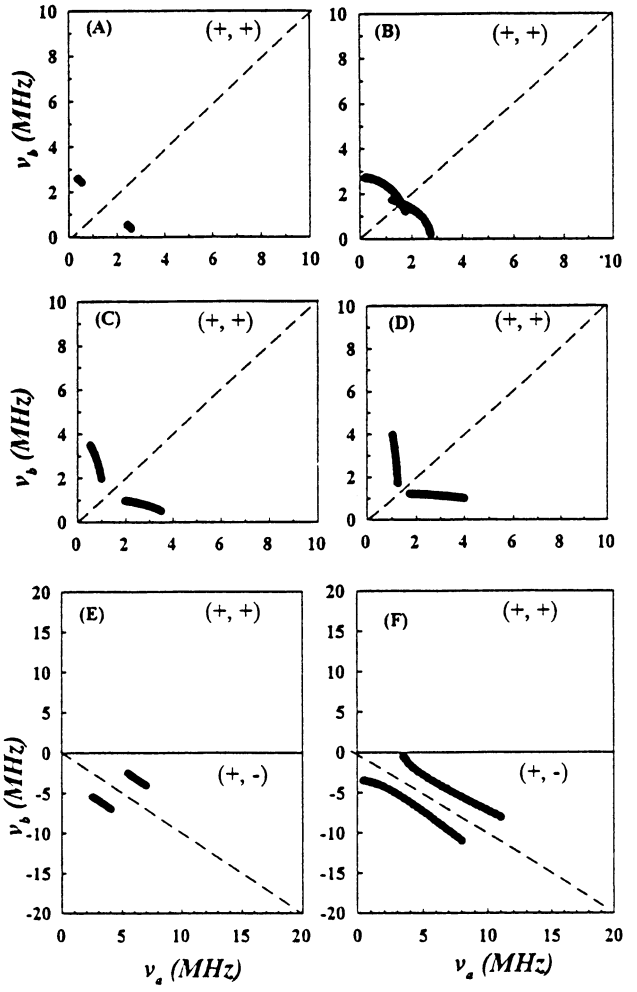

Fig. 8. Theoretical line shapes of the cross-peaks of 2D-HYSCORE spectra for a single $I = 1/2$ nucleus coupled to a $S = 1/2$ spin, calculated by use of Eq. (23) for $\nu_I = 1.49$ MHz. The isotropic, A_{iso}, and the axially anisotropic T hyperfine coupling parameters used are: $(A_{iso}, T) = (0.4, 0.2$ MHz) in panel A, (1.0, 0.8 MHz) in panel B, (1.7, 0.8 MHz) in panel C, (2.4, 1.1 MHz) in panel D, (4.0, 0.2 MHz) in panel E and (6.0, 4.0 MHz) in panel F. Reprinted form Ref. [86] after permission. Copyright 1997 American Chemical Society.

ESEEM techniques. Complicated proton couplings have been resolved in HYSCORE spectra of the Fe–S centers [100]. In borate glasses HYSCORE allowed the resolution and assignment of multiple couplings from ^{11}B ($I = 3/2$) and ^{10}B ($I = 3$) nuclei [81]. Detailed structural information can also be extracted from the analysis of the inhomogeneous and homogenous broadening of proton ESEEM lines, and this task is achievable through the use of HYSCORE [101]. A promising variant of HYSCORE, termed double-nuclear-coherence-transfer-HYSCORE

(DONUT-HYSOCRE), has been introduced recently [102]. The pulse sequence is $\pi/2$-τ_1-$\pi/2$-τ_1-π-τ_2-π-τ_2-$\pi/2$-τ_1-echo, and is complementary to the standard HYCORE [102].

3.6. High-spin $S > 1/2$ paramagnetic centers

The ground state of multielectron spin systems in the solid state is often nondegenerate even in zero magnetic field [1]. This zero-field splitting, together with the high-spin multiplicity complicates the analysis of the EPR spectra [1,2]. In cases when the magnetic properties of the ground state can be described by a spin-Hamiltonian, this usually has the form of the Hamiltonian (11) augmented by a zero-field splitting term [1]

$$H_{\mathrm{ZFS}} = \boldsymbol{S}\cdot\boldsymbol{D}\cdot\boldsymbol{S} \tag{24}$$

and the total spin Hamiltonian becomes

$$H = \boldsymbol{g}\cdot\beta\boldsymbol{B}\cdot\boldsymbol{S} + \boldsymbol{S}\cdot\boldsymbol{D}\cdot\boldsymbol{S} + g_n\beta_n\boldsymbol{I}\cdot\boldsymbol{B} + \boldsymbol{I}\cdot\boldsymbol{A}\cdot\boldsymbol{S} + \boldsymbol{I}\cdot\boldsymbol{Q}\cdot\boldsymbol{I} \tag{25}$$

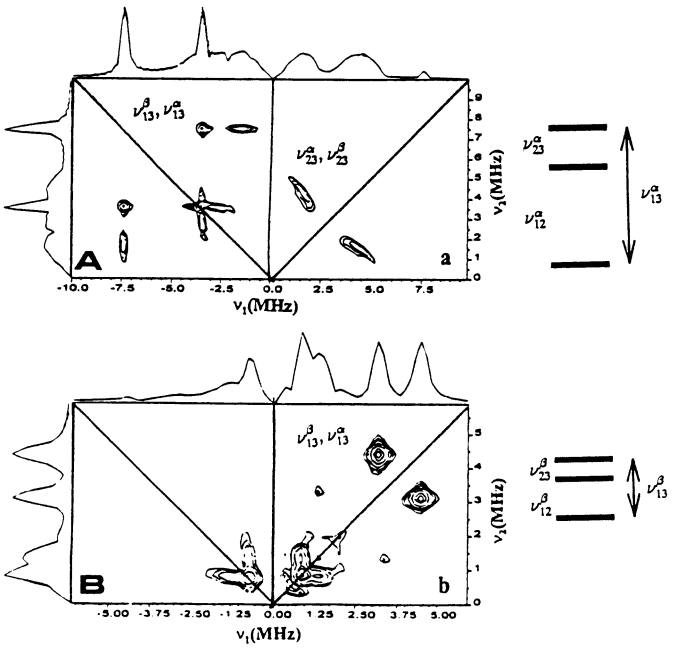

Fig. 9. Simulated HYSCORE spectra for a single ^{14}N($I = 1$) nucleus coupled to a $S = 1/2$ spin. The spectra correspond to strong (A) and weak (B) hyperfine couplings. The assignment of the observed cross-peaks to the nuclear transition is assisted by reference to the energy level scheme depicted on the right. Simulation parameters: (A) $A_{\mathrm{iso}} = 5$ MHz, $\nu_I = 1.08$ MHz, $K = 0.6$ MHz, $\eta = 0.5$, $\tau = 136$ ns. (B) $A_{\mathrm{iso}} = 1.1$ MHz, $\nu_I = 1.08$ MHz, $K = 0.81$ MHz, $\eta = 0.5$, $\tau = 400$ ns. Reprinted form Ref. [87] after permission. Copyright 1996 American Chemical Society.

where the first two terms refer to the electron spin while the last three describe the nuclear couplings. The nuclear g_n is taken as scalar. Tensor $\boldsymbol{D}$ is the, traceless, zero-field splitting tensor [1] and is determined by electron–electron and ligand-field interactions [1].

The ESEEM spectra for electron spin $S=1$ interacting with a nucleus $I=1/2$ [103,104] have been described. However the existing ESEEM literature for $S=1$ refers almost exclusively to the study of organic triplets [103]; its application to metal centers is fairly limited. Quite recently, the $S=1$ ESEEM theory has been invoked in the analysis of deuterium modulations of the 'split-S_3 signal' of Photosystem II [105].

ESEEM data for a spin $S=3/2$, have been reported for the MoFe center of nitrogenase [106] and the iron-nitrosyl, $Fe^{2+}(S=2)$–NO, adduct of Photosystem II [107] while ESEEM spectra for $S=5/2$ have been reported for the high-spin $Fe^{3+}(S=5/2)$ of transferrin [108]. In all three cases the zero field splitting parameter, D, is much larger than the Zeeman energy at X-band, $D \gg h\nu \sim 0.3\ cm^{-1}$, therefore the EPR spectrum can be described by an effective spin $S_{eff}=1/2$ [1] with effective g-values at $g_{\perp} \sim 4$ and $g_{\parallel} \sim 2$ for the $S=3/2$ systems [106,107], and $g_x \sim g_y \sim g_z \sim 4.3$ for the middle Kramer doublet in $Fe^{3+}(S=5/2)$ transferrin [108]. In the effective $S'=1/2$ representation the effective hyperfine tensor becomes [1,109,110]

$$\boldsymbol{A}_{eff} = \boldsymbol{A}\cdot\boldsymbol{g}_{eff}/2 \tag{26a}$$

where the denominator 2 is an approximation of the electronic g-tensor. For collinear **A** and **g**

$$\boldsymbol{A}_{eff} = 1/2 \begin{pmatrix} A_X g_X & 0 & 0 \\ 0 & A_Y g_Y & 0 \\ 0 & 0 & A_Z g_Z \end{pmatrix} \tag{26b}$$

from which it is seen that even for a purely isotropic intrinsic hyperfine tensor, the effective tensor may be strongly anisotropic e.g. when $\boldsymbol{g}_{eff}$ is anisotropic. Having embodied all the zero-field splitting terms in the effective g-tensor, the ground state of the system can be described by the effective spin-Hamiltonian

$$H = \boldsymbol{g}_{eff}\cdot\beta\boldsymbol{B}\cdot\boldsymbol{S}' + g_n\beta_n\boldsymbol{I}\cdot\boldsymbol{B} + \boldsymbol{I}\cdot\boldsymbol{A}_{eff}\cdot\boldsymbol{S}' + \boldsymbol{I}\cdot\boldsymbol{Q}\cdot\boldsymbol{I} \tag{27}$$

for $\boldsymbol{S}'=1/2$ [1]. Then, the ESEEM spectra of $S=3/2$, $5/2$ for $D \gg h\nu$, can be described by the formalism of Mims for $S=1/2$ [106–108].

The case of spin $S>1/2$ with zero field splitting comparable with the Zeeman energy, $D \sim h\nu$, is more complicated since in this case the effective $\boldsymbol{S}'=1/2$ spin-Hamiltonian formalism is not applicable [1]. The manganese ion $Mn^{2+}(S=5/2)$ is the typical example of this case. The theory of two-pulse ESEEM for weakly coupled $I=1/2$ nuclei interacting with an $S=5/2$ electron spin has been described by two different groups [83,111]. In Ref. [83], the analysis was based on a simplified picture where the total ESEEM is considered to be the sum of contributions from transitions between successive M_S levels. Then the theory of ESEEM for $I=1/2$

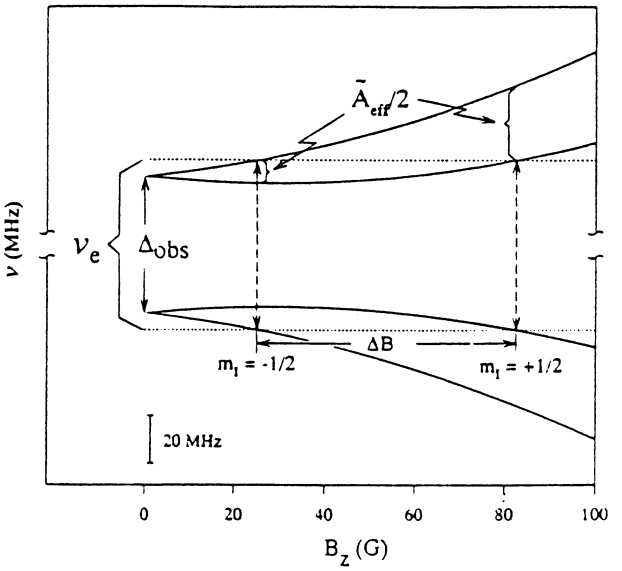

Fig. 10. Energy levels for a non-Kramer doublet interacting with a single $I = 1/2$ nucleus. Parameters: $\Delta = 9200$ MHz, $A\| = +160$ MHz. The M_S manifolds have been shifted in energy to allow both on the same figure; the parallel lines span the microwave frequency taken as $\nu_e = 9220$ MHz. The figure depicts the hyperfine splitting, $\Delta B = \Gamma\|/g\|\beta = A\|/g\|\beta$, observed in field swept EPR. The two vertical braces represent the hyperfine splitting, $\Gamma_{eff}/2$, of the $M_S = +1/2$, $M_I = \pm 1/2$ energy levels to the fixed field where the individual $M_I = -1/2$ and $+1/2$ EPR transitions are in resonance. The observed zero-field splitting is $\Delta_{obs} = [\Delta^2 + (\Gamma\|/2)^2]^{1/2}$, and are independent of the nuclear states M_I. Reprinted form Ref. [116] after permission. Copyright 1994 American Chemical Society.

was adapted to take into account the proper expectation values of $\langle S \rangle$ [83]. A more elaborated analysis, based on the density-matrix formalism, was carried out by Coffino and Peisach [111] who conclude that the zero-field splitting term, although assumed to be small, gives rise to angle selection effects in ESEEM spectra of Mn^{2+} ($S = 5/2$). The angle-selective phenomenon was not predicted in Ref. [83]. So far, the theory for other, interesting and commonly encountered cases, i.e. ESEEM due to ^{14}N($I = 1$) couplings to Mn^{2+} ($S = 5/2$), is not available.

3.7. ESEEM of non-Kramer doublets (NK-ESEEM)

Molecules with an odd number of electrons necessarily exhibit degenerate doublets in zero magnetic field, characterized by half-integer spin, $S = 1/2$, 3/2, 5/2 [1]. A non-zero-applied field splits these so-called 'Kramer' doublets, and this permits their interrogation by EPR spectroscopy [1]. Molecules with an even number of electrons, characterized by integer spin, do not necessarily exhibit degenerate energy states in zero field, and thus are commonly EPR-silent. However, certain even-electron systems with integer total angular momentum $J = L + S \geq 2$, may exhibit a quasi-degenerate doublet that in zero-field is split by an energy Δ [1], see Fig. 10.

It was first observed by Bleaney [112] and analysed rigorously be Griffith [113] that 'non-Kramer' EPR spectra with enhanced intensity can be detected for such integer spin systems, in cases of near axial zero-field splitting which is of the order of the microwave energy e.g. $\Delta \sim 0.3\text{cm}^{-1}$ at the X-band. In order to achieve the maximum intensity in these 'non-Kramer' EPR spectra, the static $\boldsymbol{B}$ and the microwave field $\boldsymbol{B}_1$ have to be parallel to each other i.e. $\boldsymbol{B}_1 \parallel \boldsymbol{B}$, while for half-integer spin $\boldsymbol{B}_1 \perp \boldsymbol{B}$ [1]. Such 'non-Kramer' EPR spectra are characterized by large effective g-values, e.g. typical values are $g \sim 8$ for $Fe^{2+}(S=2)$ [114] and $g \sim 16$ for the oxidized P clusters ($S=3$ or 4) of nitogenase [115]. In the case of spin-coupled clusters the interplay between exchange and zero-field splitting terms can leave one or more nearly degenerate non-Kramer doublets [115,116]. For single ions, non-Kramer EPR spectra can be described by a fictitious spin $S_{\text{eff}} = 1/2$, with an effective g-tensor for which the case of axial symmetry has the form [113,116]

$$\tilde{g}_{\text{eff}} = [\tilde{g}_\perp, \tilde{g}_\perp, \tilde{g}_\parallel] = [0, 0, (2J)g_\parallel] \tag{28}$$

where $J = L + S$, (becomes $J = S$ for systems with quenched orbital momentum, $L = 0$), $g\|$ is defined in the true spin-Hamiltonian ($g\| \approx 2$ for $L = 0$).

In the presence of a nucleus with spin I, the resonance condition for a non-Kramer system is

$$(h\nu_e)^2 = (\beta\tilde{g}_\parallel B \cos\theta + m_I\tilde{A}_\parallel)^2 + \Delta^2 \tag{29}$$

with $\tilde{A}_\parallel = (2J)A_\parallel$ where $A_\parallel$ is the projection of the true spin-Hamiltonian along z. Non-axial terms reduce both $\tilde{g}_\parallel$ and $\tilde{A}_\parallel$ [113,116]. For coupled spins in clusters, Eq. (29) is still valid but the expression for $\tilde{g}_\parallel$ is now given by the projection of $2Jg_\parallel$ on the cluster z axis, while $\tilde{A}_\parallel$ is given by the projection of the component of $2JA_\parallel$ along the ion's crystal-field axis, on the cluster's z axis [116]. The energy difference between the states m_I and $m_I - 1$ is

$$|E_{(m_I)} - E_{(m_I-1)}| = \tilde{A}_\parallel(\beta\tilde{g}_\parallel B\cos\theta)/2h\nu_e = (1/2)\tilde{A}_\parallel\left(\frac{b}{(1+b_z^2)^{1/2}}\right) \tag{30}$$

where b_z is the reduced field $b_z \equiv \beta\tilde{g}_\parallel B\cos\theta/\Delta$. This energy difference is the effective hyperfine interaction

$$\tilde{A}_{\text{eff}} = \tilde{A}_\parallel\left(\frac{b_z}{(1+b_z^2)^{1/2}}\right) \tag{31}$$

which determines the ENDOR spectrum [116]. The effective hyperfine interaction depends (a) on the intensity (B) and (b) the direction ($\cos\theta$) of the applied magnetic field with respect to the molecular z-axis. Thus at low B values, typical for the non-Kramer doublets, the effective hyperfine coupling is significantly smaller than the $\tilde{A}_\parallel$ value [116]. These small effective hyperfine couplings fail to cause significant mixing of the semiforbidden and allowed EPR transitions, which is the prerequisite for non-zero ESEEM [3]. In this context, nuclei with strong hyperfine coupling, e.g. from directly coordinated nuclei, are expected to give rise to deeper modulations than the remote nuclei.

In summary, for nuclei with $I = 1/2$ (^{1}H, ^{19}F, ^{15}N, ^{13}C, ^{31}P) the modulation depth varies quadratically with the nuclear g_n factor [116]; therefore, protons are expected to give $[g_n(^{1}H)/g_n(^{15}N)]^2 \sim 100$ fold deeper modulations than ^{15}N nuclei having the same hyperfine couplings. On the other hand the presence of a significant quadrupole interaction may enhance the mixing of the semiforbidden and allowed EPR transitions; in metal complexes this is typically encountered for ^{14}N, and probably for ^{17}O [116]. For nuclei with $I > 1/2$ but with negligible quadrupole interaction (^{2}H), no ESEEM is expected for non-Kramer doublets. In the case of ^{14}N, the NK-ESEEM spectrum originates from the three pure nuclear quadrupole transitions ν^+, ν^- and ν^0, given in Eq. (20), which for small magnetic fields ($B < 20$ G) shift linearly with B. Only nuclei with $I \geq 1$ and with significant quadrupole couplings such as ^{14}N($I = 1$) and possibly ^{17}O($I = 5/2$) for biomolecules, are likely to give useful NK-ESEEM signals at low fields. The theoretical predictions have been verified in recent pioneering applications of the NK-ESEEM in various diferrous carboxylate bridged non-heme iron proteins [117,118].

4. The working tools in ESEEM spectroscopy, perspectives and limitations

Among the primary challenges of ESEEM spectroscopy is to enhance the observability of spectral lines, to simplify the interpretation of the spectra by forging direct links between their features and the spin couplings to be measured. In considering methods through which this goal can achieved, we recall the main experimental strategies usually adopted [7]. One concerns manipulation of the internal spin-Hamiltonian parameters by isotopic labeling of the sample, a second is post-acquisition manipulation of the spectra in order to show forth specific contributions, e.g. by dividing time-domain spectra, and a third is manipulation of the spin interactions with the external magnetic field, e.g. by varying the magnetic field and/or the microwave frequency.

4.1. Isotopic labeling

In certain cases, replacement of a naturally non-magnetic nucleus by a magnetic isotope allows detection of ESEEM signals; in this case the assignment of the signal is straightforward. Examples include the substitution of the naturally abundant isotopes of carbon, ^{12}C($I = 0$) and oxygen ^{16}O($I = 0$) with ^{13}C($I = 1/2$, natural abundance 1.11%) and ^{17}O($I = 5/2$, natural abundance 0.04%), respectively. Usually ESEEM from nuclei with low-natural abundance cannot be resolved, except in certain, rather rare, cases [119].

^{13}C-modulations have been detected in ESEEM spectra from ^{13}C-[pyruvate] in Mn^{2+}·*N*-Ras21 [120], VO-pyruvate kinase [121], and VO-transferrin [122], from ^{13}C-[oxalate] in VO-transferrin [123], Cu-transferrin [124] and Cu-conalbumin [125], in Cu-[^{13}C]carbonate [178], in ^{13}C-labeled absorbates, in Cu^{2+}- ZSM-5 zeolites [127] and in *t*-(^{13}CH)$_X$ radicals [128].

In general, the ESEEM spectra of $^{17}O(I = 5/2)$ are expected to be complicated [82] due to its high nuclear spin ($I = 5/2$), low gyromagnetic ratio (2.02 MHz at 3.5 kG) and large quadrupole moment. ^{17}O modulations have been resolved in the ESEEM of the S_2-state of the Mn-cluster of the OEC of Photosystem II suspended in $H_2^{17}O$ [129] and in cytochrome P_{450}cam [130]. Attempts to observe ^{17}O-modulations in ESEEM of Mn^{2+}-creatine kinase complexes with ^{17}O-labeled ADP were unsuccessful [131].

Exchanging a magnetic nucleus with another magnetic isotope of the same atom, allows direct assignment of the pertinent modulations, and may result in improved resolution: typical examples include the $^{14}N(I = 1)/^{15}N(I = 1/2)$ and $^{1}H(I = 1/2)/^{2}H(I = 1)$. ^{15}N-labelling has been used in ESEEM studies of NO-heme-imidazole [132], in Mn^{2+}-glutamine synthase [133], VO-[imidazole]$_n$ [88,134], Cu-[imidazole]$_4$ [135,136], a Cu^{2+}-pyridine complex [137], superoxide dismutase [69], VO-[*S*-adenosylmethinine synthetase] [138], CN–Fe^{3+} in adenylate kinase [139], flavine radicals [96], the semiquinone and pheophytin radicals of Photosystem II [66,86], the Mn-cluster of the OEC of Photosystem II [140–142], the semiquinone A1 [143] and the primary electron donor P_{700} [144] of Photosystem I, and bacteria [97], particulate methane monoxygenase [145], Mn^{2+} complexes of the *N*-ras21 protein [146] and a CN–Mn(III)–Mn(IV) complex [67].

4.2. Multifrequency ESEEM

The salient properties of the ESEEM spectral features, that are strongly influenced by the strength of the external field, are the frequencies of the nuclear transitions, their amplitude and dispersion of the fundamental [78] or combination [147] lines. The dispersion of the frequencies from anisotropic spin interactions can be manipulated by variation of the external magnetic field. Singel and co-workers have demonstrated that line narrowing through removal of the dispersion, is achieved when the nuclear Zeeman frequency assumes particular values determined by the hyperfine couplings [78,147].

For $I = 1/2$ with axial hyperfine interaction, line narrowing occurs for $4\nu_I = 2A_{iso} + T$ or $2\nu_I = A_{iso} - T$ resulting in strong, sharp spectral features at frequencies $3T/4$ and $A_{iso} - T$, respectively [78], see also Fig. 4. Proton couplings close to matching at the X-band, leading to intense modulations have been observed for the OH^- bridge in mixed valent Fe(II)–Fe(III) forms of hemerythrin and methane mono-oxygenase [148] and the stable tyrosine radical of Photosystem II [149].

For $I = 1$ with purely isotropic hyperfine interaction, line narrowing occurs in the cancellation condition i.e. for $2\nu_I = A_{iso}$ resulting in sharp spectral features, see Fig. 5, at frequencies given by relations 20, 21 [78].

Performing ESEEM experiments at various frequencies provides a means by which the line-narrowing conditions can be met. In addition to the lucrative line-narrowing, multifrequency ESEEM offers other advantages [7,78]: First in a system comprised of several nuclei with distinct hyperfine couplings, the external field could be chosen to accentuate the contributions of some but attenuate the contributions of other spins to the ESEEM spectrum. Multifrequency ESEEM has

been developed and used in various experiments by Singel and co-workers (see Ref. [78] and references therein) who also explored the beneficial application of line-narrowing in studies of combination-lines by ESEEM, e.g. two- and four-pulse experiments [147] and orientation selective ESEEM [136].

Optimisation of the echo modulation for strongly coupled nuclei can be achieved by performing ESEEM experiments at high microwave frequencies [150] e.g. significantly higher than the frequencies of 8–12 GHz usually employed for ESEEM. An elegant pertinent example is the ESEEM experiments performed at THE W-band (95 GHz), for Cu^{2+} in single crystals of azurin at ~ 3.5 T, which allowed the resolution of deep modulations originating from the directly coordinated ^{14}N from His-117 and His-46, with hyperfine couplings of 25 and 17 MHz, respectively [151]. An additional advantage of performing experiments at high frequency, is the possibility to have single-crystal like orientation selection due to increased spectral resolution in the continuous wave (c.w.) EPR spectrum. Moreover, at high magnetic fields the spectral resolution of the ESEEM spectra in the nuclear-frequency dimension [150] is increased; for example hyperfine lines of nuclei with neighboring Larmor frequencies at the X-band (e.g. ^{14}N, ^{15}N, ^{2}H, ^{13}C) will be well separated, by a factor of 10, at the W-band [150].

5. Interpretation of the spin-Hamiltonian parameters and relation to structure

5.1. Anisotropic hyperfine interaction

The geometric information obtained by ESEEM that is most directly related to interatomic distances derives from the anisotropic portion of the electron–nuclear hyperfine interaction. For numerous metal complexes where the interaction concerns the electron spin and ligand nuclei, the hyperfine interaction is often axially symmetric [1]. To the extent that the hyperfine interaction can be modeled as a simple interaction between electron and nuclear point magnetic dipoles, the anisotropic hyperfine coupling provides a simple measure of the electron–nuclear distance, see Eq. (6a) for the $\boldsymbol{A}$-tensor. For an isotropic electronic $\boldsymbol{g}$-tensor, the dipolar interaction is simplified to the well-known form

$$T = gg_n\beta\beta_n/r^3 = C/r^3 \tag{32}$$

where for T in MHz units and r in angstroms (Å), the factor $C \sim 5.7$ for ^{14}N ($g_n = 1.077201$), $C \sim 78.9$ for ^{1}H ($g_n = 14.90218$) and $C \sim 12.1$ for ^{2}H ($g_n = 2.287575$).

The main factors, which may limit the applicability of the point dipole model include (a) highly delocalized electron spins, which produce anisotropic hyperfine couplings not describable by a point dipole model, (b) local p spin-densities often produce anisotropic hyperfine couplings. An electron spin occupying a p orbital generates anisotropic hyperfine interaction at a nucleus located at the center of the orbital. This hyperfine anisotropy is of dipolar origin [152] and may be written in a matrix form $\boldsymbol{A}_{\text{orbital}}$ which adds to the through-space dipolar part $\boldsymbol{A}_{\text{dipolar}}$. The

final form of the $\boldsymbol{A}$ tensor depends on the relative orientations of the $\boldsymbol{A}_{\text{dipolar}}$ and $\boldsymbol{A}_{\text{orbital}}$. For the case of collinear $\boldsymbol{A}_{\text{dipolar}}$ and $\boldsymbol{A}_{\text{orbital}}$ tensors the total $\boldsymbol{A}$ tensor has the axial form

$$A = \begin{pmatrix} A_{\text{iso}} - T - A_{\perp} & 0 & 0 \\ 0 & A_{\text{iso}} - T - A_{\perp} & 0 \\ 0 & 0 & A_{\text{iso}} - 2T - 2A_{\perp} \end{pmatrix} \tag{33}$$

For the case where the two axial tensors $\boldsymbol{A}_{\text{dipolar}}$ and $\boldsymbol{A}_{\text{orbital}}$ tensors are not collinear the resultant tensor $\boldsymbol{A}$ becomes rhombic [152–154].

Deuterium ESEEM with improved modulation depth is often used to study proton couplings. In estimating the electron-deuterium distance the quadrupole interaction is frequently neglected. Mims et al. [155] estimated that neglecting the deuterium quadrupole interaction would lead to no more than a 10% underestimate of interatomic distances.

5.2. Isotropic hyperfine interaction

The sign of the isotropic hyperfine interaction is indicative of its quantum mechanical origin: direct, through-bond spin transfer puts positive spin density at the nucleus corresponding to positive A_{iso} [152]. In this case an axially symmetric $\boldsymbol{A}$ tensor with $A_{\text{iso}} > T > 0$, the tensor will have the form $[A_x, A_y, A_z] = [A_{\text{iso}} - T, A_{\text{iso}} - T, A_{\text{iso}} + 2T]$ with $A_x, A_y < A_z$. On the other hand, spin polarization of filled orbitals generates negative spin density at the nucleus i.e. $A_{\text{iso}} < 0$ [152]. In this case the A_z component is the smallest $A_z < A_x, A_y$, and the hyperfine tensor will have the form $[A_x, A_y, A_z] = [-A_{\text{iso}} - T, -A_{\text{iso}} - T, -A_{\text{iso}} + 2T]$.

In general the ESEEM spectra are not sensitive to the sign of the hyperfine coupling parameter. Nevertheless, in certain cases the determination of the relative sign of the isotropic versus the anisotropic hyperfine parameters is possible. In model low-spin iron heme complexes and myoglobin, the A_z value for the coupling of the axial ^{14}N was found to be the smaller, both by ESEEM [155,156] and ENDOR [154]. This was interpreted as being due to a negative A_{iso} which in turn means that the spin density is transferred through a spin-polarisation mechanism and not via a, more intuitive, direct spin transfer through the σ-bond between the metal and the imidazole [156]. As another example, Dikanov et al. [135] found that the A_{iso} and T of ^{15}N nuclei in Cu^{2+}-[imid]$_4$ have opposite sings. This was achieved for these specific ^{15}N couplings, which fulfil the 'matching condition' e.g. $(2A_{\text{iso}} + T) = \pm 4\nu_I$, after having determined the value of $|T|$ from sum and difference combination lines from detailed consideration of two- and four-pulse ESEEM [135].

The isotropic hyperfine coupling observed for atoms in ligands of metal complexes arises from the interaction between the nuclear spin and unpaired electron spin f_s in s orbitals of the ligand atom [1]. Thus the isotropic hyperfine coupling provides a measure of the spin density at the interacting nucleus. For the general case of a metal complex with m unpaired electrons having total spin $S = m \cdot \frac{1}{2}$, the relationship between f_s and A_{iso} is

$$A_{iso} = \frac{f_s A_s}{2S} \tag{34}$$

where A_s is the hyperfine coupling for a unit spin density at the specific nucleus. A_s values have been tabulated by Morton and Preston [157].

5.3. Nuclear quadrupole coupling parameters

Nuclear quadrupole couplings (NQC) in molecules are in general only qualitatively understood. Therefore the analysis of the experimental NQC is usually based on a simplified model originally proposed by Towens and Dailey [158]. According to Towens–Dailey the observed quadrupole parameters are related to the electron population of an atom. The Towens–Dailey approach simply assumes that the electric field gradient on a nucleus is due to different populations of the three p orbitals $2p_x$, $2p_y$ and $2p_z$. Multicenter electronic and lattice contributions are neglected; s-electrons do not contribute because of spherical symmetry. The model yields the following relations between the experimental coupling constant in the particular molecule $(e^2qQ/h)_{mol}$ and the population numbers N_j (assuming that p_z points to the metal):

$$f = \frac{(e^2qQ/h)_{mol}}{(e^2qQ/h)_{at}} = -N_z + \frac{(N_x + N_y)}{2} \tag{35a}$$

and

$$f \cdot \eta = \frac{3(N_x - N_y)}{2} \tag{35b}$$

where $(e^2qQ/h)_{at}$ is the experimentally determined value for the free atom [159]. A modified Towens–Dailey analysis based on a sp^n hybrid orbital picture for ^{14}N nuclei, developed in order to interpret NQR data [160] can also be used for the interpretation of ESEEM data [161].

The measured NQC parameters may serve as a reference for the identification of the molecule bearing the interacting nucleus. In certain cases, the NQC parameters can be correlated with specific structural–electronic properties of the molecule. For example, in Cu^{2+}-imidazole compounds the variation in the e^2qQ/h values of the remote, non-coordinated amino nitrogen, is influenced by the presence of hydrogen bonding [160,161]: hydrogen bonding decreases the e^2qQ/h value along with an increase in η. Substitution at the remote nitrogen of the imidazole results in an increase in the e^2qQ/h value along with a decrease in η [161,162]. On the other hand, in the case of imidazole axially coordinated to heme iron, the mechanism of the observed variation in the e^2qQ/h value is attributed to σ-bonding between the imidazole and the iron [156]. The e^2qQ/h value for ^{14}N in substituted hydroxamates coordinated to VO^{2+} was found be 3.8–4.0 MHz [163] which is significantly lower than the value for hydroxamic acid (4.6–5.2 MHz). This reduction was attributed to electron redistribution upon binding of the hydroxamates to VO^{2+} [163].

The Euler angles of the nuclear quadrupole tensor, can be related to the molecular geometry of the complex if the orientation of the principal axes of the

nuclear quadrupole tensor is known. ESEEM data obtained for ^{14}N-quadrupole tensors in single crystals of Cu^{2+}-doped-L-histidine monochloride monohydrate show that the principal direction of the quadrupole tensors are mainly connected with the ligand molecule itself and thus can effectively be utilized to characterize the ligand orientation in the copper complexes [164]. Analogous conclusions may be envisaged for other metals and/or ligands, but only after experimental verification, e.g. by singe-crystal studies.

5.4. Quantitation of ligands

One of the strengths of ESEEM spectroscopy, is the ability to quantify the number of coupled nuclei associated with a paramagnetic center [7]. For example, where more than a single imidazole is coupled to Cu^{2+}, the result is the appearance of combination lines in the ESEEM spectrum [165]. For example, when the electron spin of Cu^{2+} is coupled to a single 2-methyl imidazole, as in the Cu^{2+}-diethylene-triamine complex, a four line spectrum is seen as in Fig. 11, with three sharp lines plus one broad double quantum transition. As the number of interacting, equivalently coupled nuclei is monotonically increased from one to four, additional lines

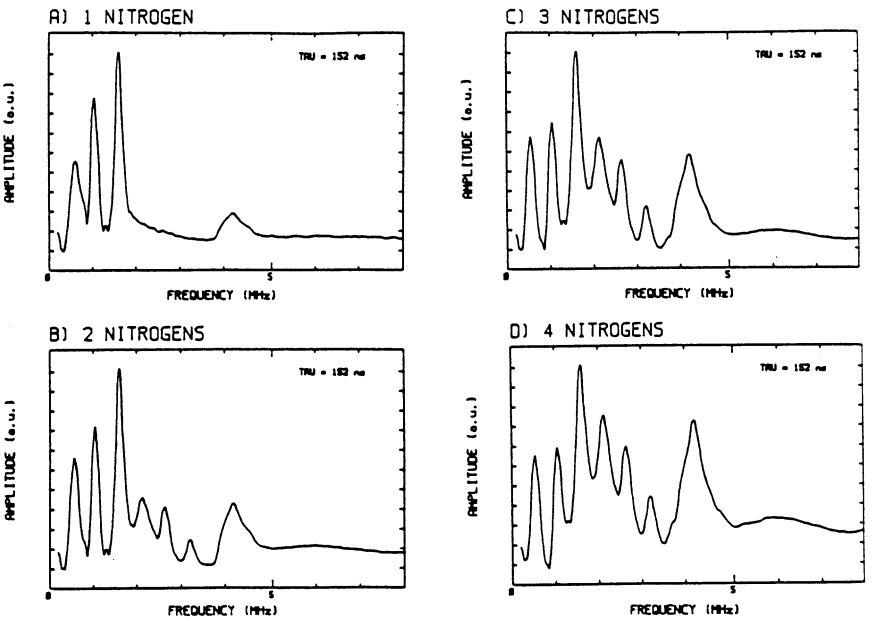

Fig. 11. Fourier transform of three-pulse ESEEM simulations. For (A) one ^{14}N contributes to the ESEEM data; (B) two equivalent nitrogens; (C) three equivalent nitrogens; (D) four equivalent nitrogens. The lines appearing in the region 2–4 MHz are combinations of the basic frequencies. Analysis of their intensity relative to the basic lines, together with the intensity of the broad double quantum line at $\sim$4.5 MHz, allows quantitation of the number of contributing ^{14}N nuclei. Reprinted form Ref. [165] after permission. Copyright 1988 American Chemical Society.

appear in the spectrum whose frequencies are the combination of the nuclear quadrupole frequencies of the mono 2-methyl imidazole complex, Fig. 11.

Based on computer simulations and comparison with appropriate model systems, when available, one can eventually determine the number of coupled nuclei.

6. ESEEM characterization of model compounds and metalloproteins

Metal ions serve a variety of functions in proteins, the most important of which is to enhance the structural stability of the protein in the conformation required for biological function and/or to participate in the catalytic processes of enzymes [166,167]. Metal ions can activate chemical bonds and make them more amenable to reaction. They can participate in trigger and control mechanisms by specifically altering or stabilizing a macromolecular conformation on binding. Certain metals can also undergo redox reactions.

The major metal-binding amino acids side-chains in proteins are carboxyl (aspartic acid and glutamic acid), imidazole (histidine), indole (tryptophan), thiol (cysteine), thioether (methionine), hydroxyl (serine, threonine, and tyrosine) and possibly the amide groups (asparagine and glutamate, although generally via their side-chain carbonyl, rather than amino, groups). Protons (^{1}H, $I = 1/2$) and nitrogens ^{14}N($I = 1$) are the only, naturally-abundant, protein nuclei which can give ESEEM signals; other protein nuclei with non-zero nuclear spin (^{13}C, ^{17}O) have very low natural abundance and their contribution is not resolved.

6.1. Copper(II)

6.1.1. General characteristics

Copper complexes are well suited for EPR investigations, since the d^9 Cu^{2+} ion is subjected to Jahn–Teller distortion so that axial and equatorial coordination sites become easily distinguishable [2]. Copper-containing proteins often have binding sites with irregular geometries with one or more nitrogenous ligand [168,169]. For this reason, intensive investigations have been carried out on models containing nitrogen ligands as a means for understanding the chemistry of copper coordinated in proteins.

Many copper complexes tend to have an elongated octahedral or square pyramidal coordination geometry [169] with a $d_{x^2-y^2}$ ground state and EPR spectrum characterized by $g_\perp < g_\parallel$ [169]. In proteins as well as in models, various constrains may be imposed on the metal–ligand structure often leading to tetrahedral distortion. This is accompanied by a reduction in the EPR parameters $A\parallel$ and $g\parallel$ [169]. Another type of distortion of a copper site is brought about when the ion is forced into a trigonal bipyramidal coordination geometry, for example by binding to a tripodal pentadentate ligand [162,168]. Characteristic of this type of coordination symmetry is the reversal of the g-values $g_\perp > g_\parallel$ and a d_{z^2} ground state [162,168].

In both $d_{x^2-y^2}$ and d_{z^2} ground state complexes, the hyperfine couplings with directly coordinated ligands usually exceed by far the corresponding nuclear

Larmor frequencies at the X-band (~ 9.4 GHz); due to this no ESEEM is usually resolved for the coordinated nuclei [24,162,170] at the X-band. In contrast, more distant nuclei coordinated either equatorially (for $d_{x^2-y^2}$ ground-state [84,161] or axially (for d_{z^2} ground-state [162]) have weaker couplings, appropriate for ESEEM. A typical example is the coupling of the remote nitrogen of imidazole which is $A(^{14}N) \sim 1.7$ MHz in $d_{x^2-y^2}$ complexes [84,161] and ~ 10% larger, e.g. $A(^{14}N) \sim 1.9$ MHz, for d_{z^2} complexes [162], see Fig. 6.

Directly coordinated ligands at the axial position in $d_{x^2-y^2}$ ground-state complexes might have couplings suitable for ESEEM spectroscopy [137]. This was verified experimentally for Cu(benzyloacetonate)$_2$ with axially coordinated ^{15}N- or ^{14}N-pyridine, where field-dependent ESEEM data showed that the ^{15}N coupling of axial pyridine is weak, $\boldsymbol{A} = (1.45, 1.45, 0.09$ MHz) [137]. For such weak coupling, however, the ^{14}N-quadrupole tensor is dominant and this complicates the analysis of the ^{14}N-ESEEM [137].

6.1.1.1. Imidazole as a Cu^{2+} ligand. Spectroscopic data about the copper ligands in proteins very often indicate coordination with one or more histidine residues via one of the atoms of the imidazole ring [169]. For copper proteins, ESEEM spectroscopy has proven useful in various types of experiments: firstly to identify and quantify the number of interacting imidazoles at a copper site and secondly to determine the effect of hydrogen bonding or even metal coordination at the remote or amino nitrogen of histidine imidazole coordinated to Cu^{2+} [170].

Both amino and imino nitrogen atoms in imidazole are sp^2 hybrids, with three sp^2 orbitals forming σ bonds with N or C and H atoms, or accommodating a lone pair of electrons. The p orbital perpendicular to the heterocycle plane engages in the aromatic π bond [159–161]. In the gas phase, the pπ orbital of the amino nitrogen has the highest electron occupancy so that the largest quadrupole coupling, Q_{zz}, for N1, the protonated nitrogen of imidazole, occurs perpendicular to the heterocycle plane [159–161]. The near-equivalency of the two N–C bonds at N1, brings the direction of q_{yy} close to the N–H bond direction (17° off) and that of q_{xx} 20° away from the N1–C2 bond direction. For imidazole, the gas-phase value and the solid-state value, obtained by ESEEM, are quite different from each other. These solid- versus gas-phase differences ($e^2qQ/h = 2.54$ MHz, $\eta = 0.18$ in the gas phase [159] versus $e^2qQ/h = 1.42$ MHz, $\eta = 0.99$ in the solid-phase [160,161]) go beyond expectations for physical-state change and, as noted above, have been interpreted as arising from hydrogen bonding in the solid state which cannot occur in the gas-phase [161]. Structural adjustments in accord with hydrogen bonding effects in the solid state include an N–H bond length increase of 0.05 Å [161]. The quadrupole parameters are sensitive to alteration in the N–H bond polarization brought by hydrogen bonding [161]. As a consequence, in the solid state there is a significant change in the quadrupole coupling along the N–H bond and the principal direction of the smallest quadrupole coupling, q_{xx}, is now along N–H direction at N1 of imidazole, see Fig. 12. The principal direction with the largest quadrupole coupling, Q_{zz}, has switched from being perpendicular to the imidazole plane to being within the plane, Fig. 12 [161,171].

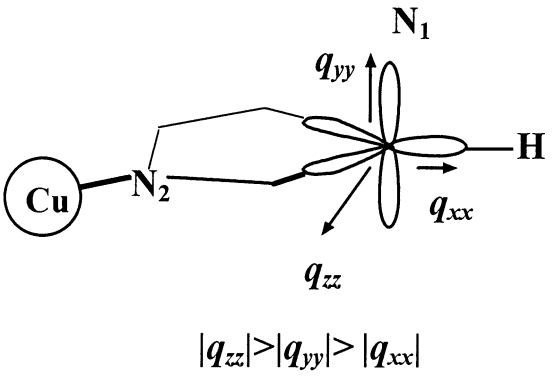

Fig. 12. The amino nitrogen atom in imidazole is sp^2 hybrid, with three sp^2 orbitals forming σ bonds with N or C and H atoms, or accommodating a lone pair of electrons. The p orbital perpendicular to the heterocycle plane engages in the aromatic π bond. In the solid state or in Cu complexes, the principal direction of the smallest quadruple coupling, q_{xx}, is along the N–H direction at N1 of imidazole. The principal direction with the largest quadruple coupling, Q_{zz}, is within the plane.

The replacement of a methyl group on C3 of the imidazole in Cu-dien–imidazole changes the electron distribution around N1, thereby affecting the quadrupole parameters. Such effects have been observed previously [161]. An analysis based on the Towens–Dailey model [158] suggested that the electron occupancy at the three sp^2 hybrid σ orbitals of N1 of the imidazole was altered by the change in the electron distribution at a ring carbon through an induction effect brought about methyl substitution [161].

According to this analysis, the quadrupole couplings — but not the hyperfine couplings — [161,162,172] of the remote ^{14}N of the coordinated imidazole, can serve as sensitive probes of structural details, not-discernible by any other means. For example, in isopenicillinate synthase Cu^{2+} is bound to two imidazoles in a nearly tetragonal geometry [173] very similar to that found in Cu^{2+}-doped Zn^{2+} (1,2-dimathylimidazole)$_2Cl_2$ [161]. In spite of the geometrical similarities, ESEEM data reveal differences in their electronic structure, e.g. the couplings for both the remote ^{14}N of imidazole are identical in Cu^{2+}-doped Zn^{2+}(1,2-dimathylimidazole)$_2Cl_2$ but clearly inequivalent in isopenicillinate synthase [173].

6.1.2. Cu^{2+} complexes

6.1.2.1. Cu^{2+}-(imidazole)$_n$. The Cu^{2+}-(imidazole)$_4$ complex is often considered to be a model system for histidine coordination in copper proteins; the pioneering ESEEM work of Mims and Peisach on Cu^{2+}-(imid)$_4$ [84] established that the hyperfine couplings of the remote ^{14}N is $A_{iso} = 1.75$ MHz, which is close to the 'cancellation condition' at the X-band, $A_{iso} = 2\nu_I$, and this results in deep modulations at the nuclear quadrupole frequencies, see Eqs. (20) and (21). Recently, a detailed orientation-selective investigation of Cu^{2+}-(imid)$_4$ with ^{15}N-labeled imidazoles, allowed an accurate evaluation of the hyperfine coupling of the remote

nitrogen, e.g. the ^{15}N couplings are $A_{iso} = 2.44$ MHz, $T = -0.39$ MHz, and determined the angle between the axial direction of the complex and the direction of the largest principal hyperfine tensor element as 40° [135]. In frozen deuterated aqueous solution (pD 7) in the presence of excess histidine, the predominant species is in a configuration where the cupric ion is surrounded by two imidazole N atoms plus two amino N atoms from the histidine and two water molecules [174].

The remote imidazole nitrogens have been found to contribute exclusively in the ESEEM spectra for copper complexes with Tris–histidine [Tr(His)$_3$]-based tripodal ligands [76]. The EPR spectra of these complexes, characterized by $g_\perp < g_\parallel$, imply an octahedral arrangement with trigonal distortion [76]. Based on numerical simulations of orientation selective ESEEM data it was concluded that in Cu^{2+}–Tr(His)$_3$ and Cu^{2+}–Ar(His)$_3$ the Cu^{2+} is coordinated to three imidazole rings whereas in Cu^{2+}-Tt(His)$_2$Met it is coordinated only to two imidazoyl rings. The pivotal nitrogen in Cu^{2+}-Tr(His)$_3$ is not coordinated to Cu^{2+}. From the Euler angles of the equivalent ^{14}N quadrupole tensors it was concluded that the binding site in Cu^{2+}-Tr(His)$_3$ and Cu^{2+}-Ar(His)$_3$ has the imidazoyl rings forming a propeller-like arrangement [76].

A novel approach for the chemical modeling of the active site of copper proteins has been published recently [175]. This procedure is based on the use of histidine molecules covalently bonded on an inorganic support, resulting in a hybrid organic–inorganic material [175]. Three-pulse ESSEM and HYSCORE studies of complexes formed by Cu^{2+} ions and the hybrid material, showed that the copper atom is coordinated by two inequivalent ($e^2qQ/h = 2.1$ MHz, $\eta = 0.11$, and $e^2qQ/h = 1.58$ MHz, $\eta = 0.84$) histidine imidazoles [175].

6.1.2.2. Cu-pyrazole, pyridazine. A structural isomer of imidazole is pyrazole. Both its amino and imino nitrogen atoms are sp^2 hybrids, with three sp^2 orbitals forming σ bonds with N or C and H atoms, or accommodating a lone pair of electrons and the p orbital perpendicular to the heterocycle plane engages in the aromatic π bond [172]. However, there is much less electron occupancy at the N–N σ orbital of pyrazole as compared to imidazole, due to the higher electronegativity of the bonding atom, i.e. a N atom as compared to a C atom. This makes the inequivalency of the N–H bond and the N–C bond of pyrazole N1 less significant so that the principal direction of the second largest quadrupole coupling, q_{yy}, is almost along the N(1)–N(1) bond direction (5° off) and that of the weakest quadrupole coupling, q_{xx}, lies almost 23° away from the N(1)–H bond direction [172]. As a consequence of the higher asymmetry in electron distribution at the three bonding sp^2 orbitals in the pyrazole plane, a larger quadrupole coupling constant and a larger asymmetry parameter are observed for pyrazole than for imidazole [172]. The quadrupole coupling constant e^2qQ/h obtained for N1 of pyrazole by ESEEM is larger than the value for N1 of imidazole, while the asymmetry parameter η is smaller [172]. It is noteworthy that the NQR values obtained for pyrazole by ESEEM are not very different form the NQR values in the gas phase ($e^2qQ/h =$ 3.02 MHz, $\eta = 0.52$ in the gas phase versus $e^2qQ/h = 2.86$ MHz, $\eta = 0.74$ in the Cu-complex). In pyrazole, the N–H bond direction is away from the principal axis

of the quadrupole tensor, so that any change of N–H bond polarization has less influence on the principal values of the quadrupole coupling. The principal directions are nearly retained. Although a decrease in e^2qQ/h and an increase in η are observed for pyrazole in the Cu(dien) complex as compared to the gas phase, no profound effects of hydrogen bonding quadrupole parameters is observed as was found with the imidazole.

The quadrupole parameters of nitrogens in other heterocycles, which are not engaged in hydrogen bonding remain unaltered. For example in pyridazine, quadrupole parameters of the non-coordinated, non-protonated nitrogen are found to be similar in free pyridazine and in the Cu-complex ($e^2qQ/h = 5.35$ MHz, $\eta = 0.03$) [172].

6.1.2.3. Cu-thiochrome. The reaction of Cu(II) with 2-(α-hydroxybenzyl)thiamine, an active intermediate of the enzymatic cycle of thiamine, in methanolic solutions produced Cu(I) and thiochrome. The crystal structure of the Cu^{II}(thiochrome)Cl_2 complex, formed from the reaction media, comprised an infinite array of Cu(thiochrome)Cl_2 neutral units linked together through the N(4′a) and N(1′) atoms of thiochrome, coordinated to Cu(II). The copper atom was tetracoordinated with a weak Cu···N(3′) interaction in a compressed tetrahedral environment (Fig. 13) [176].

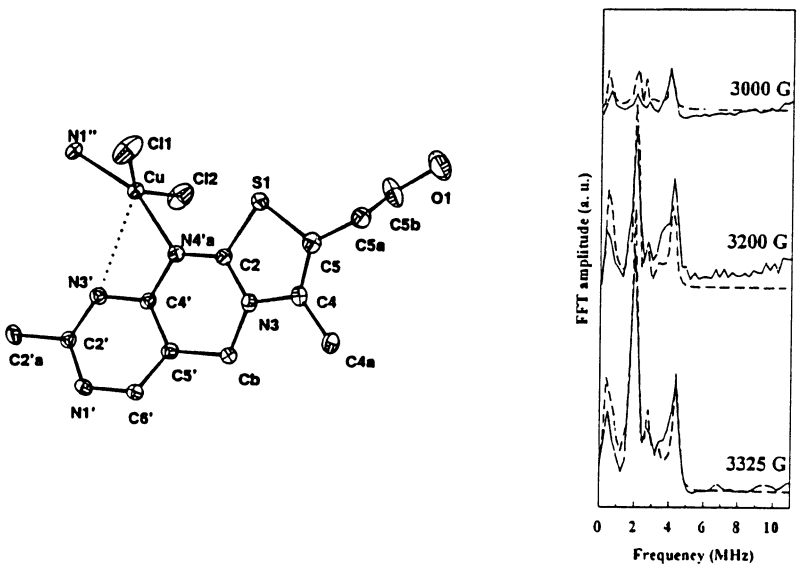

Fig. 13. Crystal structure of Cu^{II}(thiochrome)Cl_2. Experimental (solid lines) and simulated (dashed lines) orientation selective three-pulse ESEEM data. The magnetic interaction between the N(3′) of the pyrimidine ring and the copper $d_{x^2-y^2}$ electron spin is detected by ESEEM spectroscopy. The coupling parameters are ($A_x = 1.6$ MHz, $A_y = 1.4$ MHz, $A_z = 1.0$ MHz, $e^2qQ = 3.1$ MHz, $\eta = 0.25$). Reprinted form Ref. [176] after permission. Copyright 1997 American Chemical Society.

In the Cu^{II}(thiochrome)Cl_2 complex the magnetic interaction between the N(3′) of the pyrimidine ring and the copper $d_{x^2-y^2}$ electron spin was detected by ESEEM spectroscopy [176]. The ESEEM data showed the existence of a weak interaction ($A_x = 1.6$ MHz, $A_y = 1.4$ MHz, $A_z = 1.0$ MHz) between the Cu unpaired electron spin and the nucleus of the $^{14}N(3')$ of the pyrimidine ring, providing structural information which is in agreement with the crystal structure. The quadrupole parameters ($e^2qQ = 3.1$ MHz, $\eta = 0.25$) show that the electron distribution on the pyrimidine ring in Cu^{II}(thiochrome)Cl_2 differs substantially from that in crystalline pyrimidine mainly due a difference in the C–N–C angle [176].

6.1.2.4. Cu–NO_2^-. The coordination properties of the nitrite ion NO_2^- with copper have been investigated by the orientation selective ESEEM of Cu^{2+}(TEPA)NO_2]PF_6 (TEPA = tris[2-(2-pyridil)ethyl]amine) [177]. In frozen solution, the ^{14}N ESEEM indicates that nitrate binds to copper as an equatorial ligand through oxygen, rather than nitrogen [177]. Analysis of the quadrupole parameters ($e^2qQ = 5.66$ MHz, $\eta = 0.31$), which are similar to those for diamagnetic species, suggests that the O–N–O angle is 111–116° in frozen solution, as compared to 115° in the crystal. In hemocyanin treated with nitrite, ESEEM signals, as those detected in Cu^{2+}(TEPA)NO_2]PF_6, were not detected indicating that nitrite does not coordinate to hemocyanin, contrary to what was claimed previously [177].

6.1.2.5. Cu-carbonate. Recently the pH dependent complexation between Cu^{2+} and ^{13}C-labeled carbonate ligands was investigated by four-pulse ESEEM, HYSCORE and ENDOR [178]. At pH 5.5 small ^{13}C hyperfine couplings, e.g. $A(^{13}C) = (0.1, 0.1, 3.5 \pm 0.3$ MHz), was observed and assigned as monodentate coordination of carbonates to Cu^{2+} ion.

At pH 8, stronger ^{13}C couplings are observed, reaching the 'matching' regime [79], e.g. $A(^{13}C)$ becomes (4.0, 6.9, 9.0 ± 0.1 MHz), indicating a bidentate coordination. Proton sum combination peaks in four-pulse and shifts in HYSCORE ridges, Fig. 14, allow tracking of the number of coordinated water molecules as a function of the pH. In addition, axial and equatorial proton couplings are distinguished. At pH 5.5, two or three H_2O molecules are coordinated equatorially, while only one remains at pH 6.5 and none at pH 8. The two axially coordinated water molecules are not affected by pH [178]. Based on these data detailed structural models have been suggested.

To this end we wish to discuss an intriguing trend, first noticed by Kofman et al. [179], concerning the relationship between the experimental isotropic coupling A_{iso}, and the number of bonds between copper and the ligand nuclei: comparable couplings — after being scaled for the nuclear g factors — have been observed for atoms three bonds away from the metal, e.g. $A_{iso}(^{14}N) \sim 1.7$ MHz for the remote nitrogen of imidazole [84], $A_{iso}(^{14}N) = 1.25$ MHz in Cu^{2+}-bis(*N*,*N*-di-*n*-butyldithiocabamate) [180], $A_{iso}(^{14}N) = 1.3$ MHz for Cu-thiochrome [176], $A_{iso}(^{13}C) = 5.8$ MHz (scales to ~ 1.3 MHz for ^{14}N) for the $^{13}C_{3,4}$ in Cu-bis(*cis*-1,2-dicyanoethylenedithiolate) [181]. The couplings of directly coordinated nuclei are ~ 20 times stronger, i.e. $A_{iso}(^{14}N) = 39$ MHz in Cu-imidazole [90], $A_{iso}(^{33}S) = 35$ MHz (scales to 33 MHz for ^{14}N) in Cu^{2+}-bis(*N*,*N*-di-*n*-butyldithiocabamate) [180].

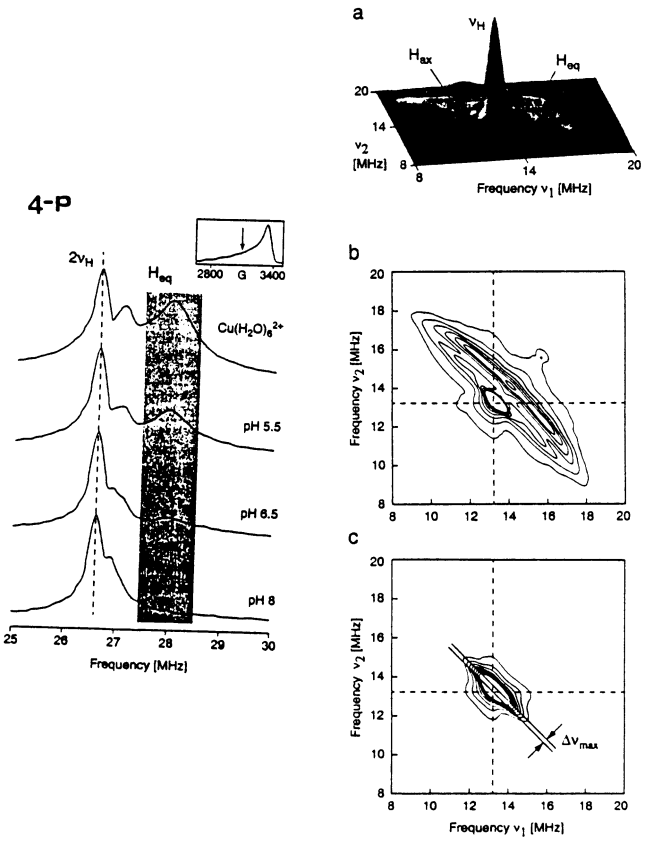

Fig. 14. (Left) Four pulse-proton ESEEM spectra of copper-hexaquo and copper-carbonate samples at different pH, recorded at $H = 3100$ G, indicated by an arrow in the echo detected EPR spectrum (inset) of the pH 5.5 sample ($\nu_{mw} = 9.72$ GHz, $T = 14$ K). The dashed line marks twice the proton Zeeman frequency, $2\nu_H$, at this magnetic field. The dashed area marks the shifted proton sum-combination frequencies, assigned to protons from equatorial water molecules. The peaks shifted by e.g. 0.5 MHz are due to protons of axially coordinated water molecules. (Right). HYSCORE spectra of copper-hexaquo complex (a,b) and a copper-carbonate sample pH 8 (c). In (a) a surface plot is presented, with the assignment of the spectral features to matrix protons (ν_H) and to protons at axial (H_{ax}) and equatorial (H_{eq}) water molecules. (b) Corresponding contour plot. The dashed lines indicate the proton Zeeman frequency. (c) Contour plot of the pH 8 sample with the same contour levels as in part (b). The maximum shift $\Delta\nu_{max}$ of the shoulders, marked by the two solid lines, is due to weak dipolar proton coupling. Reprinted form Ref. [178] after permission. Copyright 1997 American Chemical Society.

The ^{14}N coupling observed for the nitrogen located two bonds from copper, i.e. in pyridazine, $A_{iso}(^{14}N) = 2.6$ MHz [162], and in nitrite coordinated to $[Cu^{2+}(TEPA)]PF_6$, $A_{iso}(^{14}N) = 3.05$ MHz [177], fall intermediately between the couplings cited above for directly coordinated nuclei and those three bonds away from the metal. Surprisingly, for some nuclei two bonds away from the copper atom, the couplings appear to be comparable, or even smaller, compared with those for the nuclei three bonds away from the copper: $A_{iso}(^{14}N) = 1.4$ MHz in pyrazole [162],

$A_{iso}(^{14}N) = 1.3$ MHz in hydroxamates [179], A_{iso} (^{13}C) ~ 4 MHz (scales to ~ 1 MHz for ^{14}N) for the $^{13}C_{1,2}$ in Cu-bis(*cis*-1,2-dicyanoethylenedithiolate)[181]. In the Cu-hydroxamates, based on molecular orbital calculations, this relatively small coupling was attributed to a node in the molecular orbital at the nitrogen [179]. In the case of the monodentate coordination of carbonate, the ^{13}C nucleus two bonds away from copper has weak A_{iso}, e.g. 1.23 MHz [178]. This is increased significantly, e.g. becomes 6.6 MHz, for bidentate coordination of carbonate, due to more efficient π bonding, between the copper and the carbonate orbitals in bidentate Cu-carbonate [178]. The Cu-carbonate case recalls that the details of spin-delocalization — or configuration interaction, spin polarization where applicable — may invalidate simple geometry-based trends.

6.1.3. Copper-proteins

6.1.3.1. Superoxide dismutase. Superoxide dismutase (SOD) is a dimeric metalloprotein containing one Zn^{2+} and one Cu^{2+} ion per subunit, which dismutates the superoxide anion O_2^- into O_2 and H_2O. X-ray crystallographic data show that each Cu^{2+} ion is coordinated to four histidine residues (His-44, His-46, His-61, and His-118), see Fig. 15, [182]. In native ($Cu^{2+}Zn^{2+}$SOD) the hyperfine couplings of the remote nitrogens of the histidine ligands have been determined by X-band ESEEM study of ^{14}N-containing, i.e. unlabeled, [183] and ^{15}N-labelled SOD [69]. Based on the comparison of three- and four-pulse ESEEM for a model Cu^{2+}-(^{15}N imidazole)$_4$ compound [88], it was suggested that in SOD the remote nitrogens of His-46 and His-44 posses hyperfine interaction parameters, e.g. $A_{iso}(^{14}N) \sim 2.0$ MHz, $T = -0.26$ MHz, similar to those of the nitrogens in the model Cu^{2+}-(imid)$_4$ compound [88].

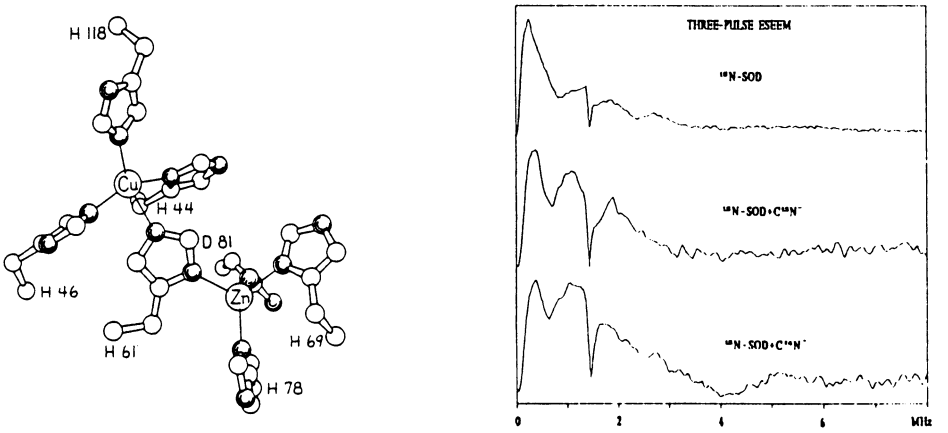

Fig. 15. (Left) The structure of superoxide dismutase (SOD), reprinted from Ref. [182] with permission. (Right) Three pulse ESEEM spectra of native ^{15}N-SOD, and of SOD bound with inhibitors ($C^{15}N^-$ and $C^{14}N^-$, respectively). The time domain ESEEM spectra have been recorded at 3300 G, 9.753 GHz for $\tau = 312$ ns. Reprinted from Ref. [88] with permission.

These imidazoles have their planes parallel to the direction of the maximal principal value of the g-tensor [88]. The two other nitrogens in SOD, from His-61 and His-118, have their imidazole plane tilted with respect to the other two histidines, with lower A_{iso} values e.g. $A_{iso}(^{14}N) \sim 0.67–1.0$ MHz [88]. Changes observed ESEEM data of ^{15}N-SOD inhibited with $C^{14}N$ or $C^{15}N$ were interpreted as indications that the hyperfine coupling of the nitrogen of cyanide is much stronger than the N-Larmor frequency. Based on this it was postulated that upon binding, His-46 is detached and CN binds to Cu^{2+} [88]. Specific removal of zinc from native SOD results in more homogeneous ESEEM spectra, reflecting more equivalent Cu–N_{ε} couplings due to the disruption of the imidazolate bridge [183].

Three-pulse ESEEM and ENDOR spectroscopy was applied to study the ($Ag_2^{1+}Cu_2^{2+}$SOD) derivative, which contains diamagnetic Ag^{1+} at the copper site and Cu^{2+} at the zinc site of the native protein [184]. It was found that the Cu^{2+} at the zinc site binds three imidazoles, one with strong Cu–N bonds, similar to that in the model Cu^{2+}-(imid)$_4$ compound, e.g. $A_{iso}(N_{\delta}) = 2$ MHz, $A_{iso}(N_{\varepsilon}) \sim 42$ MHz, and two with weak Cu–N bonds, e.g. $A_{iso}(N_{\delta}) \sim 1$ MHz, $A_{iso}(N_{\varepsilon}) \sim 28$ MHz. The NQI parameters showed that all the remote imidazole nitrogens are protonated, which indicates that the bimetallic imidazolate bridge, formed by His-61 in the native SOD, is broken in $Ag_2^{1+}Cu_2^{2+}$SOD [184].

6.1.3.2. Blue copper oxidases. Laccase, ascorbate oxidase and ceruplasmin, are members of blue copper oxidases containing metal ions at three different chemical environments, two of which, copper type 1 and copper type 2, give rise to EPR [169]. The third copper site, termed type 3, consists of a spin-coupled Cu^{2+} pair that is EPR silent. Ascorbate oxidase contains eight Cu^{2+} ions per molecule and consists of two identical laccase-like units [185]. Early ESEEM data showed that both type 1 and 2 copper in laccase [186,187] and ascorbate oxidase [187], and type 2 in ceruplasmin [186] are ligated to imidazole.

More recently, laccase and ascorbate oxidase were reinvestigated by ESEEM by two different groups [188,189]. One group studied the type 2 copper binding site in the Hg(II)-derivative of laccase in which the type 1 Cu^{2+} is substituted by Hg(II), an EPR silent surrogate [188]. It has been determined that the imidazole groups of two histidyl amino acid residues (both having $e^2qQ/h = 1.47$ MHz, $\eta = 0.91$) are equatorially coordinated to Cu^{2+}, although the data does not preclude another axially or equatorially coordinated nitrogenous ligand [188]. The A_{iso} values of these two nitrogens are not identical, being 1.5 and 2.0 MHz [188]. Using both two- and three-pulse ESEEM methods, water is shown to be accessible to the copper site. On the basis of deuterium-exchange experiments, its direct coordination to copper is suggested. When N_3^- binds to the metal, it displaces a H_2O at the equatorial position [188]. This type of ligation proposed for the type 2 copper in the Hg(II)-derivative of laccase bears a resemblance, both in the number of imidazoles coordinated and in the water ligation, to the type 2 site in ascorbate oxidase as determined by X-ray crystallographic analysis [185].

Goldfarb et al. [189] have performed orientation selective ESEEM on native laccase and ascorbate oxidase as well as in the Hg(II)-derivative of laccase. Their

findings agree with those in Ref. [188]. There are two histidines coupled to the type 2 sites in laccase [189], although the coupling parameters found by this group (e.g. two equivalent nitrogens with $A_{iso} = 1.5$ MHz, $e^2qQ/h = 1.55$ MHz, $\eta = 0.91$) are somehow different than those reported in Ref. [188]. In Ref. [189] the two nitrogen hyperfine couplings were found to be inequivalent for the type 1 sites in laccase (N1, $A_{iso} = 1.7$ MHz; N2, $A_{iso} = 1.53$ MHz and $e^2qQ/h = 1.45$ MHz, $\eta = 0.92$ for both nitrogens) and in ascorbate oxidase (N1, $A_{iso} = 1.27$ MHz; N2, $A_{iso} = 0.76$ MHz and $e^2qQ/h = 1.45$ MHz, $\eta = 0.95$ for both nitrogens). The signals at the type 2 site of ascorbate oxidase remained unresolved probably because of severe deviation from the cancellation condition [189]. Based on the X-ray structure of ascorbate oxidase [185], the observed differences between the quadrupole parameters of type1 and type 2 sites was attributed to the alkyl group of the side-chain being adjacent to the bound imidazole in type 1 and to the remote nitrogen in type 2 [189].

6.1.3.3. Isopenicillin N synthase. Isopenicillin N synthase (IPNS) is a non-heme iron(II)-containing enzyme which catalyzes the oxidative ring closure reactions of δ-(L-α-aminoadipoyl)L-cysteinyl-D-valine (ACV) to form isopenicillin N, the precursor of all other penicillins, with concomitant four-electron reduction of a single equivalent of dioxygen to form two equivalents of H_2O. The Cu(II)-substituted IPNS [Cu(II)IPNS] was used for spectroscopic studies of the active site structure of the enzyme by ESEEM spectroscopy [173].

Based on the observation of combination lines in three-pulse ESEEM for Cu(II)IPNS, Fig. 16, it was concluded that two — nearly magnetically equivalent — His imidazoles are equatorially coordinated ($A_{iso} = 1.65$ MHz for the remote ^{14}N of each imidazole). ACV binding to Cu(II)IPNS causes a significant perturbation of the magnetic coupling of the coordinated His residues with the Cu(II) center so that A_{iso} of the remote nitrogen becomes 1.30 MHz for one His and 2.16 MHz for the other. The ESEEM studies also suggested that water, as a ligand of the Cu(II) in IPNS, is displaced upon ACV binding [173].

6.1.3.4. Dopamine β-hydroxylase. Dopamine β-hydroxylase (DβH) is a tetrameric, copper-containing glycoprotein monoxygenase. The fully active enzyme contains approximately eight copper atoms per tetramer. ESEEM study of Cu(II) in DβH [190] revealed frequency components at 0.7, 1.4 and 4.0 MHz, characteristic Cu(II)-imidazole complexes where imidazole is protonated and equatorially coordinated. Spectral simulation showed that there are three, or more likely four, imidazole ligands bound to Cu(II) [190]. Addition of a deuterated substrate analogues to the enzyme did not produce any observable ^2H modulation in the spin-echo envelopes, thus indicating that the distance between substrate deuterons and Cu(II) is greater than 5 Å [190].

6.1.3.5. Phenylalanine hydroxylase. Phenylalanine hydroxylase (PAH) catalyzes the conversion of L-phenylalanine to L-tyrosine utilizing molecular oxygen and a tetrahydropterin cofactor. ESEEM studies for PAH from *Chromobacterium vio-*

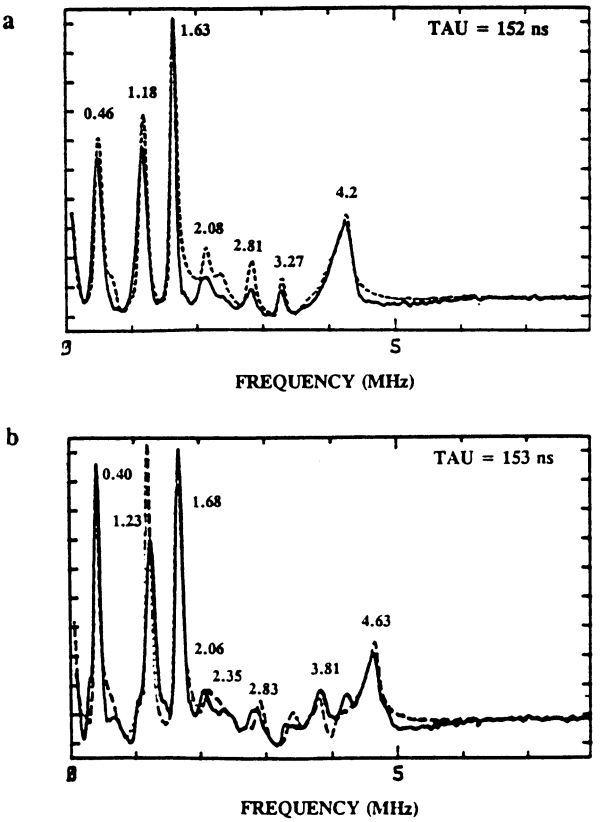

Fig. 16. Three-pulse ESEEM spectra (solid lines) of Cu^{2+} isopenicllin synthase (IPNS) in the absence (pH 6.0) (a) and in the presence (pH 7.1) (b) of substrate ACV. Measurement conditions: (a) $\nu_{mw} = 8.9262$ GHz, $H = 3088$G, $T = 4.2$ K. (b) $\nu_{mw} = 8.8515$ GHz, $H = 3059$ G, $T = 4.2$ K. The dashed lines are simulated spectra for two interacting imidazole ^{14}N nuclei. The peaks at 2.06, 2.81, 3.27 MHz in (a) and 2.06, 2.35, 3.81 MHz in (b) are combination lines. Reprinted form Ref. [173] after permission. Copyright 1991 American Chemical Society.

laceum, which contains one Cu^{2+} per monomer, have allowed the assignment of imidazole as a ligand to Cu^{2+} [165]. The observed nuclear quadrupole frequencies at 0.55, 1.0, and 1.55 MHz, arising from the remote nitrogen of equatorially bound imidazole, are similar to those observed in Cu^{2+} complexes with 2-methylimidazole. The observations of combinations of ^{14}N frequencies indicate that more than one such ligand is bound. Based on ESEEM data from a Cu^{2+}-2-methylimidazole model compound and computer simulations it was concluded that two imidazoles are bound equatorially to Cu(II) [165].

ESEEM spectroscopy was used to identify two histidine residues, His-138 and His-143, that appear to be critical for catalytic activity [191]. Both histidines, 138 and 143, were mutated to serines. The mutant enzymes H138S and H143S were both catalytically inactive, but still able to bind Cu(II). ESSEM studies on each of

the mutants showed the presence of only a single copper-coordinating histidine, rather than two histidine ligands suggested for the wild-type protein. This result supported a model in which Cu(II) is equatorially ligated to only two histidines in the Cu(II)-inhibited protein and suggested histidines 138 and 143 as these ligands [191].

6.1.3.6. Galactose oxidase. The single Cu(II) site of the 'non-blue' copper protein, galactose oxidase, has been studied by two-pulse and three-pulse ESEEM [192]. The Fourier transform contains frequency components at 0.55, 1.0, 1.53 and 4.1 MHz at a magnetic field $H_0 = 3170$ G. Differences in the frequencies ν_-, and ν_0 show that there is a perturbation of the quadropolar field not present in stellacyanin or in various imidazole-containing model compounds and may indicate weak hydrogen bonding of the imidazole to the protein. Computer simulations of the superhyperfine spectrum for a ^{14}N nucleus coupled to electron spin indicate that these frequencies are due to ^{14}N in a quadrupolar field characterized by frequencies ν_+, ν_-, and $\nu_0 = 1.54$, 1.0 and 0.54 MHz and coupled by $A_{iso} = 1.8$ MHz [192]. The results of two-pulse electron spin-echo envelope measurements of galactose oxidase are consistent with the view that galactose oxidase contains a ligand other than imidazole which is easily displaced by F^-, CN^-, or imidazole [192].

6.1.3.7. Stellacyanin. The c.w. EPR spectrum of stellacyanin compared to the other type 1 copper proteins such as azurin and rusticyanin, differs with respect to line width and shape, which is indicative of a disparity in the protein's magnetic properties (i.e. ligand field parameters). This difference was attributed to stellacyanin possessing a variant of the otherwise conserved copper binding motif [193]. Early time-domain ESEEM studies have confirmed that histidine is bound to copper [194,195]. Recently, stellacyanin was reinvestigated by multifrequency ESSEM [196]. Based on a novel approach for analyzing weak $^{14}N(I = 1)$ slightly dissimilar hyperfine interactions, the ESEEM data have been interpreted by a two imidazole model [196]. That is, the ESEEM spectra can be fully described in terms of hyperfine interactions arising from two $HisN_\delta$ (i.e. the remote, non-coordinated nitrogen) of the imidazole side chains that serve as copper ligands in the type 1 protein motif. The imidazole ring orientations are perpendicular to one another (minimally 60°). The spin Hamiltonian parameters assigned to these two nitrogen atoms are: $e^2qQ = 1.45$ MHz, $\eta = 0.9$, $A = 2.0$ MHz and; $e^2qQ = 1.50$ MHz, $\eta = 0.9$, $A = 1.5$ MHz. Analysis of the double-quantum transition lineshape indicates that the nuclear hyperfine interaction tensor is very nearly isotropic. In spite of evidence for its existence, no features of these ESSEM spectra can be attributed to an amino nitrogen of a glutamine side chain [196] nor is there any need to invoke the contribution of a third nitrogen coupling in order to explain lineshape variation over the g-value or frequency range examined.

6.1.3.8. Azurin. Azurin is a blue single-copper protein containing a type 1 copper site which has unique spectroscopic properties: an intense blue color due to a S(Cys) → Cu(II) charge transfer absorption near 600 nm and a relatively small

Cu(II) hyperfine interaction ($A_{\parallel} \leq 90 \times 10^{-4}$ cm^{-1}) [169]. The available three-dimensional structures of several copper proteins with a type 1 site reveal three strong ligands, a cysteine thiolate and two imidazole residues of histidine, in a trigonal arrangement with rather short bonds and a fourth, weaker axial ligand (usually a thioether of methionine) [197], see Fig. 17. Azurin is exceptional in the sense that its crystal structure shows an additional weak axial copper interaction with a peptide carbonyl from glycine-45 at a distance around 3 Å [198].

HYSCORE spectroscopy was applied to study the copper ligands in azurins from *Pseudomonas aeruginosa*, Az(pae), and *Alcaligenes species NCIIB 11015*, Az(asp), in frozen solutions [199]. Measurements were performed at ~ 9 GHz which is usually within the cancellation condition [87] for the remote nitrogen of imidazole ligands. At all pH values investigated, the HYSCORE spectra, Fig. 17(A), of Az(pae) showed cross-peaks due to the remote nitrogens of the imidazole ligands and additional well-resolved cross-peaks from a weakly coupled amide ^{14}N [199]. This confirms earlier detection and assignment of three-pulse ESEEM spectra of this ^{14}N recorded for the H117G mutant [200]. The HYSCORE spectra of Az(asp) were similar to those of Az(pae) showing that a third weakly coupled nitrogen is present in this species as well. Comparison with the corresponding spectrum of ascorbate oxidase suggested that this nitrogen is the amide nitrogen of His-46, magnetically coupled to the copper via the carbonyl group of Gly-45. This further implied that also in azurin from Az(asp), the copper in the type 1 site has five ligands rather than four [199]. A W-band, e.g. 94GHz, Fig. 17C, ESEEM study of a single crystal of azurin has been reported also [151]. At the W-band, the coordinated instead of the remote nitrogens of copper proteins can be investigated by ESEEM. The isotropic hyperfine coupling of the copper-bound nitrogen of His-117 was 1.4 times larger than that of His-46. The anisotropic hyperfine tensors showed that the wave function of the unpaired electron on the coordinated nitrogens mainly concerns the σ bonds with copper [151].

6.1.3.9. Rusticyanin. Rusticyanin possesses the characteristic type 1 copper binding motif CysHis$_2$Met [169] where the ligands are Cys-138, His-143 and Met-148, while the fourth ligand was conclusively identified as His-85, Fig. 18 [201].

ESEEM spectra were recorded across the EPR spectrum for the rusticyanin and its engineered variant His-85Ala, which lacks one of the two imidazole ligands to copper [202]. The Zeeman and g-value dependence of the spectral peaks were systematically mapped and accurately predicted that low intensity lines in the wild type (w.t.) spectrum were combination lines, as verified in the His-85Ala spectra. Analysis reveals that the w.t. ESEEM spectra are attributable to a pair of HisN$_{\delta}$ only, and the NQI parameters, e^2qQ/h and η, are 1.37 MHz and 0.90 for both HisN$_{\delta}$ in the w.t. protein. The nuclear hyperfine interaction is estimated as 1.8 MHz, and includes a dipolar interaction of 0.5 MHz. The principal difference between the two imidazole nitrogen couplings is manifest in the dispersion of the combination lines, which suggests non-equivalent orientations of the respective

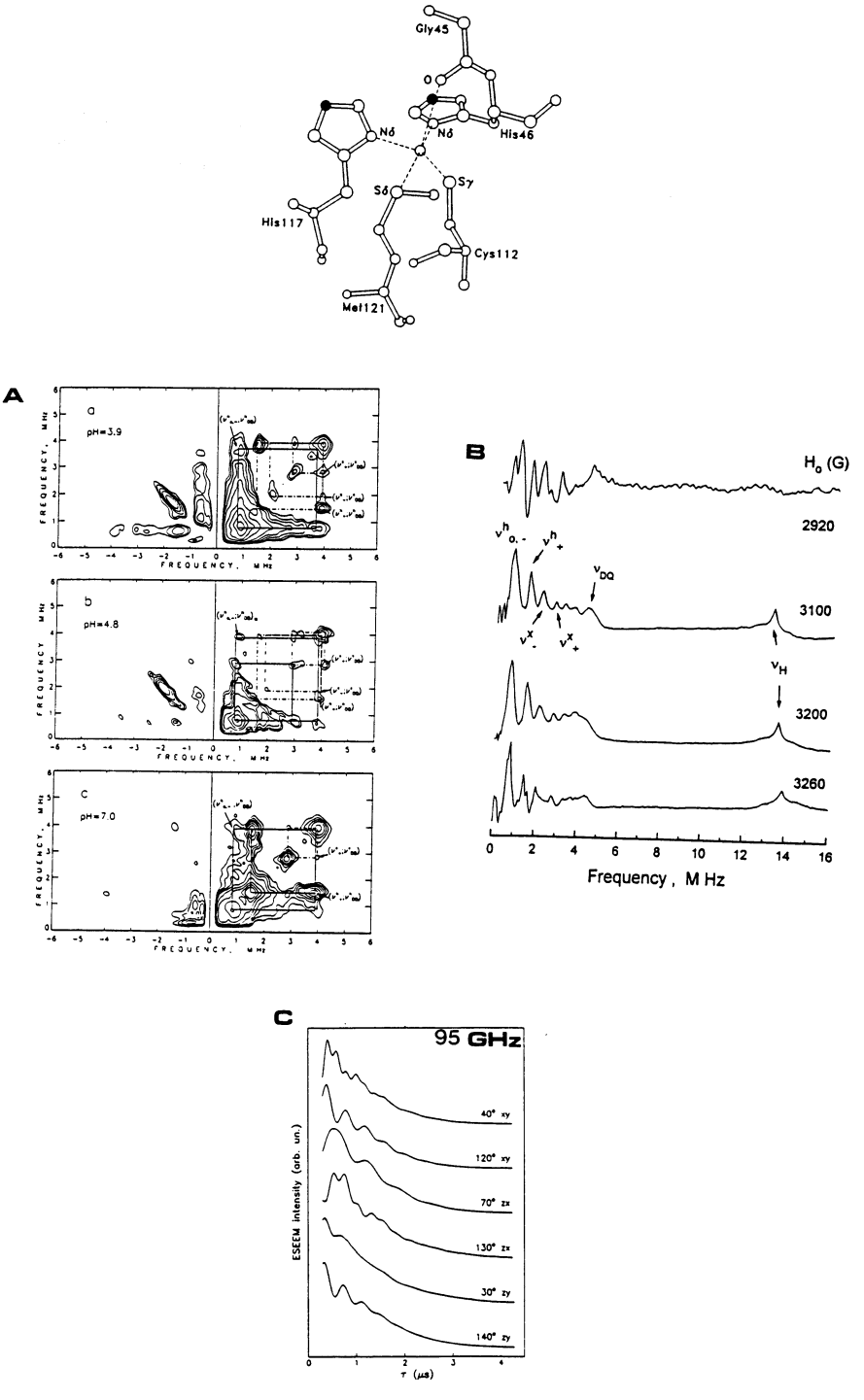
Gly45
O
Nδ
Nδ
His46
Sδ
Sγ
His117
Cys112
Met121
A
a
pH=3.9
b
pH=4.8
c
pH=7.0
FREQUENCY, MHz
B
H_o (G)
2920
3100
3200
3260
$\nu^h_{\alpha,-}$
ν^h_+
ν_{DQ}
ν^x_-
ν^x_+
ν_H
0 2 4 6 8 10 12 14 16
Frequency , M Hz
C
95 GHz
40° xy
120° xy
70° zx
130° zx
30° zy
140° zy
ESEEM intensity (arb. un.)
τ (μs)

Fig. 17.

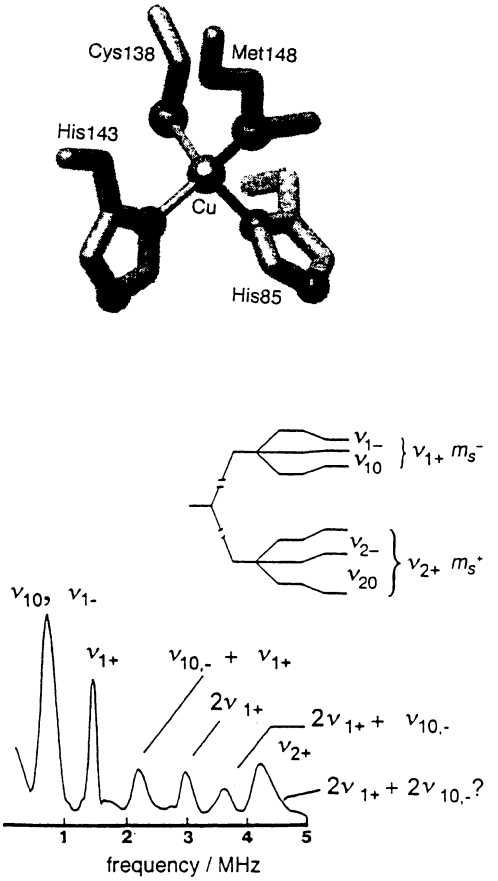

Fig. 18. (Top) Structure of the copper coordination sphere of rusticyanin. (Bottom) A representative three-pulse ESEEM spectrum of wild type rusticyanin, recorded at $g = 2.25$ and 9.0 GHz. The peaks in the 2–5 MHz range are combinations of the basic harmonics, presented by the strong peak below 2 MHz. The energy level diagram and labeling used to assign the peaks are illustrated (inset). Reprinted from Ref. [202] with permission.

Fig. 17. (A) Contour plots of HYSCORE spectra of the structure of Azurin from *Pseudomonas aeruginosa*, recorded at $g = 2.06$. (a) pH 3.9, $\tau = 300$ ns, $H = 3115$ G. (b) pH 4.8, $\tau = 300$ ns, $H = 3210$ G. (c) pH 7.0, $\tau = 350$ ns, $H = 3216$ G. The main cross peaks are due to coupling of the remote ^{14}N of His-117, with secondary contribution from His-46. Contribution from a backbone nitrogen, either from Cys-112 [199] or from Cys-45 [200], are also resolved. (B) Orientation selective three-pulse ESEEM of Azurin from *Alcaligens* species, at pH 4.8, $\tau = 180$ ns. For $H = 2920$ G, τ is 170 ns. Reprinted from Ref. [199] with permission. Copyright 1996 American Chemical Society. (C) W-band 95 GHz two-pulse ESEEM for a single crystal of Azurin from *Pseudomonas aeruginosa*. Data for six orientations of the magnetic field with respect to the g-tensor principal axes system (x, y, z) are shown. The modulations originate from the coordinated ^{14}N from His-46 and His-117. Reprinted from Ref. [151] with permission. Copyright 1997 American Chemical Society. The structure of Azurin from *Pseudomonas aeruginosa* shown at the top of the figure, is reprinted from Ref. [200] with permission.

superhyperfine tensors (or tilt of the imidazole ring) [202]. Finally, peak shifts among ESEEM spectra of His85Ala-X ($X = H_2O$, Cl^-, Br^-) demonstrated that the imidazole ligand powder superhyperfine spectrum is sensitive to chemical effects in the metal's ligand sphere [202].

6.1.3.10. Cytochrome c oxidase. Cytochrome *c* oxidase is the terminal protein in the mitochondrial respiratory chain and catalyzes the reaction in which molecular oxygen is reduced to water in a four-electron reduction [203,204]. There are four redox-active metal centers in cytochrome *c* oxidase, two copper centers, Cu_A and Cu_B, and two iron atoms bound as heme chromophores that are designated cytochromes α and α_3, Fig. 19. Of the two Cu sites, the Cu_B is EPR silent, while the Cu_A site is EPR detectable, and is bound to two histidyl ligands detected by ENDOR spectroscopy [205]. The protein spans the inner mitochondrial membrane and actively pumps protons out of the matrix by using the redox free energy made available during the catalytic cycle.

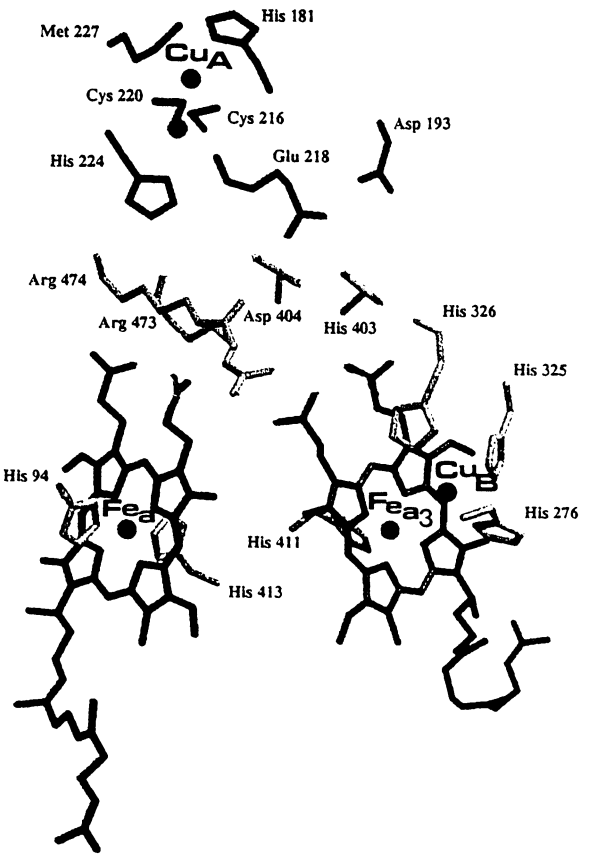

Fig. 19. Three dimensional structure of cytochrome *c* oxidase. The copper, Cu_A and Cu_B, and the heme centers α and α_3 are marked. Adapted from Ref. [351] with permission.

Proton currents in the enzyme are crucial to its catalytic cycle [203,204]. These protons are expected to be exchangeable. ENDOR and ESEEM spectroscopies were used to study whether protons in the immediate protein environment around Cu_A in cytochrome *c* oxidase are susceptible to solvent exchange [206]. The enzyme was incubated in buffered D_2O under resting or turnover conditions for 90 min and then frozen to quench the hydrogen/deuterium-exchange process. The ESEEM spectra provided a clear indication of the introduction of deuterium into the Cu_A environment following incubation in buffered D_2O. The extent of deuterium incorporation was not affected by enzyme turnover. The ESEEM data indicated that water was in reasonably close proximity to the Cu_A site, but not in the coordination sphere of the metal(s) [206]. The minimum distance from the Cu_A site to the protein/water interface of the cytochrome *c* oxidase is approximately 5.4 Å.

6.1.3.11. Hemocyanin. In hemocyanin (Hc), reversible oxygen binding occurs at a binuclear copper site. A complex formulated as Cu(II)–O_2^{2-} Cu(II) is present in oxy-Hc, reflecting one-electron transfer from each cuprous copper of deoxy-Hc to the bound dioxygen [207]. According to the three-dimensional structure of deoxy-Hc from *Panulirus interruptus* (*Arthropoda*) determined to 3.2 Å resolution by X-ray crystallographic analysis of crystals formed at pH 4 [208], each copper atom is coordinated to two nitrogen atoms from approximately coplanar histidyl imidazoles and, perpendicular to these, to a third histidine imidazole nitrogen at a distance of 2.7 Å. The Cu–Cu distance is 3.6 ± 0.4 Å. The geometry of the active site is approximately trigonal and no evidence was found for a fourth ligand to copper.

The structure of the Cu(II) site in a derivative of hemocyanin known as green half-met (GHM) has been analysed using ESEEM spectroscopy [209]. The rationale for this preparation is its use as a paramagnetic probe of the active site structure of the protein. The ESEEM spectra of these green half-methemocyanins indicated that three imidazole ligands are coordinated to Cu(II), see Fig. 20. Based on this information, a tetragonal N_3O ligand structure (O is an oxygen of nitrite) was proposed. The g and A_{cu} (copper nuclear hyperfine coupling) values for the derivatives, and the finding of three similar nuclear hyperfine coupling constants for the N_δ sites of imidazole ligands, when considered with the orientation-specific information obtained using angle-selection methods for simulation of ESEEM spectra, suggest a distorted tetragonal Cu(II) structure in which three imidazoles and a nitrite ligand are bound near the equatorial plane [209]. Another approach used to obtain a paramagnetic center involves the preparation of a mononuclear Cu(II) derivative of *Carcinus maenas* hemocyanin (Cu(II)–Hc) and a nitrite complex of the derivative (Cu(II)–Hc–NO_2^-) [210]. Several techniques have been used in their characterization, including X-ray absorption, c.w. EPR, and ESEEM spectroscopies [210]. EXAFS results for Cu(II)–Hc indicate the presence of three ligands at 1.99 Å and a fourth one at 2.26 Å from the copper. The same coordination number and very similar bond lengths were obtained for Cu(II)–Hc–NO_2^-. On the basis of simulations of three-pulse ESEEM spectra, three equivalent imidazole nitrogens coupled to Cu(II) were identified in Cu(II)–Hc. Upon the binding of nitrite, a

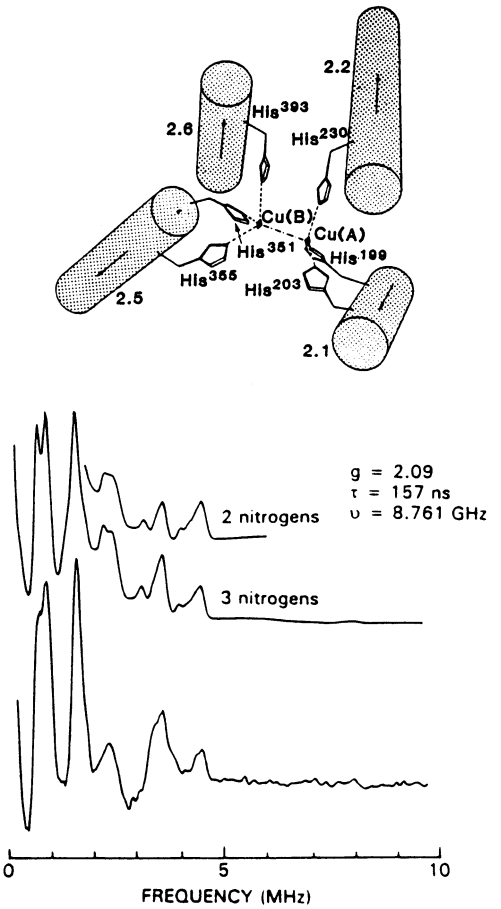

Fig. 20. (Top) Structure of one binuclear binding site in hemocyanin from *Panulirus interruptus*. Reprinted from Ref. [208] with permission. (Bottom) Three pulse-ESEEM and their simulations for green half-met hemocyanin of *O. vulgaris*. The bottom spectrum was recorded at $H = 3000$ G. The simulations have been performed for either two ^{14}N, one weakly ($A_{iso} = 1.1$ MHz) and one strongly ($A_{iso} = 1.73$ MHz) coupled, or three ^{14}N, two weakly ($A_{iso} = 1.1$ MHz) and one strongly ($A_{iso} = 1.73$ MHz) coupled. Reprinted from Ref. [209] with permission. Copyright 1995 American Chemical Society.

decrease in the hyperfine interaction for two of the three imidazole nitrogens was observed by ESEEM. Further, the results of a two-pulse ESEEM experiment are consistent with the assignment of the protons of a water ligand to Cu(II), which is displaced when nitrite is added [210]. An analysis of X-ray absorption K-edge spectra suggests a coordination geometry intermediate between square-planar and tetrahedral for the metal centers in Cu(II)–Hc and Cu(II)–Hc–NO_2^-, in agreement with the g and A_{cu} values determined by c.w. EPR. On the basis of these results, an equivalent structure is suggested for Cu(II)–Hc–NO_2^- and the Cu(II) site in green half-methemocyanin, a partially oxidized binuclear derivative formed in the reaction of the native protein with nitrite [210].

6.2. Iron

6.2.1. Model heme-iron

6.2.1.1. General characteristics. Heme enzymes are involved in the metabolism of biomolecules, drugs, and xenibiotics (oxygenases, perioxidases), in imicrobial activities (peorxidases) and in respiration (cytochrome oxidase); binding of oxygen to the heme iron is central to the above mechanisms but also to the oxygen transport role of globins [211,212]. Among other factors, the binding of ligands to the sixth coordination position of the heme iron and the polarity of the distal heme pocket, i.e. the protein moiety surrounding the bound dioxygen, has been shown to be an important factor in determining the functional characteristics of proteins [211] and model compounds [212]. Axial histidine coordination is a structural motif conserved in the active site of most known oxygen-carrying hemoproteins [211]; in addition, a distal histidine close enough to the binding site is hydrogen bonded to the bound O_2. The structural unit [His$\cdots O_2$–Fe–His] plays a key role in the function of oxyglobins [211].

6.2.1.2. Low-spin Fe^{3+} ($S = 1/2$) (TPP). A isotropic hyperfine coupling of, e.g. $A_{iso} = 4–6$ MHz, is typically observed for the porphyrin ^{14}N in Fe^{3+} ($S = 1/2$)-(heme) in models and proteins [213,214]. ^{14}N nuclei directly coordinated at the axial position in Fe^{3+} ($S = 1/2$)-(TPP)-L compounds, are characterized by slightly smaller $A_{iso} = 4–5$ MHz with modest hyperfine anisotropy, and give rise to ESEEM spectra characterized by two double quantum lines [213,214]. Coupling with the more remote nitrogen nucleus of axially coordinated imidazole is weak, and is not detectable by ESEEM in heme complexes, Fig. 21 [214].

6.2.1.3. NO($S = 1/2$)–Fe^{2+} ($S = 0$) (TPP). In NO–Fe^{2+}(TPP) complexes with $S_{total} = 1/2$, the ^{14}N of the NO group has strong coupling ($A_{iso} \sim 50–60$ MHz) which is resolved in the c.w. EPR [215] and ENDOR [216], but not in X-band ESEEM. The pyrrole ^{14}N nuclei with $A_{iso} \sim 2$ MHz, see Fig. 21, were found to have the dominant contribution detected by ESEEM in six-coordinate NO–Fe^{2+}(TPP)-L,(L = pyridine or imidazole) complexes [215]; in five-coordinate NO–Fe^{2+}(TPP) complex, the pyrrole nitrogens bear a small fraction of the spin density ($A_{iso} < 0.5$ MHz) and do not contribute to the ESEEM spectrum [215].

In NO–Fe^{2+}(TPP)-[^{14}N]imidazole and NO-myoglobin-[^{14}N]imidazole, the imidazole nitrogens have couplings which are either too weak, e.g. $A_{iso} < 1$ MHz for the remote ^{14}N(H), or too strong, e.g. $A_{iso} \sim 18$ MHz for the directly coordinated ^{14}N, and do not contribute to ESEEM [215]. Based on this findings, modulations corresponding to $A_{iso} \sim 2$ MHz that were initially considered to originate from the remote nitrogen of imidazole in NO–Fe^{2+}(TPP)-[^{14}N]imidazole[213], were reassigned to the remote nitrogen of imidazole coordinated to high-spin Fe^{3+}-TPP-[^{14}N]imidazole contamination [154,214].

The pyrrole ^{14}N-ESEEM was used to distinguish between six- and five-coordination in NO-[haemoglobin], i.e. with and without axial nitrogenous base, [215]. In

this context, in NO-hemoglobin, pyrrole ^{14}N-modulations resolved in the *R*-state were interpreted as indicating six-coordination, while their absence in the T-state was interpreted as indicating five-coordination. Based on these data it was suggested that the proximal imidazole bond to heme iron is disrupted in the T-state [215].

Recently, the proton sum combination-peaks in the ESEEM spectra of low-spin ferriheme complexes provided single-crystal-like information concerning the orientation of the g-tensor in frozen glassy media [31,61]. In Fe-TPP(pyrazole)$_2$ [31], as well as in Fe-OEP(imidazole)$_2$ and Fe-OEP(4-dimethylamino)pyridine)$_2$ (OEP = octaethylporpyrinate) [61], the *z* magnetic axis direction was identified as perpendicular to the mean plane of porphyrinate. Based on detailed investigation of both the intensities and the frequency-shifts of the proton sum-combination, it was found that g_{zz} is the largest *g*-value. Moreover it was possible to determine the orientations of g_{xx} and g_{yy} as a function of the orientation of the axial ligands with respect to the porphyrinate nitrogens [31,61].

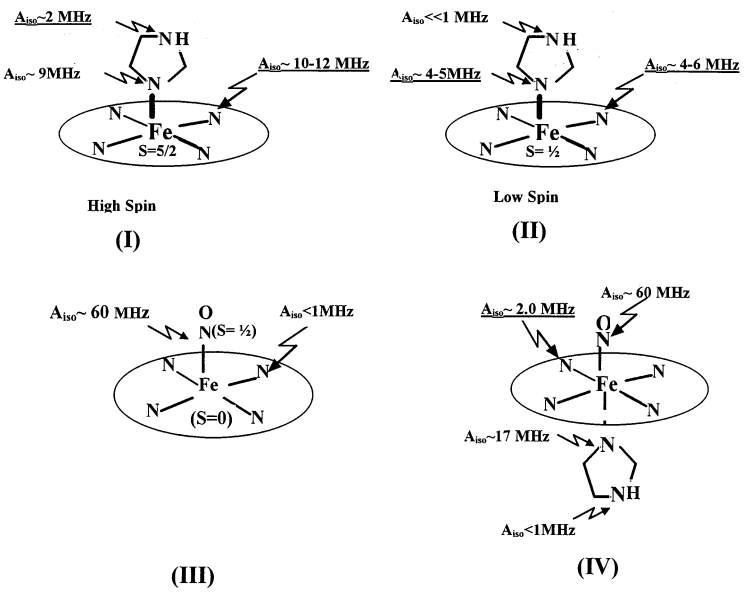

Fig. 21. Hyperfine coupling parameters, A_{iso}, for ^{14}N nuclei observed for various heme-iron compounds. (I) In the high-spin iron, $S = 5/2$, compound with axial imidazole, the porphyrin nitrogens and the coordinated nitrogen from imidazole have comparably strong couplings, while the remote nitrogen of imidazole has a weaker coupling. All these couplings have been measured by ENDOR [154]. (II) In low-spin heme compounds, the porphyrin nitrogens and the coordinated nitrogen from imidazole have comparable couplings in the range 4–6 MHz, amenable for ESEEM investigation [213,214]. The coupling of remote imidazole nitrogen is very weak. (III) In heme–nitrosyl compounds the spin density is localized mainly at the N atom of NO, measured by ENDOR [216]. The porphyrin nitrogens have very weak couplings, detectable however by ESEEM [215]. (IV) The presence of an imidazole as sixth ligand increases the hyperfine couplings for the pyrrole nitrogens, rendering them suitable for ESEEM spectroscopy. The axially coordinated nitrogen is strongly coupled while the remote nitrogen has very weak couplings.

Earlier ESEEM data on model heme–iron compounds showed that the deviation between the g_z and Q_{zz} axes is small, no more than 10° [214]. For the axial nitrogens in heme–iron model systems, the e^2qQ/h values, determined by ESEEM [214], are found to be smaller than for the free ligands, determined by NQR [159,160]. This is due to the reduction of the population of the lone pair of the nitrogen which acts as donor to the empty d_{z^2} iron orbital. In low-spin heme-iron models the maximum g-component, labeled g_z, lies near to the heme normal while g_x and g_y lie in the heme plane and their exact orientation depends on the axial ligand [214]. The lone-pair donor orbital of the axial nitrogen ligands are considered to be directed close to the heme normal in order to form a σ bond to the iron [214]. Accordingly, the heme normal will correspond to the direction of the principal axis of the NQI tensor, usually Q_{zz}, occurring along the nitrogen lone-pair orbital. ESEEM data for myoglobins revealed the Q_{zz} axis of the axial nitrogen is almost collinear with the g_z axis, showing that the Q_{zz} axis is determined by the direction of the lone-pair orbital of the axial nitrogen [214]. Surprisingly the Q_{zz} axis of the pyrrole nitrogens was found to be at $\sim 45°$ with respect to the g_z axis. This orientation may be due to an 'anomalous' nuclear quadrupole axes system for the porphine pyrrole nitrogens, where Q_{zz} is no longer coincident with the lone pair nitrogen donor orbitals, analogous to that observed for Cu^{2+}(TPP) [217].

6.2.2. Heme–iron proteins

6.2.2.1. Myoglobin. In myoglobin (Mb), the low-spin $F^{3+}(S = 1/2)$ orbital system has the electron configuration ($d_{xy}{}^2$, $d_{xz}{}^2$, $d_{yz}{}^1$) with the d_{xy} orbital being coplanar with the heme plane [156]. The iron gives one filled and one half-filled d-π orbital, for π bonding interaction with the axial imidazole (with the d_{xz}, d_{yz} orbitals) or the pyrrole nitrogens (with the d_{xy}, d_{yz} orbitals). Thus the π-bonding interaction could involve either ligand-to-metal ($L \rightarrow M$) or metal-to-ligand ($M \rightarrow L$) π donation. The coordinated imino nitrogen of imidazole, considered to be sp^2 hybridized has a p-π lobe oriented parallel to the partially filled d orbital. The proximal, axially coordinated imidazole ^{14}N is characterized by A_{iso} in the range 1.7–3.6 MHz, while A_{iso} in the range 4.1–5.1 MHz was measured for the pyrrole ^{14}N nuclei [156]. In myoglobin, the A_z value for the coupling of the axial ^{14}N was found to be the weakest $A_x = A_y > A_z$ [156]. The same holds for model low-spin iron heme complexes [154,156] and this may be interpreted as being due to negative A_{iso}, which in turn means that the spin density is transferred through a spin-polarization mechanism [156]. Direct spin transfer through the metal–nitrogen σ bond is not the dominant spin-transfer mechanism, because the p-π orbital of the proximal imidazole nitrogen is not optimally oriented for efficient overlap with the half filled d-π iron orbital [156,218].

A characteristic trend was found for the A_{iso} values of the proximal imidazole nitrogen in Mb derivatives: in MbCN and MbRS (where RS = β-mercaptoethanol) the hyperfine coupling ($A_{iso} = 2.2$ MHz for both cases) is found to be smaller than in either MbOH ($A_{iso} = 5.1$ MHz) or MbN_3 ($A_{iso} = 4.4$ MHz) [156]. This reduction of the coupling in MbCN and MbRS is not due to the *trans* effect, neither is it due

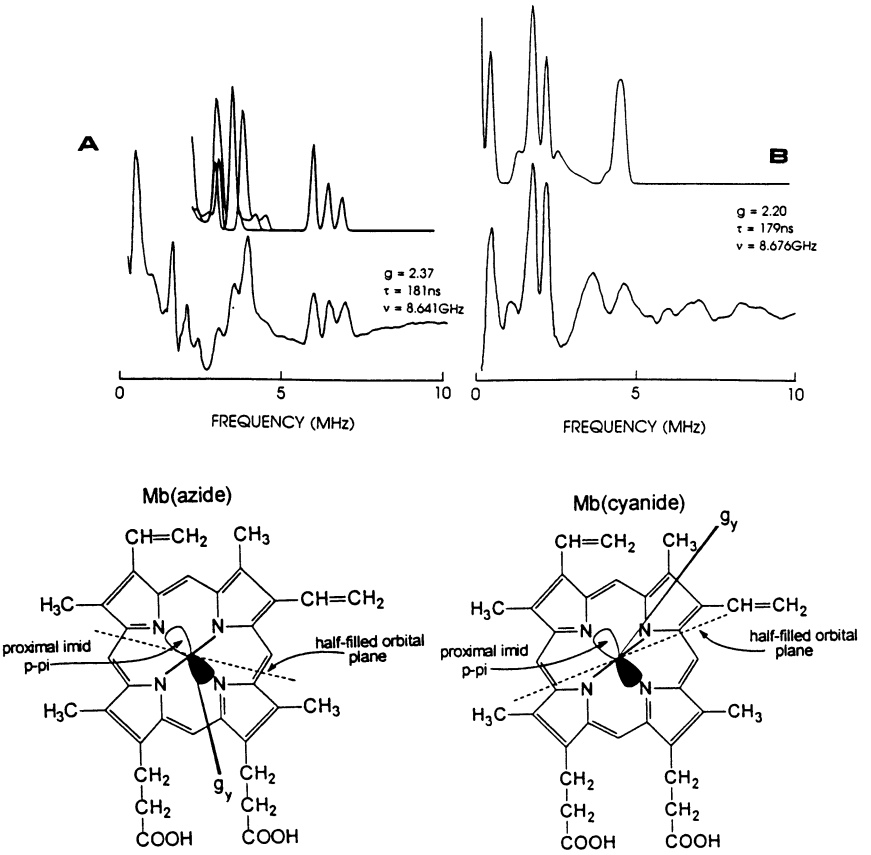

Fig. 22. Three-pulse ESEEM and simulations, of myoglobin (Mb). (A) (bottom) Spectrum of Mb(β-mercaptoethanol). (Top) Simulations for [^{14}N]pyrrole sites. Three sets of ^{14}N couplings ($A_{iso} = 5.1$, 4.6, 4.1 MHz, respectively) were used to generate the simulations presented. (B) (bottom) ESEEM spectrum of ^{15}N[heme]MbCN. (Top) Simulations for the directly coordinated ^{14}N of the proximal imidazole ($A_{iso} = 2.2$ MHz). The orientation of the g-tensor axes, the projection onto the proximal imidazole plane, the nitrogen p–π orbital and the half-filled orbital plane for Mb(azide) and Mb(CN) are shown. Reprinted from Ref. [156] with permission. Copyright 1993 American Chemical Society.

to low symmetry effects in the crystal field of the iron [156]. Instead, it arises from a redistribution of the unpaired electron spin density, e.g. involving delocalization of spin density from iron into CN^- and RS^- ligands, due to covalency between the iron and CN^- or RS^- ligands, which does not occur in the case of OH^- and N_3^-.

In the azide complex, the half-filled iron orbital has been assigned to lie between an Fe–$N_{pyrrole}$ vector and a *meso*-carbon plane, and is located between the projection onto the heme plane of the p–π orbital of the axial nitrogens from both azide and imidazole, see Fig. 22, [156]. In MdCN the half-filled iron orbital plane nearly eclipses the Fe–$N_{pyrrole}$ vector, Fig. 22 [156]. Based on the e^2qQ/h values, estimated from ESEEM data for MdCN ($e^2qQ/h = 2.5$ MHz) and MbN_3 ($e^2qQ/h = 3.2$

MHz), it was suggested that the proximal imidazole acts as a π-acceptor in low-spin heme complexes in order to support strong σ donation from the nitrogen lone pair to iron.

The low-frequency ESEEM spectrum observed for the β-thiopropionyllysine (TPLys) derivative of horse cytochrome *c* at lysine 72 (TP-Lys72), is similar to the ESEEM spectrum for MbRS [213,156]. Based on this similarity, the ESEEM pattern for TP-Lys72-cytochrome *c*, was assigned to ^{14}N of imidazole axially coordinated to the heme-iron, probably in a mercaptate-ligated form of the heme-imidazole structure [219].

6.2.2.2. Cytochrome-P_{450}. Early ESEEM data on cytochrome P_{450} (cyt-P_{450}) provide direct evidence for coupling of a ^{14}N nucleus to cyt-P_{450}, with quadrupole coupling parameters characteristic of the remote nitrogen of an imidazole [213]. ESEEM investigation of the action of the bovine adrenal side-chain cleavage enzyme, P_{450scc} [220] on deuterated steroidal substrates, revealed that cholesterol and 20-azachloesterol bind in close proximity to the heme. For example, the deuteron at carbon-22 is at ~ 4 Å from the ferric atom; in contrast hydroxycholesterol appears not to bind in the vicinity of the iron [220]. Recently, orientation-selective ESEEM experiments on substrate-free cytochrome $P_{450cam}(S = 1/2)$ with ^{17}O-enriched water were reported [130] Fig. 23(A,B), in an attempt to resolve whether the distal axial ligand of the iron is H_2O or OH^-. The experimentally determined ^{17}O-nuclear quadrupole coupling $e^2qQ/h = 6.6$ MHz and the asymmetry parameter $\eta = 0.95$ are similar to those found in ^{17}O-water and based on this it was concluded that the distal axial ligand of the low-spin iron is a H_2O molecule. Based on the orientation of the quadrupole tensor, a structural model was suggested, Fig. 23(D,E).

The ^{17}O-hyperfine coupling was found to be weak, with two possible sets of isotropic and anisotropic couplings determined, e.g. either (2.6, 0.3 MHz) or (0.4, 1.8 MHz), respectively, both of them consistent with the unpaired electron being predominantly on the d_{xz} orbital of the iron. Using the constraints on the orientation of the water ligand as determined from the ^{17}O ESEEM [130], simulation of proton-sum combination harmonics in four-pulse ESEEM, Fig. 23(C), and pulsed ENDOR data, allowed a determination of the coupling parameters for the water protons e.g. $A_{iso}(^1H) = 1.5–2.0$ MHz [221]. The orientation of the H–H axis with respect to the g_x orientation was determined to be 40–50° [221], in agreement with the ^{17}O ESEEM data where it was found to be distributed in the range $50 \pm 10°$ [130].

Pertinent to this subject is a recent work on a model analogue of the P_{450cam} [222] which although structurally similar to the resting state of P_{450cam}, e.g. a sulfur and a water molecule as axial ligands, it is found to be in the high spin ($S = 5/2$) state [222]. ESEEM and ENDOR data for this high-spin model system showed that the nuclei of the axial water ligand have couplings ($A(^1H) = 6.8$ MHz, $A(^{17}O = 19.9$ MHz) much stronger than those of P_{450cam} [130,221]. The difference in the spin-states between the model and P_{450cam}, despite the apparent structural similarity, shows that the water ligand is not the only factor determining the electronic properties of P_{450cam} [222].

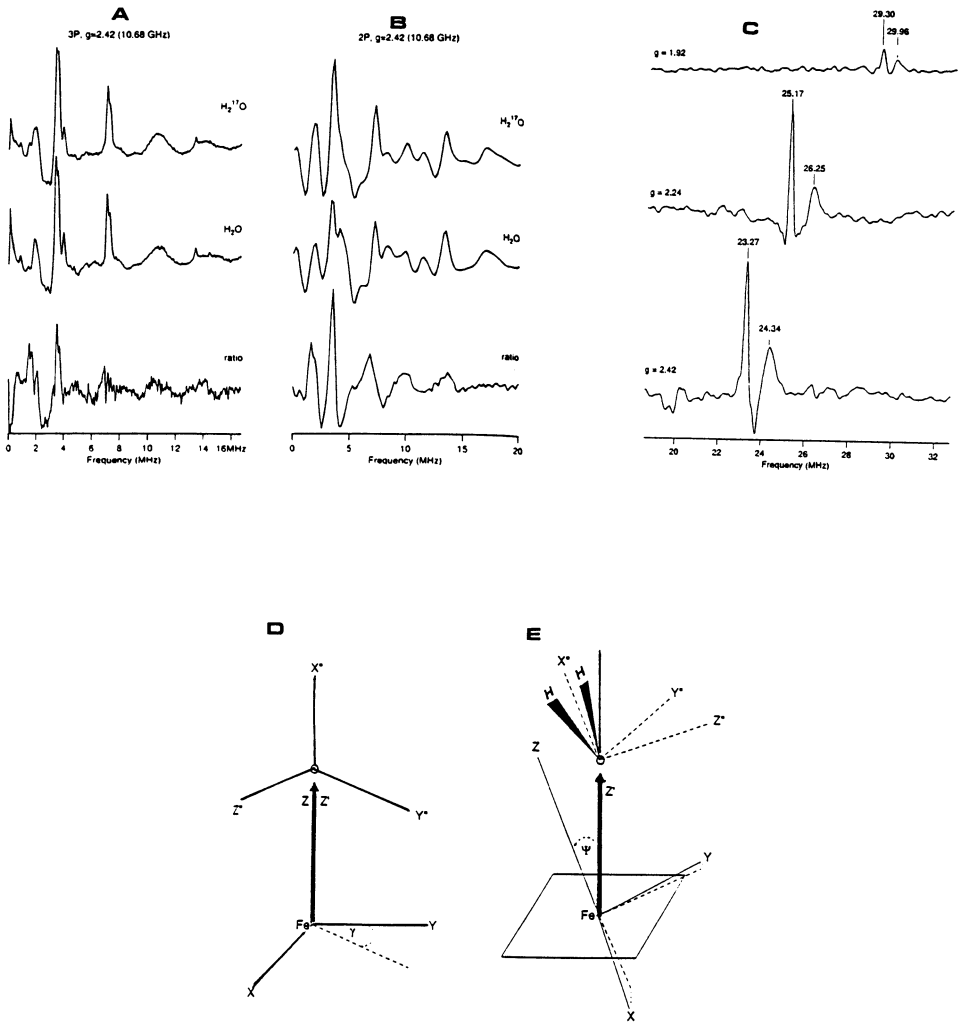

Fig. 23. Three-pulse (A), and two-pulse ESEEM (B) of cytochrome $P_{450}(H_2^{17}O)$ and $P_{450}(H_2O)$; their ratio contains features mainly due to $^{17}O(I = 5/2)$. Experimental conditions $\nu_{mw} = 10.68$ GHz, $g = 2.42$, the three-pulse spectrum was recorded with $\tau = 210$ ns. (C) Four-pulse cosine-FT-ESEEM spectra of cytochromes $P_{450}(H_2O)$, recorded across the ERP spectrum. The τ values were 240, 280 and 300 ns for the spectra at $g = 2.42$, 2.24, 1.92 respectively. The proton-sum combination harmonic is marked at each spectrum. (D) Representation of the principal axis system of the g-tensor (x, y, z) and the ^{17}O hyperfine (x', y', z') and quadruple tensors (x'', y'', z''). (E) Schematic picture showing the orientation of the water molecule with respect to the heme plane and the corresponding tensor axes, as determined from the ^{17}O ESEEM data. ψ is the angle between the normal to the heme plane and the principal axis, z, of the g-tensor. Figures A, B, D and E were reprinted from Ref. [130]. Copyright 1995 American Chemical Society. Figure C was reprinted from Ref. [221]. Copyright 1996 American Chemical Society.

6.2.2.3. Transferrins (high-spin iron). The transferrins are a family of iron-binding proteins that include transferrin (Tf) and lactoferrin (Lf) which are found in physiological fluids in a wide variety of vertebrates [223]. X-ray crystal structures have confirmed earlier spectroscopic findings that both proteins have two metal-binding sites that are spatially well-separated [224,225]. In the native protein, both sites have high affinity for iron in the $3+$ oxidation state and give rise to a characteristic 'rhombic' EPR signal at $g_{\text{eff}} = 4.3$ [223].

The protein provides four ligands for the metal, two tyrosines, one histidine and one aspartate, leaving two sites available for coordination of water or exogenous anions, Fig. 24; occupancy of the metal-binding sites by iron requires binding of an anion [226] which is considered physiologically to be the carbonate anion, CO_3^{2-} [223]. A variety of spectroscopic techniques have shown that the anion-binding site is in close proximity to the metal binding site [223], probably simultaneously to the metal and the protein [223]. The resolution of the crystal structures is not sufficient to definitely resolve this proposal. Due to the fast spin-lattice relaxation of the high-spin iron $Fe^{3+}(S = 5/2)$ sub-liquid helium temperatures (2–3 K) are required for the application of ESEEM to Fe^{3+}-transferrins. Early applications of ESEEM dealt with Cu^{2+}-transferrin [123,124], Cu^{2+}-lactoferrin [123], and VO^{2+}-transferrin [108] complexes, where ESEEM spectra of adequate quality could be recorded at 5 K. More recently, high quality ESEEM spectra of $Fe^{3+}(S = 5/2)$-transferrin (recorded at 2–3 K) for Tf-Fe–$^{13}CO_3$, [108] as well as for Tf-Fe-[1-^{13}C]puruvate [122]were reported, Fig. 24(spectra a–g). In the original study, [124], comparison of the time-domain ESEEM spectra for Cu^{2+}-Tf-[^{12}C]oxalate and Cu^{2+}-Tf-[^{13}C]oxalate revealed a 156 ns modulation indicating a specific interaction of the ^{13}C atom of oxalate with the bound copper. Two types of ^{14}N coupling were resolved by ESEEM of Cu^{2+}-Tf-CO_3, Cu^{2+}-Tf-[^{13}C]oxalate, VO-Tf-CO_3, and VO-Tf-[^{13}C]oxalate [123]. One, with $A_{\text{iso}} = 1.7$–1.8 MHz, $e^2qQ/h = 1.6$ MHz and $\eta = 0.9$, originating from the remote, non-coordinated, ^{14}N imidazole nitrogen of a histidine is resolved in the Cu^{2+} complex. The other, with $A_{\text{iso}} = 6.6$–7.0 MHz originating from the directly coordinated ^{14}N imidazole nitrogen is resolved in the VO^{2+} complex. For both vanadyl and copper complexes, ESEEM data for protein solved in either D_2O versus H_2O revealed the existence of at most one exchangeable proton within ~ 2.9 Å of the metal, plus multiple exchangeable protons within ~ 3.4 to 4.0 Å from the metal. The ESEEM together with previous ENDOR data [227] were interpreted as indicating that an OH group from water or a protein side-chain, is bound to copper but not to vanadyl. Comparison of time-domain ^{13}C-ESEEM for VO-Tf-[^{13}C]carbonate or VO-Tf-[^{13}C]oxalate revealed that the oxalate binds as a bidentate ligand with its two carbons being at equivalent distances from the metal, e.g. ~ 2.9 Å [123]. ESEEM data on Fe-Tf-[1-^{13}C]puruvate, indicate that both the carboxylate and the keto-oxygen of pyruvate are directly bound to the metal. The ESEEM together with previous EPR data led to an improved model, schemes h–l in Fig. 24 [122].

According to this model a carboxyl and a polar group are ligands to the iron and the carboxyl also serves as a bridge between the iron and a positive charge on the protein. The bridge to the protein may be sensitive to factors like ionic strength and pH, which influence release of iron from transferrin [122].

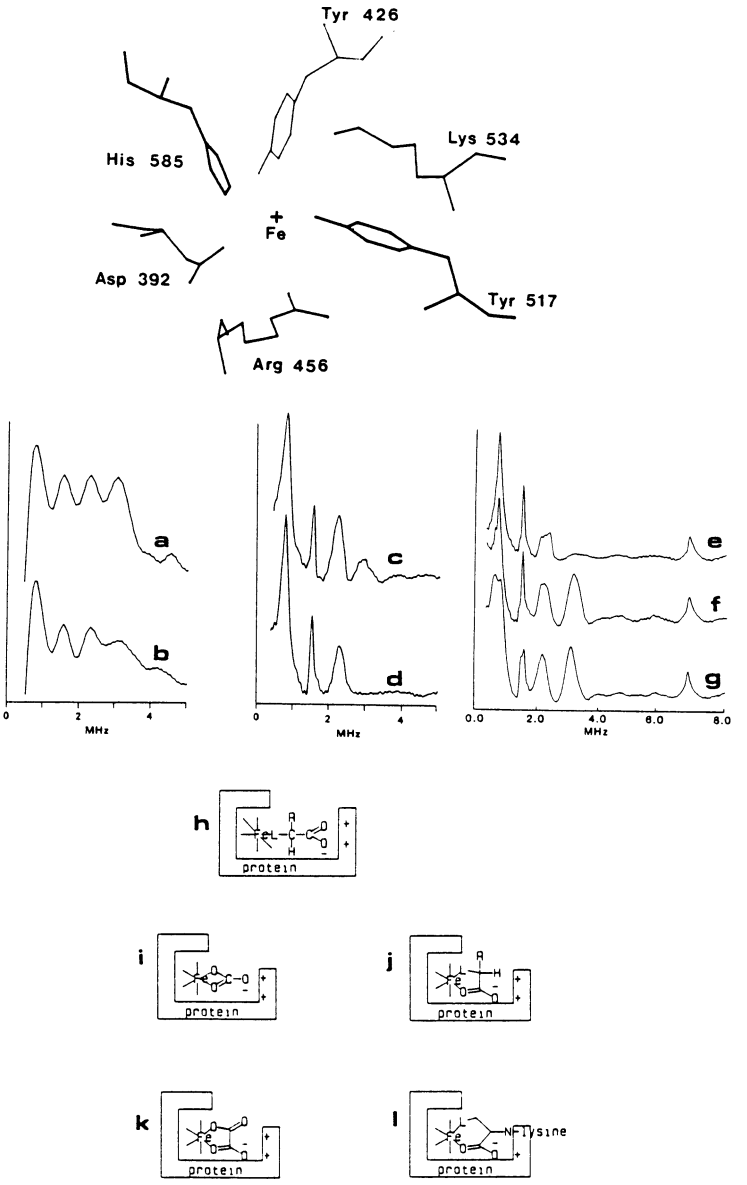

Fig. 24. (Top) Structure of the Fe-binding pocket of rabbit serum transferrin, reprinted from Ref. [225] with permission. (a–g) ESEEM spectra of high-spin Fe^{3+} ($S = 5/2$) transferrin (FeTf) in the presence of synergistic anions; all the spectra were recorded at $T = 2$–3 K at the resonance $g_{eff} \sim 4.3$. (a) Two-pulse data for FeTf-[1-^{13}C]pyruvate; (b) two-pulse data for FeTf-pyruvate; (c) three-pulse data for FeTf-[1-^{13}C]pyruvate; (d) three-pulse data for FeTf-pyruvate; (e) three-pulse ESEEM for FeTf-CO_3; (f) three-pulse ESEEM for FeTf-$^{13}CO_3$. The additional peak at 3.2 MHz is due to ^{13}C($I = 1/2$). (g) three-pulse ESEEM for FeLactoferin-$^{13}CO_3$. The features at 0.7–0.75, 0.80 and 1.57 MHz observed in all spectra originate from the remote ^{14}N of imidazole, with $A = 0.4$ MHz. Figures (h–l) are schematic representations of binding modes for synergistic anions. Figures a–d and h–l are reprinted from Ref. [122], figures e–g are from Ref. [123], with permission.

6.2.2.4. Low-spin iron. Human serum transferrin forms low-spin cyanide adducts [228] at only one of the two iron(III) binding sites — the C-terminal site — characterized by rhombic EPR ($g_x = 2.34$, $g_y = 2.15$, $g_z = 1.92$) [228]. Probably three cyanides are coordinated to the iron. ENDOR data of ^{13}CN-tranferrin revealed that one CN^- binds on the iron along the g_x axis, with a $A_{iso}(^{13}C) = -33.5$ MHz and a carbon–iron distance of ~ 2.1–1.9 Å [153]. ESEEM data on C^{15}N-transferrin allowed the resolution of two cyanide molecules bound in a bend configuration *trans* to one another, along the direction of g_x. The strong hyperfine coupling of the carbon, resolved by ENDOR, precludes detection of ESEEM modulations due to ^{13}C in ^{13}CN-tranferrin. The histidine modulations seen in the native, i.e. high-spin iron containing, protein as well as in Cu^{2+}- and VO-transferrin [123,124] are absent in the CN^- adduct, providing evidence that this protein ligand is displaced by cyanide [229]. Studies with D_2O indicate that the metal is accessible, but not directly coordinated by the solvent. This finding is also consistent with the expectation that CN^- is the preferred ligand relative to H_2O [229].

6.2.2.5. Non-heme iron of Photosystem II. Nitric oxide, NO, binds at the non-heme Fe^{2+} ($S = 2$) of Photosystem II, in competition with bicarbonate [230]. The binding of NO results in the formation of an iron–nitorsyl [Fe–NO] ($S = 3/2$) complex characterized by an axial EPR signal at $g = 4$. The three-pulse ESEEM spectra for [Fe–NO] ($S = 3/2$) are characterized by two types of ^{14}N modulations [107]. With the aid of HYSCORE spectra and numerical simulations it was shown that one type of modulations originate from either two or three nitrogens from imidazoles, which most likely are ligands of the iron [107]. The second type of modulation originates from a single imidazole nitrogen with weaker coupling. Moreover the HYSCORE data reveal a specific proton coupling of ~ 6 MHz from a protein side-chain [107].

6.2.2.6. Dinuclear iron proteins. Oxo-bridged dinuclear iron centers are a common-structural component in the active sites of a number of proteins and enzymes [231]. The mixed valence [Fe(II)–Fe(III)] forms of hemerythrin and methane monoxygenase (MMO), are characterized by $S = 1/2$ ground state, resulting from an antiferromagnetic coupling of an $S = 5/2$ ferric iron, and an $S = 2$ ferrous iron. The diiron center of hemerythrin is coordinated by five histidine residues, rather than two as in MMO [232]. A three-pulse ESEEM investigation of hemerythrin and MMO revealed a characteristic ^{1}H coupling with a strongly anisotropic hyperfine tensor [148]. The proton belongs to a D_2O/H_2O exchangeable group and it was assigned to the OH^- [148], which is a bridging ligand between the metal centers. Modulation from two ^{14}N nuclei were resolved in methane monoxygenase hydroxylase from *Methylococous capsulatus*. The strongly coupled nitrogen ($A_{iso} = 5.0$ MHz, $r_{eff} = 2.2$ Å, $e^2qQ/h = 3.0$ MHz, $\eta = 0.3$) was assigned as a ligand of the ferrous iron [99] while the weakly coupled nitrogen ($A_{iso} = 0.8$ MHz, $r_{eff} = 3.2$ Å, $e^2qQ/h = 1.7$ MHz, $\eta = 0.35$) was assigned to the remote nitrogen of a histidine [148].

Recently, the couplings from five ^{14}N nuclei were resolved by HYSCORE spectroscopy for the diiron center of semimethemerythrin from *Themista zostericola*

[98], four of them having hyperfine parameters in the strong coupling regime, see Fig. 25.

Taking into account the crystal structure from *Themista dyscrita*, these couplings were assigned to coordinated histidine residues, e.g. His-73 ($A_{iso} \sim 5.2$ MHz), His-77 and His-101 (both with $A_{iso} \sim 7.0$ MHz) are coupled to the ferrous atom, while His-25 ($A_{iso} \sim 9.2$ MHz) and His-54 ($A_{iso} \sim 15$ MHz) are coupled to the ferric atom [98]. The nitrogens located axial to the Fe(II)–Fe(III) direction have smaller couplings than the nitrogens coordinated approximately perpendicular to this direction [98]. Noteworthy, the ^{14}N coupling of ~ 15 MHz of His-54 resolved by HYSCORE is among the largest hyperfine couplings ever resolved by ESEEM spectroscopy. In the same work [98], the binding of azide was also studied; in addition to the five histidine couplings, the HYSCORE data allowed the resolution of couplings ($A \sim 2$ MHz, $e^2qQ/h = 1.0$ MHz, $\eta \sim 1$) from the non-coordinated central nitrogen of azide [98].

Uteroferrin is an acid phosphatase with a spin-coupled and redox-active binuclear iron center and is paramagnetic in its, enzymatically active, mixed valence [Fe(II)–Fe(III)] $S = 1/2$ state [233]. A histidine coordinated to the metal center of uteroferrin was identified in an early ESEEM study [234]. In addition, ESEEM investigation of molybdate binding in uteroferrin, which is an inhibitor of its enzymatic activity, revealed a coupling of $A_{iso} = 1.2$ MHz from a single ^{95}Mo atom, which most likely is a ligand of the binuclear iron cluster [234]. ESEEM on D_2O/H_2O samples showed that the metal binding site is easily accessible to solvent and that a proton, possibly from a bridging OH^- group between the two iron atoms coupled ($A_{iso} = 19$–26 MHz) to the metal [234].

6.2.3. Iron–sulfur proteins

Iron–sulfur proteins are a broad group of proteins containing either mononuclear, e.g. rubredoxin-type, or polynuclear clusters [2Fe–2S], [3Fe–4S] and [4Fe–4S], having cystein residues as ligands and sulfine ions as bridging ligands [235]. They participate mainly in electron transfer but some interact directly with substrates [235]. In the mononuclear proteins, the iron atom in its oxidized form is in the high-spin Fe^{3+} ($S = 5/2$) state and its EPR spectrum is characterized by large effective g values, e.g. $g = 9.2$, 4.3, which is typically accompanied by fast spin-lattice relaxation times. So far no ESEEM of mononuclear iron–sulfur Fe^{3+} ($S = 5/2$) center has been reported. Recently an ESEEM study of the mononuclear iron–sulfur center of adenylate kinase has been reported, but with the iron having being converted to its low-spin state, Fe^{3+} ($S = 1/2$) [139]. Polynuclear Fe–S centers are often characterized by effective $S = 1/2$ ground states [235], and the analysis of their ESEEM spectra can be done by the theory of Mims for $S = 1/2$ [11].

6.2.3.1. Adenylate kinase. Adenylate kinase from the Gram-negative bacterium *Paracoccus denitrifants* (AK_{den}) has structural features similar to those of the enzyme from Gram-positive organisms. Recently, it was found that the recombinant protein of dimeric AK_{den} binds simultaneously zinc and iron [139]. The EPR and optical absorption spectra of the bound iron in oxidized form Fe^{3+} ($S = 5/2$),

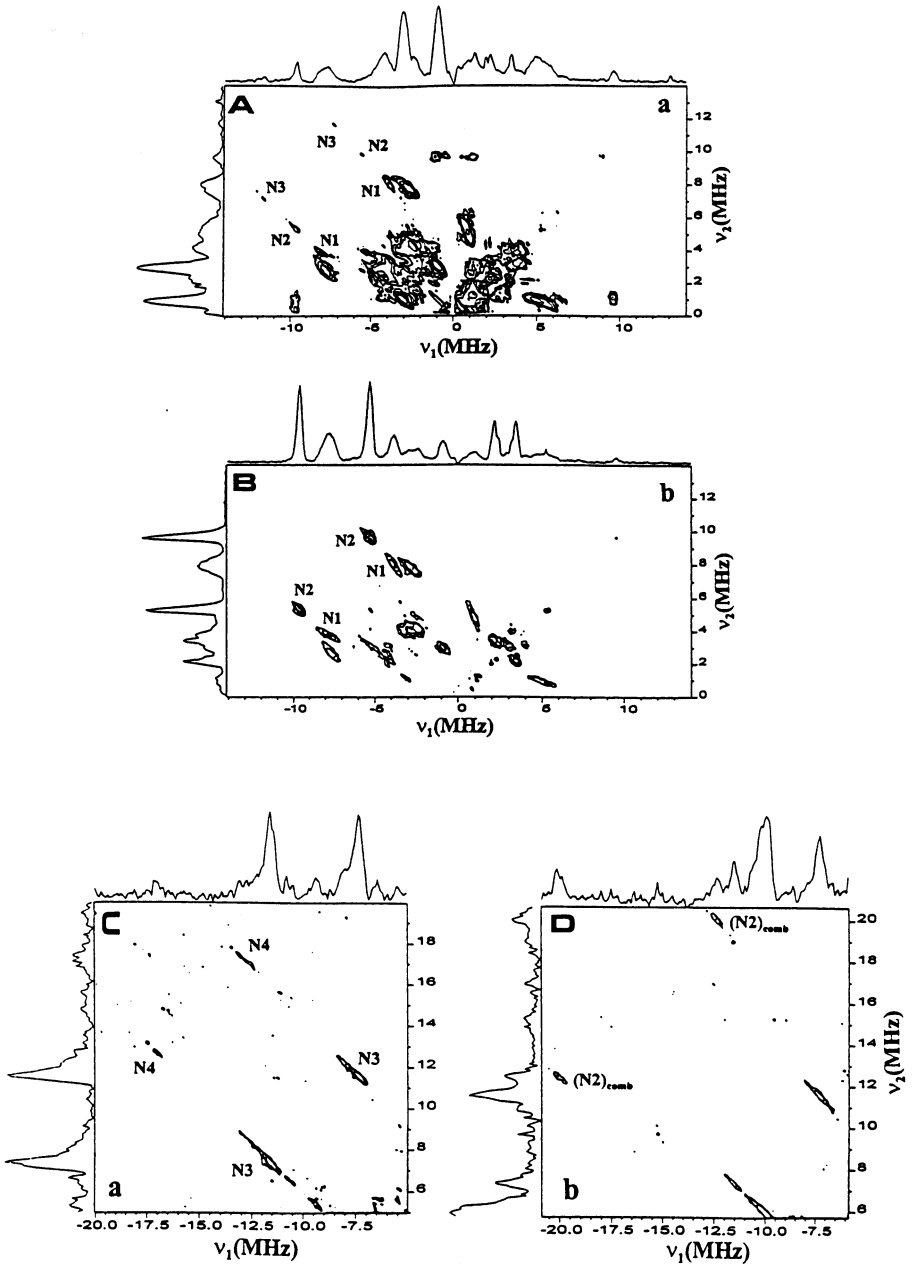

Fig. 25. Contour plots of HYSCORE spectra of semihemerythrin (A) and azidosemihemerythrin (B), recorded at $H = 3570$ and 3580 G, respectively, both for $\tau = 136$ ns. The cross-peaks between the double quantum transitions of strongly interacting nitrogens, see assignments on the figure, appear in the $(+, -)$ quadrant. At different τ values e.g. $\tau = 200$ ns (C) or $\tau = 104$ ns (E), the cross peaks of $^{14}N_4$ with very strong coupling are resolved in (D) while combination lines due to two equivalent N_2 nuclei are resolved in (D). Figures are reprinted from Ref. [98] with permission. Copyright 1998 American Chemical Society.

are similar to those of rubredoxins [139]. Moreover, the amino acid sequence of AK_{den} contains the structural motif Cys-X_2-Cys-X_{16}-Cys-X_2-Cys, which is similar to the iron-binding pocket in the rubredoxin form *Clossrtidium pasteurianum*. ESEEM spectroscopy showed that the non-heme iron in AK_{den} has at least one labile coordination position that can be easily occupied by cyanide, which converts the iron to the low-spin spate. In addition, ^{14}N modulations have been detected in the ESEEM spectrum of cyanide-treated AK_{den} and were assigned to the imidazole nitrogen of His-138 [139]. The unusual coordination environment of the non-heme iron, e.g. a histine ligand together with four cystein sulfurs, was considered to be responsible for the redox properties of the non-heme iron.

6.2.3.2. [2Fe–2S]. The ESEEM experiments performed on the reduced Rieske [2Fe–2S] clusters in cytochrome b_6f of spinach chloroplast, cytochrome $bc1$ complexes from photosynthetic bacteria and bovine mitochondria [236] in complex III of bovine mitochondrial membranes [237], in benzene 1,2-dioxygenase from *Pseudomonas putida* [238], all show two coordinated ^{14}N histidine nitrogens with hyperfine couplings between 3.6–4.5 and 4.6–5.5 MHz. Typically the stimulated ESEEM spectra are characterized by four peaks corresponding to the double-quantum frequencies, Fig. 26(A).

In contrast to the Rieske-type centers, ESEEM investigations of plant ferredoxin-type [2Fe–2S] clusters [239–244] as well as wild type and molecular variants of *C. pasteurianum* ferredoxin [245] show weak interactions with nitrogens having hyperfine couplings of ~ 1 MHz or less. The quadrupole coupling parameters of this type of nitrogen ($e^2qQ/h = 3.2$–3.4 MHz, $\eta = 0.4$–0.5) are characteristic of an amide nitrogen from the protein backbone. Typically, the stimulated ESEEM spectra are characterized by four low-frequency ^{14}N peaks, Fig. 26(B). Recently a X- and C-band (~ 7 GHz) ESEEM study [243] revealed the existence of a second peptide nitrogen bonding to the iron–sulfur center of ferredoxin from the red algae *Porphira umbilicalis* (Fig. 27).

Both types of ^{14}N couplings, e.g. strongly coupled histidines, and weakly coupled peptide-nitrogen, have been resolved in three-pulse ESEEM [246] and HYSCORE [87] investigations of the Rieske-type [2Fe–2S] cluster in 2,4,5-T monoxygenase from *Burkholderia cepacia*, Fig. 28.

ESEEM and ENDOR data of the [2Fe–2S] centers of Rieske protein from *Thermus thermotphilus* and phthalate dioxygenase from *Pseudomonas cepacia* showed they have remarkably similar structures, e.g. both are coordinated to two nitrogens with couplings $A_{iso} \sim 27$ and 9 MHz, respectively, detected by ENDOR [247], and are weakly interacting with an amide protein nitrogen and the remote nitrogen of an imidazole, detected by ESEEM [247].

Recently, HYSCORE investigation of the reduced [2Fe–2S] cluster in D_2O/H_2O exchanged ferredoxin from red marine algae *Porfira umbilicalis* allowed the resolution of five proton couplings [100]. Based on a novel method of analysis of the HYSCORE data, four of them with hyperfine couplings in the range 0.8–2.7 MHz were assigned to β protons from the cysteine ligands, located at distances between 2.8 and 4.5 Å from the iron centers [100].

6.2.3.3. Hydrogenase. In hydrogenase from the purple photosynthetic bacterium *Thiocapsa roseopersicina*, stimulated ESEEM recorded at $g = 2.02$, corresponding to resonances from the [3Fe–4S] cluster, reveals a weak ^{14}N coupling of $A_{iso} \sim 1$ MHz, probably from the second coordination sphere. Nitrogen coupling ($A_{iso} = 1.2$ MHz) with rather unusual quadrupole parameters ($e^2qQ/h = 4.85$ MHz, $\eta = 0.2$) was detected by ESEEM for the H-cluster of hydrogenase I from *Clorostridium pasteurianum* [248] although its origin remains unidentified.

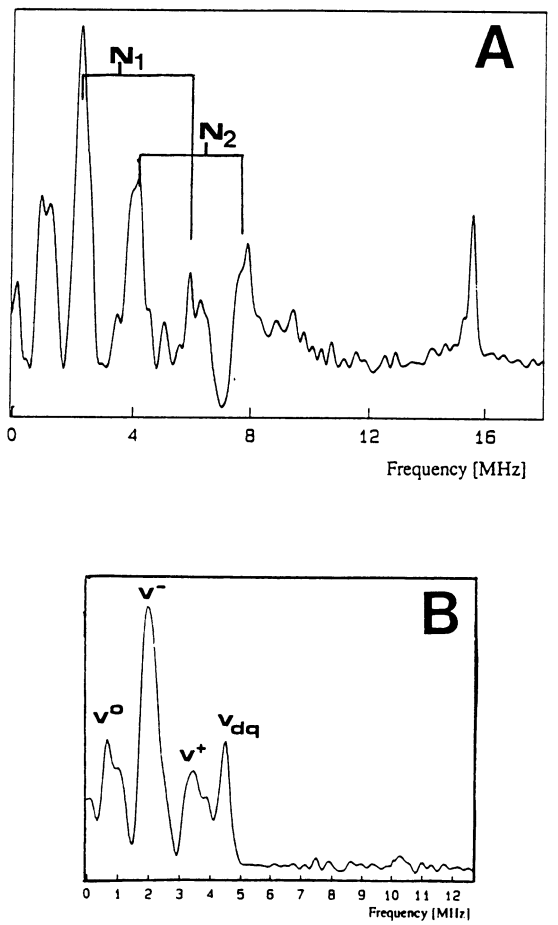

Fig. 26. (A) Three-pulse ESEEM of ascorbate- and TMPD-reduced (TMPD = tetramethyl-*p*-phenylenediaminate) Rieske protein from bovine heart mitochondrial membranes, recorded at $g_y = 1.98$. The spectrum is characterized by the double quantum frequencies, due to two strongly coupled ($A(N1) = 3.4–3.6$ MHz and $A(N2) = 5.2–5.3$ MHz) ^{14}N nuclei from coordinated histidines. (B) Three-pulse ESEEM of dithionite reduced *Spirulina platensis* [2Fe–2S] ferredoxin, at $g = 1.96$. The pattern is characteristic of a weakly coupled ($A \sim -1.1$ MHz) ^{14}N nucleus. Reprinted from Ref. [242] with permission.

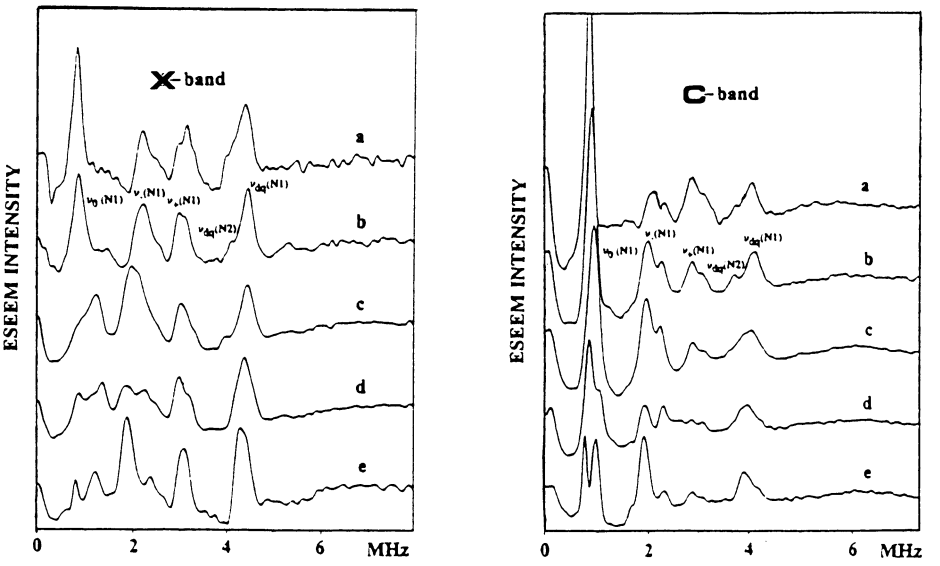

Fig. 27. X-band (9.256 GHz) and C-band (7.232 GHz) three-pulse ESEEMs recorded across the ERP spectrum of reduced [2Fe–2S] ferredoxin in *S. platensis*. The field positions are X-band: (a) 3531; (b) 3490; (c) 3379; (d) 3300; (e) 3231 G. C-band: (a) 2730; (b) 2680; (c) 2639; (d) 2580; (e) 2530 G. Reprinted from Ref. [243] with permission.

6.2.3.4. Carbon monoxide dehydrogenase. The center C of CO-dehydrogenase (CODH) is believed to be an iron-containing cluster of unknown structure. In an effort to better understand its coordination properties, the effects of inhibition with azide on the C center of CODH from *Clorostridium thermoaceticum* were investigated by ESEEM [249]. Comparative $^{14}N_3^-$ versus $^{15}N_3^-$ ESEEM data revealed the existence of strong anisotropic and isotropic nitrogen hyperfine coupling, indicating binding of azide to the paramagnetic center that results from the treatment of CODH with the inhibitor.

6.2.3.5. Nitrogenase. Nitrogenase is a two-component metalloenzyme which catalyses biological nitrogen fixation. The two component proteins are a [4Fe–4S] protein and a heterodimer containing a [8Fe–7S] cluster, called the 'P-cluster', and the FeMo cofactor consisting of a [Mo–7Fe–9S] framework [250,251]. ESEEM investigation of the [4Fe–4S] protein from *Azotobacter vinelandii* and *Closrtidum pausterianum* revealed nitrogen modulations, possibly from a protein backbone nitrogen involved in NH···S type hydrogen bond [252] which were slightly modified by Mg-ADP addition [252]. No modulation from ^{31}P of Mg-ATP were detected and this was interpreted as indication that the phosphate of ATP is not bound to the iron–sulfur center [252]. Prior to the availability of structural models, see Fig. 29, ESEEM had provided evidence for a N-atom from imidazole coupled to the $S = 3/2$ spin system of the FeMo cofactor from *C. pasteurianum* [253]. Further ESEEM investigation in whole cells of *Azodobacter vinelandrii* mutant strains, showed that

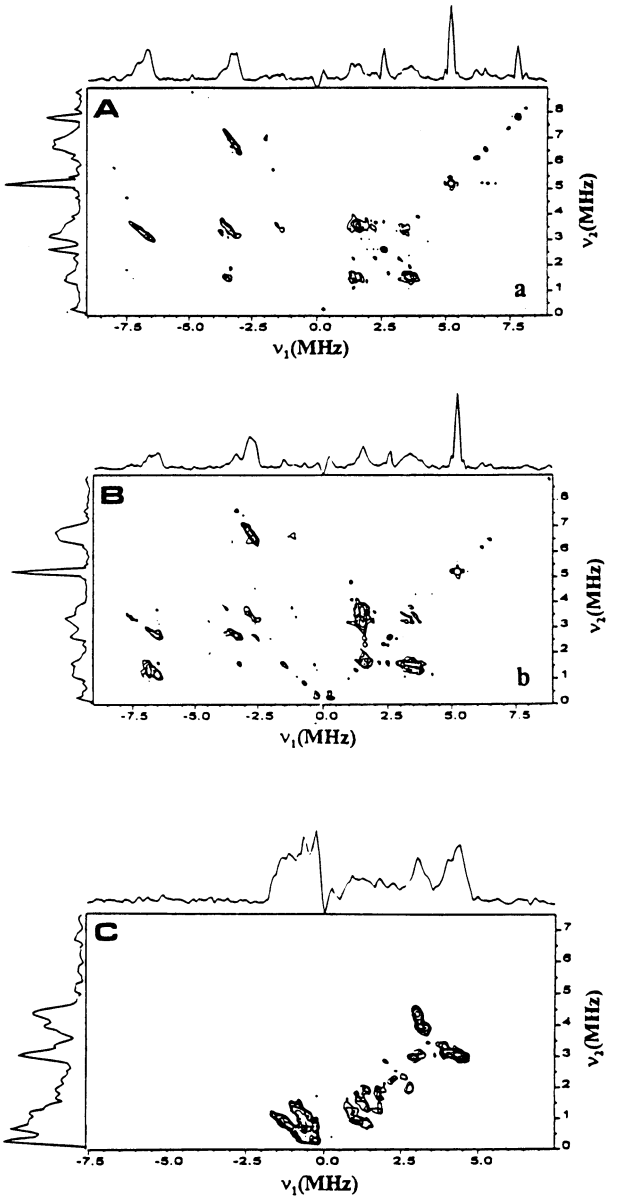

Fig. 28. Contour plots of HYSCORE spectra of 2,4,5-T-monooxygenase recorded at magnetic fields of 3464 G ($\tau = 112$ ns) (A) and 3770 G ($\tau = 104$ ns) (B). The observed cross-peaks originate from double quantum transitions of two coordinated histidine ^{14}N: one (N1, with $A = (4.05$ MHz, 3.88 MHz, 4.01 MHz) is responsible for the features at (-6.5, 2.05 MHz), (3.6, 1.5 MHz), (-6.6, 1.1 MHz) and the second (N2, with $A = (4.71$, 5.07, 5.02)) is responsible for the features at (-7.6, 3.2 MHz). (C) The HYSCORE spectrum of the reduced ferredoxin from *Pseudomonas umbilicalis* recorded at $H = 3550$ G ($\tau = 400$ ns). The cross-peaks at ($+3.9$–4.3, 3.0–3.2 MHz) correspond to the double quantum frequencies of one peptide ^{14}N. Reprinted from Ref. [87] with permission. Copyright 1996 American Chemical Society.

mutation of α-195His by α-195Asn, see structure in Fig. 29, results in the disappearance of the modulation [254] leading to the suggestion that the observed modulation is due to a coordinated imidazole from histidine α-195. The crystallographic data [251], however, revealed that α-195His is not covalently attached to the FeMO cofactor, see Fig. 29, but is within hydrogen bond distance to a bridging sulfide.

In more recent ESEEM work on mutants around the MoFe cofactor of *A. vinelandii*, e.g. α-195His → Asn, α-195His → Gln, see Fig. 29 [106], it was demon-

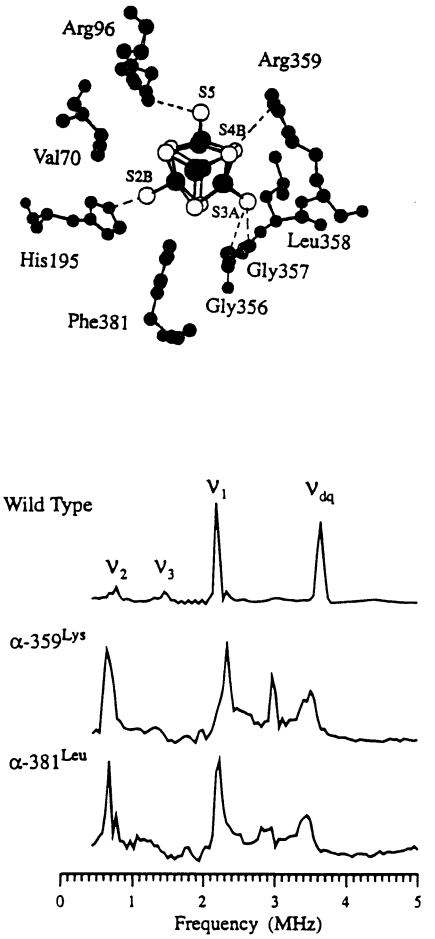

Fig. 29. (Top) Structure of the FeMo-cofactor and selected residues viewed along the threefold axis of the cofactor. (Bottom) Three-pulse ESEEM spectra recorded at $g = 4.3$ of wild-type MoFe protein ($H = 1594$ G, $\tau = 148$ ns) and two mutants, α-395Lys ($H = 1606$ G, $\tau = 148$ ns) and α-381Leu ($H = 1597$ G, $\tau = 148$ ns). The signal in the wild-type arises from one ^{14}N with $A = (0.98, 1.02, 1.14)$ MHz, $e^2qQ/h = 2.17$ MHz, $\eta = 0.59$, from the side chain of α-359Arg. The signals in the mutants arise from one ^{14}N with $A = (0.4, 0.5–0.6, 0.4)$ MHz, $e^2qQ/h = 3.4–3.5$ MHz, $\eta = 0.35$-0.40, from an amide backbone from α-356Gly or α-357Gly. Reprinted from Ref. [255] with permission. Copyright 1998 American Chemical Society.

strated that α-195His is not the origin of the nitrogen modulations. Subsequent analysis, taking into account the coupling parameters for this nitrogen ($A_{iso} \sim 1$ MHz, $e^2qQ/h = 2.2$ MHz, $\eta = 0.5$) led to the suggestion that the nitrogen originates from the side chain of an arginine [255]. This was confirmed by ESEEM data on mutants of the two candidate arginines, α-96Arg and α-359Arg, which demonstrated that the modulation detected by Thomann at al. [253,254] was due to the side-chain nitrogen of α-359Arg [255]. Moreover, ESEEM investigation of the mutant α-359Arg → Lys where the modulation due to α-359Arg was eliminated revealed an additional nitrogen coupling ($A_{iso} \sim 0.5$ MHz, $e^2qQ/4h = 3.5$ MHz, $\eta \sim 0.4$) which was assigned to an amide backbone nitrogen from α-356Gly or α-357Gly [255].

Nitrogen modulations ($A_{iso} \sim 2$ MHz, $e^2qQ/h = 2.8$ MHz, $\eta = 0.7$) were detected in ESEEM and HYSCORE data reported for the reduced hybrid-cluster iron–sulfur protein from *Desulfovibrio desulfuricans* [256]; this coupled nitrogen was tentatively assigned to His-244 [256].

6.3. Mo^V

6.3.1. Sulfite oxidase

Mononuclear Mo enzymes [257] catalyse key 2-electron oxidation–reduction reactions in the metabolism of C, N and S by living organisms, by a formal oxygen atom transfer process. Sulfite oxidase (SO) catalyses the oxidation of sulfite to sulfate coupled with the subsequent reduction of two equivalents of ferricytochrome *c* to ferrocytochrome [257].

Multifrequency ESEEM studies of the Mo^V center of SO in phosphate buffer [258] show that Mo is directly coordinated by at least one phosphate group. The coupling parameters were distributed and this was interpreted as being due to a distribution of the orientations of the phosphate group around the Mo–OPO_3H bond. A combination of 1D-ESEEM and HYSCORE experiments [259] showed that Mo^V, in the high-pH form (pH 9.55) of SO, coordinates a group that includes one solvent-exchangeable D(H), probably in the form of a Mo–OH(D) moiety. The orientation of this –OH group is characterized by a restricted distribution. The modulations due to this group are absent in the high-pH form (pH 7.0) of SO, probably due to a relatively small displacement of the H(D) out of the singly occupied d-orbital of Mo [259]. No ^{14}N modulations have been detected in these studies.

6.3.2. Xanthine oxidase

^{14}N modulation was detected in the form characterized by the 'very-rapid' EPR signal [260] with 2-hydroxy-6-methylpurine substrate bound to Mo. The ^{14}N modulation was assigned to the ^{14}N nuclei of the purine ring and this shows that purine is directly coordinated to Mo. Modulations due to the C_6-methyl deuterons of 2-hydroxy-6-methylpurine were not resolved. From the analysis of the time-domain stimulated ESEEM it was estimated that these methyl groups are at a distance > 4.9 Å from the Mo^V. Modulation from the exchangeable proton at the N_7

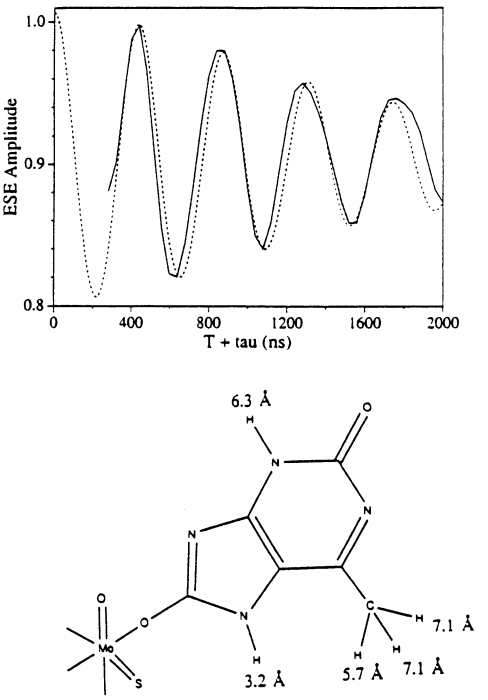

Fig. 30. (Top) Ratio of time domain spectra for the 'very rapid' EPR signal of xanthine oxidase in D_2O versus H_2O. The modulations from ^2H nuclei contribute the dominant modulation. The dashed line is a numerical simulation by the use of two ^2H nuclei, one at a distance of 3.2 Å and another at a distance of 3.9 Å from the Mo spin. (Bottom) Proposed model for the geometric arrangement between the Mo center of xanthine oxidase and the 2-hydroxy-6-methylpurine substrate, based on ESEEM time domain data and molecular modeling. Reprinted from Ref. [260] with permission.

position were resolved, and this allowed an estimation of their distance from the metal to be estimated, e.g. 3.2 Å (Fig. 30).

No ^{31}P has been resolved in the ESEEM spectra and based on this the presence of ^{31}P nuclei in the vicinity of Mo in xanthine oxidase was ruled out [260].

6.4. VO^{2+}

6.4.1. General characteristics

The oxovanadium(IV) or vanadyl ion, VO^{2+}, is very stable and can be substituted for a variety of divalent metal ions in metal-activated enzymes and metalloproteins [261]. The c.w. EPR spectra of $^{51}VO^{2+}$ ($S = 1/2$, $I = 7/2$) provide information about the equatorial coordination environment, mainly through comparison of the electron g and ^{51}V hyperfine (A) matrix with reference compounds [261]. In the ground state of V^{4+} there is a single unpaired electron, $3d^1$, which in square pyramidal vanadyl complexes occupies the $3d_{xy}$ orbital [262]. The V=O bond imposes an approximate axial symmetry which is reflected in the hyperfine splitting

of the EPR spectra i.e. $A_z > A_x \sim A_y$ [261,262]. The d_{xy} orbital is almost purely non-bonding [262], lies on a plane perpendicular to the V=O bond and has its lobes directed between the coordinated ligands [261,262]. As a result the hyperfine couplings of equatorially coordinated magnetic nuclei are small, typically one order of magnitude weaker than the couplings observed for isostructural Cu^{2+} complexes [263–265]. For instance, A_{iso} of the directly coordinated imidazole nitrogens in VO^{2+}-[imidazole]$_4$ is $A_{iso} \sim 6$ MHz [88] while that for the remote ^{14}N of imidazole is almost 20-times smaller, e.g. 0.3 MHz [88]. The same ratio of $\sim 1/20$ holds for the A_{iso} couplings of the remote ($A_{iso} \sim 2$ MHz) [84] versus the coordinated ($A_{iso} \sim 40$ MHz) [89,90] ^{14}N nuclei in Cu^{2+}-[imidazole]$_4$.

6.4.2. Synthetic VO complexes

ESEEM studies of vanadyl ion include, VO^{2+} in water and methanol [266], bis(acetylacetonato)oxovanadium in chloroform/toluene [263], complexes of VO^{2+} with NH_3 and H_2O [70,267], inorganic ligands with equatorial directly coordinated [68,88,92,123,267–271] as well as non-coordinated [163] and axially coordinated [272] nitrogens. In all cases the hyperfine couplings for equatorially coordinated ^{14}N are not within the cancellation condition at the X-band, typically being between ~ 4 and ~ 8 MHz.

The hyperfine coupling of equatorial nitrogens is commonly taken as isotropic or with small anisotropy. An exemplary analysis of the ^{14}N-anisotropic hyperfine as well as the quadrupole tensor for a VO^{2+}-(methylquinolin-8-olato) complex in frozen solution has been worked out recently, based on detailed one-dimensional ESEEM at the C- and X-band, as well as HYSCORE at the X-band [273]. The ^{14}N anisotropic hyperfine tensor was found to be rhombic with principal values (0.06, 0.51, -0.57 MHz) all are much smaller than the isotropic component, $A_{iso} = -6.2$ MHz. Such almost pure isotropic tensor results in the three-pulse ESEEM spectra which are dominated by the double quantum transitions at ν_{dq+} and ν_{dq-} transitions, Eq. 22a,b, see spectrum Fig. 5 for $A_{iso} > 2\nu_I$, see also Fig. 32(A). These features can be used for a first estimate of the coupling parameters:

$$A_{iso} = \frac{\nu_+^2 - \nu_-^2}{8\nu_I} \tag{36a}$$

$$K^2(3+\eta^2) = \left(\frac{\nu_\pm}{2}\right)^2 - \left(\nu_I \pm \frac{1}{2}A_{iso}\right)^2 \tag{36b}$$

The single-quantum, ν_{sq}, transitions have frequencies [275]

$$\nu_{sq}^{\pm} = 1/2\nu_{dq}^{\pm} \mp 3K \tag{37}$$

For collinear **g**, **A** and **Q** tensors, their modulation depth is zero when the magnetic field is parallel to any of the principal axes. In cases when the tensors are not collinear, then ν_{sq} transitions may become detectable [92,275]; thus observation of single-quantum transitions may be used to diagnose non-collinear **g**, **A** and **Q** tensors [275]. Due to the highly anisotropic ^{51}V-hyperfine tensor, $A_z/A_{x,y} \sim 3$, the ESEEM spectra recorded at magnetic fields across the EPR spectrum are orienta-

tion-selective [68]. The analysis of such 'single-crystal-like' spectra allows a comprehensive magnetic resonance picture of the electronic and geometrical structure of the nitrogen coordination in an oxovanadium complex [68,92].

The hyperfine coupling for ^{14}N nuclei of hydroxamates bound to VO^{2+}, which is two bonds away from VO^{2+}, gives rise to well resolved ESEEM features [162], see Fig. 31.

The corresponding coupling, $A_{iso} = 1.6–2.2$ MHz [162], is smaller than the $A_{iso} = 4–8$ MHz usually observed for directly coordinated nitrogens, but larger than the $A_{iso} = 0.3$ MHz observed for the remote imidazole nitrogen [88] which is separated by three bonds from VO^{2+}. An exceptionally low hyperfine coupling for directly coordinated ^{14}N, $A_{iso} \sim 1.7$ MHz, was reported for the complex of VO^{2+} with dithiocarbamate (LVOdtc) and hydrotris(3,5-dimethyl-1-pyrazyl)borate [274]. This hyperfine coupling is rather puzzling since the crystal structure of LVOdtc does not appear to deviate strongly from other complexes [274]. A possible explanation offered was that this complex possess a pseudo-threefold axis symmetry, leading to a deviation of the unpaired electron spin density from the plane defined by the nitrogen-donor and vanadium atoms [274] which in turn results in diminished ligand–metal overlap.

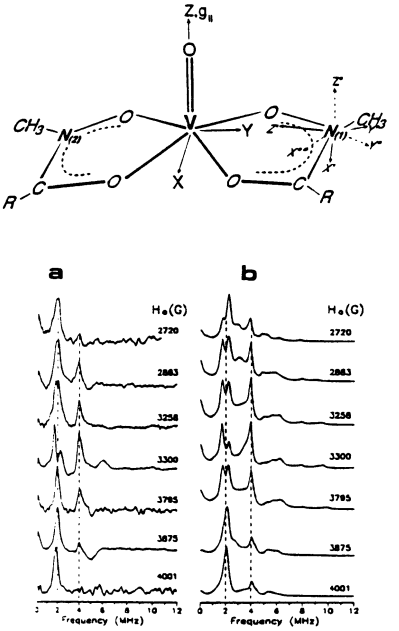

Fig. 31. (Top) A schematic representation of hydroxamate binding, and the principal axis systems of the g and $A(^{51}V)$, (X, Y, Z), the ^{14}N hyperfine (x', y', z') and quadruple (x'', y'', z'') tensors. The orientations of (x', y', z') and (x'', y'', z'') in the figure are arbitrary. (Bottom) Experimental (a) and simulated (b) ESEEM spectra of VO-RL261 in methanol, recorded across the EPR spectrum. The signals originate and is from a ^{14}N nucleus, with $A_{iso} = 1.8$ MHz, $e^2qQ/h = 4.0$ MHz, $\eta = 0.84$. Reprinted from Ref. [163] with permission. Copyright 1995 American Chemical Society.

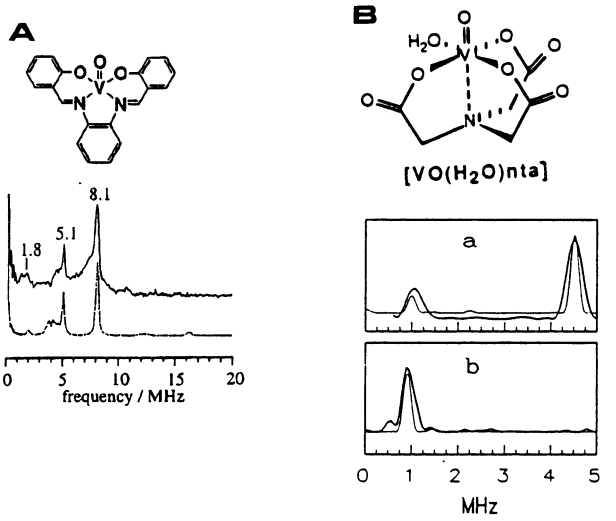

Fig. 32. (A) Three-pulse ESEEM spectrum of VO(salophen) in 1:1 DMF–toluene v/v glass ($H = 2634$ G, $\tau = 270$ ns). The spectrum is characterized by two double-quantum transitions typical for ^{14}N nuclei ($A_{iso} = 6.2$ MHz in VO(salophen)) equatorially coordinated in VO complexes. Reprinted from Ref. [270] with permission. (B) Three pulse ESEEM spectrum of [VO(H_2O)nta] ($H = 3427$ G, $\tau = 190$ ns). The spectrum has characteristic peaks at e.g. 1 and 4.6 MHz, originating from the axially coordinated ^{14}N nucleus, with $A_{iso} = 1.35$ MHz much lower than the couplings encountered for equatorially coordinated nitrogens. Reprinted from Ref. [272] with permission. Copyright 1998 American Chemical Society.

6.4.2.1. Axially coordinated nuclei. Usually, in VO^{2+}-complexes the hyperfine coupling between the electron spin and axial nuclei, *trans* to the V=O double bond, is too weak to be resolved by ESEEM at the X-band. A four-pulse ESEEM study of aquo-VO^{2+} complexes showed that the couplings of the electron spin with the equatorial protons are 10–100-times larger than those with the axial water protons [33].

Recently, in an ESEEM study of complexes of the type [VO(H_2O)L] (L = *N*-(2-acetzamido)iminodiacetic acid, *N*-(2-hydroxyethly)iminodiacetic acid or nitriloacetic acid) the detection of ^{14}N couplings from axially coordinated amine was reported [272]. The A_{iso} for this axial amine was found to be ~ 1.3 MHz, with non-negligible anisotropy, e.g. $T \sim 0.4$ MHz deduced according to the point dipole model, based on a V–N_{amine} distance of 2.3 Å according to X-ray data [272]. The molecular orbital origin of this exceptional axial coupling has not been analysed so far. The axial ^{14}N gives rise to a characteristic ESEEM pattern e.g. a peak at ~ 4.5 MHz together with weaker features at around 1 MHz [272] in the stimulated ESEEM spectrum, Fig. 32(B), which is easily distinguished from the ESEEM patterns from equatorial ^{14}N nuclei, Fig. 32(A).

The spectral features observed for the axial ^{14}N atom [272] bear similarities to those observed earlier in ESEEM spectra for the M2 unit of Chloroplast F_1-ATPase [276]. Accordingly, the previously observed spectra were postulated to originate from axial nitrogen coordination to vanadyl, from the ε-amino nitrogen of a lysine residue [272].

The ESEEM data reported so far for nitrogens coordinated equatorially to VO^{2+} ion suggest an intriguing relationship between the magnitude of the hyperfine couplings and the type of the nitrogens. For amine nitrogens, the $V–N_{amine}$ couplings appear to range from $|A_{||}| = 4.4–5.4$ MHz and $|A_{\perp}| = 3.6–4.9$ MHz for amine nitrogen adducts of $VO(acac)_2$ [263], $|A_{iso}| = 5.0–5.1$ MHz for $VO(gly)_2$, [121,270], 4.7 MHz for $VO–NH_3$ on a silica supported vanadium oxide [70], and 4.98 MHz for VO(edda) [270]. The hyperfine couplings for amine nitrogens are smaller than the couplings reported for imine nitrogens which are in the range $\sim 6–7$ MHz, e.g. $|A_{||}| = 6$ MHz and $|A_{\perp}| = 5.6$ MHz for imine nitrogen adducts of $VO(acac)_2$ [263], $|A_{iso}| = 6$ MHz for $VO(meox)_2$ and 6.4 MHz for $VO(mim)_4$ Cl [92,273], $|A| = 7.1$ MHz and 7.6 MHz for pyridine and imidazole adducts of $VO(hexafluoro\text{-}acac)_2$, respectively [123], $|A_{iso}| = 6.5$ MHz for imidazole adduct of $VO(Himac)_2$ [271], $|A_{iso}| \sim 5.8$ MHz for VO(salen) and VO(salophen) [271]. So far, the highest hyperfine coupling reported is that observed for $VO–(NCS)_4$ $|A_{iso}| = 7.47$ MHz [270], and for VO-porphyrin complexes [269], $|A_{iso}| = 7.2–7.3$ MHz.

Fukui et al. [271] have suggested that the s-orbital content of the sp^n hybrid orbital of coordinated nitrogen may be correlated with the isotropic hyperfine couplings. The plot in Fig. 33, helps to visualise the suggested trend: $A_{iso}(sp) > A_{iso}(sp^2) > A_{iso}(sp^3)$ [270].

This correlation, although attractive, does not apply in all cases, e.g. the coupling of pyrrole nitrogens in VO-porpyhrin, appears to be higher than predicted for sp^2 hybridization. Nevertheless, the hyperfine coupling values may serve as useful reference data for the identification of the nitrogen type in VO complexes.

6.4.3. Vanadyl in proteins

6.4.3.1. Imidazole glycerol phosphate dehydratase (IGPD). IGPD catalyses the dehydration of imidazole glycerol phosphate to imidazole acetyl phosphate which is

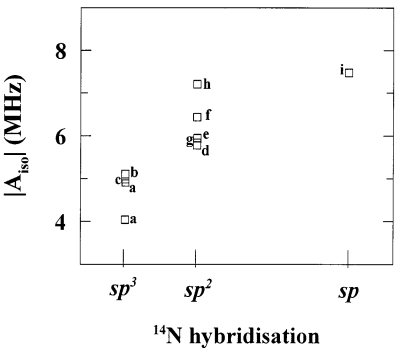

Fig. 33. Plot of experimental A_{iso} values, observed for equatorial ^{14}N in VO complexes versus ^{14}N hybridization: (a) amine ^{14}N of $VO(acac)_2$ [263]; (b) $VO(gly)_2$ [270]; (c) VO(edda) [270]; (d) imine ^{14}N of $VO(acac)_2$ [263]; (e) $VO(meox)_2$ [273]; (f) $VO(mim)_4Cl$ [92]; (g) VO(salen) [271]; (h) VO(TPP) [269]; (i) $VO(NCS)_4$ [270].

an important step in the biosynthesis of histidine. ESEEM of the VO^{2+} derivative of IGPD from *Saccaromyces cerevisiae* revealed the existence of strong ^{14}N coupling, $A_{iso} = 7.0$ MHz, from coordinated imidazole [277] Additional low frequency components were detected in the ESEEM spectrum but no definitive assignment was provided [277].

6.4.3.2. Bromoperoxidase. Native bromoperoxidase contains V^{5+} while its reduction with dithionite results in an axial EPR spectrum, similar to that observed in VO^{2+} complexes. Although the crystal structure of native V^{V}-chloroperixidase was recently reported [278], the structure of the reduced enzyme is an open question. The only ESEEM spectrum reported for reduced bromoperoxidase (V–BrPO) [279] contains features at 3.1, 4.2, 5.3 and 8.1 MHz, Fig. 34(A), recorded for non-orientation selective magnetic field setting. The analysis of the these frequencies remains puzzling. Although it is considered that these originate from ^{14}N nuclei the exact assignments are controversial [270,272,280]. In [280], based on previous ESEEM data for VO-imidazole where the imidazole ring is perpendicular to the equatorial plane [138], the frequencies 5.3 and 8.1 MHz were assigned to a coordinated imidazole, see Fig. 34(D).

Furthermore, prompted by the detection and assignments of modulations from axially coordinated nitrogen in model VO^{2+} compounds, Fig. 34(C), these authors postulated the assignment of the 4.2 MHz feature to an axial nitrogen [280], Fig. 34(D), while the 3.0 MHz peak was postulated to arise from a nitrogen donor significantly displaced from the equatorial plane of the vanadyl ion [272]. In [271], the ESEEM spectra of newly synthesized VO-imidazole model, see Fig. 34(B), with the imidazole ring parallel to the equatorial plane, have double quantum frequencies at 4.8 and 8.6 MHz while the 3.4 and 5.3 MHz are the single-quantum frequencies. Accordingly, it was postulated that two equatorial imidazoles may be the origin of all the spectral features seen in VBrPO [271].

6.4.3.3. Puruvate kinase. Puruvate kinase is a nonmetalloprotein, which requires two divalent metal ions and a monovalent cation, for activation, presumably Mg^{2+} and K^{+}, respectively, in vivo. Vanadyl can function as the divalent ion replacing Mg^{2+} [121]. ESEEM data recorded at two frequencies, e.g. 8.8 and 10.0 GHz, contained ^{14}N modulations with $A_{iso} = 4.9$ MHz, $e^2qQ/h = 2.55$ MHz and $\eta = 0.5$, assigned to a coordinated lysine, see Fig. 35(A,B) [121]. ^{13}C-contact interactions were resolved between VO^{2+} and [1-^{13}C]pyruvate ($A_{iso} = 2.2$ MHz) [2-^{13}C]pyruvate ($A_{iso} = 5.4$ MHz), Fig. 35(C,D).

Such coupling requires a through-bond interaction between the carbon and the vanadyl and shows that the pyruvate is a bidentate ligand to the metal [121]. ESEEM data for VO^{2+}-pyruvate kinase, contained the Larmor frequencies of monovalent cations Na^{+}, K^{+} and Cs^{+} indicating that these cations are in close proximity to the metal site [121].

6.4.3.4. S-Adenosylmethinine (AdoMet) synthetase. AdoMet-synthetase catalyses a reaction in which the adenosyl group of ATP is transferred from the triphosphate

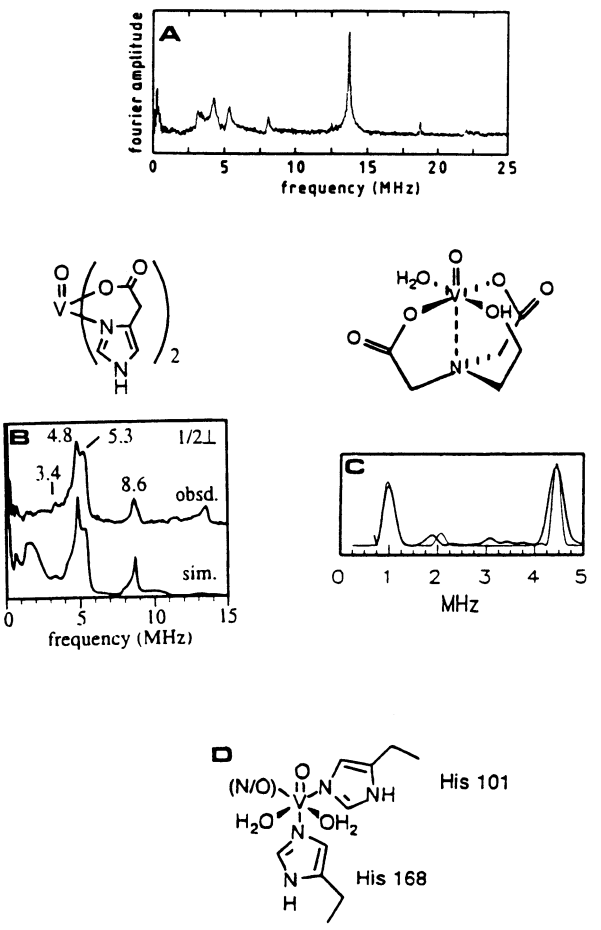

Fig. 34. (A) Three-pulse ESEEM, for reduced vanadium bromoperoxidase. Data were recorded at the non-orientation selective field setting, $m_I = -1/2$, for $\tau = 380$ ns, $H = 3240$G. Reprinted from Ref. [279] with permission. (B) Three-pulse ESEEM and simulation for $VO(Himac)_2$ in v/v H_2O/ethylene glycol glass. Data were recorded at non-orientation selective field setting, $m_I = -1/2$ for $\tau = 300$ ns, $H = 3185$ G. Based on the similarities of the spectrum (B) to that in (A) it was postulated the in reduced vanadium bromoperoxidase the ESEEM features indicate equatorial ^{14}N ligation like in $VO(Himac)_2$ [271]. Based on similarities of the ESEEM spectrum of axially coordinated nitrogen (C) to those in (A), an axially coordinated ^{14}N was suggested to contribute to the ESEEM of reduced vanadium bromoperoxidase, see model (D), [280]. Reprinted from Ref. [280] with permission. Copyright 1997 American Chemical Society.

moiety to the sulfur atom of L-methionine. Based on ESEEM data in samples containing either ^{14}N or ^{15}N it was shown that a lysine is coordinated to VO^{2+} [138]. In the substrate complex enzyme VO^{2+}-ATP-methionine-K^+, an equatorially coordinated lysine was found with $A_{iso} \sim 4.3$ MHz. In the intermediate enzyme, the lysine coupling is stronger, $A_{iso} \sim 4.8$ MHz. In the product enzyme VO^{2+}-AdoMet-

K^+, the ESEEM data shows that the lysine is not coordinated to the metal and that the methionyl nitrogen ($A_{iso} \sim 5.3$ MHz) is coordinated to VO^{2+}.

6.4.3.5. ATP-ase. The soluble part F1 of the APT synthase, which retains the ability to hydrolyze ATP to ADP after isolation, bears sites for divalent metal binding. ESEEM spectroscopy has been applied to study the F1 ATPases isolated from spinach chlorplasts (CF1) or from the thermophilic bacterium *Bacillus* PS3 (TF1) [281,282]. In CF1 using VO^{2+} as paramagnetic probe, the ESEEM data showed that two of the three metal-binding sites, called M2 and M3, in the absence of a nucleotide, involve one amine ligand each from a lysine side chain [281]. When

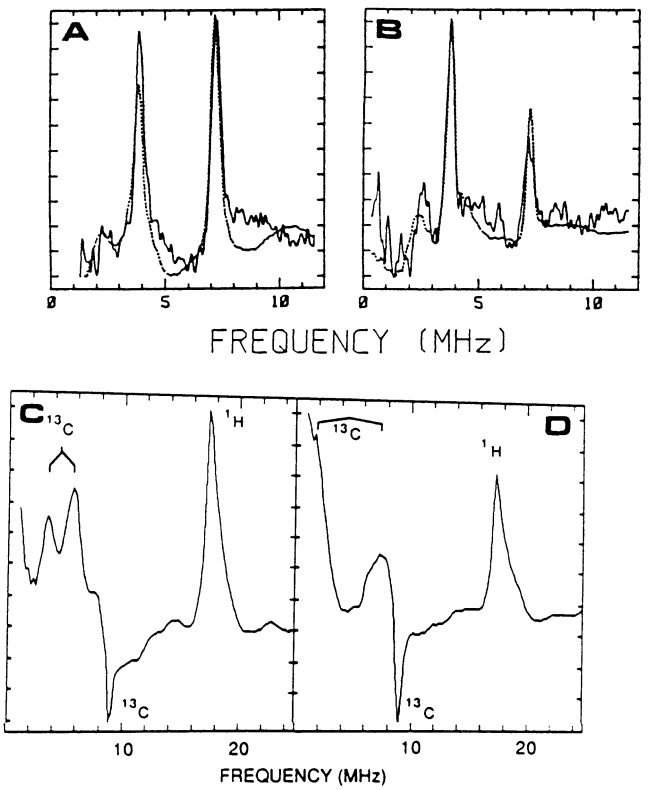

Fig. 35. (A) Three-pulse ESEEM of VO(glycinate)$_2$, recorded at 8.8 GHz, $H = 3130$ G. Dashed line is a simulation for two ^{14}N nuclei with similar hyperfine couplings $A = (4.85, 4.85, 5.3$ MHz). (B) ESEEM for the VO-pyruvate–phoshoenolpyruvate complex, recorded at 8.8 GHz , $H = 3130$ G. Dashed line is the simulation for one ^{14}N nucleus with $A = (4.8, 4.8, 5.1$ MHz). (C) Two-pulse ESEEM spectrum for VO-pyruvate kinase-[1-^{13}C]pyruvate; the positive ^{13}C signals corresponds to a hyperfine coupling of 2.2 MHz. (D) Two-pulse ESEEM spectrum VO-pyruvate kinase-[2-^{13}C]pyruvate; the positive ^{13}C signals correspond to a hyperfine coupling of 5.4 MHz. The negative ^{13}C signals near 9 MHz in both C and D correspond to the sum combination harmonics. Reprinted from Ref. [121] with permission. Copyright 1989 American Chemical Society.

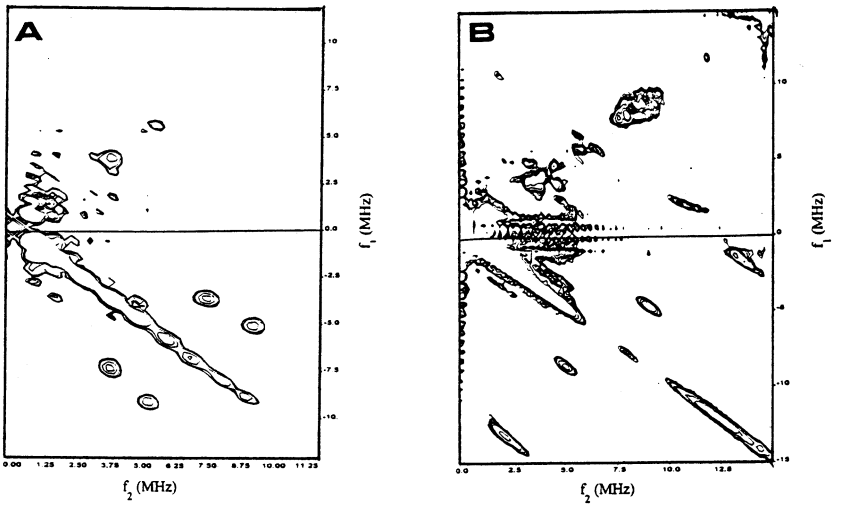

Fig. 36. (A) Contour plot of HYSCORE spectrum of VO^{2+} complexed with TF1, recorded at $H = 3415$ G, 9.57 GHz, $T = 4.2$K. (B) Contour plot of the HYSCORE spectrum of the VO^{2+}-TF1-ATP complex, recorded at $H = 3419$ G. Reprinted from Ref. [282] with permission. Copyright 1996 American Chemical Society.

VO^{2+} is added to CF1 in the presence of ADP, the ESEEM data show nitrogen modulations, tentatively assigned to an axial ^{14}N from β-Lys-162 for the M3 site and/or from α-Lys175 for the M2 site [276]. In VO^{2+}-TF1, three-pule ESEEM and HYSCORE data detect two nitrogen ligands to VO^{2+}, with couplings $A_1 = 4.75$ MHz, $e^2qQ/h = 2.8–3.2$ MHz, and $A_2 = 6.5$ MHz, $e^2qQ/h = 2.0–2.3$ MHz, respectively, Fig. 36(A) [282]. On the basis of these couplings, the ligands were identified as a lysine terminal amine and a histidine imidazole. In VO-TF1-ATP the HYSCORE data show correlation peaks which are interpreted as hyperfine couplings with $^{31}P_\alpha$ and $^{31}P_\beta$ from ATP equatorially bound to VO^{2+}, with $A(^{31}P_\beta) = 8.7$ MHz and $A(^{31}P_\alpha) = 15.5$ MHz, Fig. 36(B).

6.4.3.6. Apoferritin. Ferritins are proteins that store iron as a hydrous ferric oxide mineral core of ~ 80 Å diameter within a highly symmetrical assembly of 24 20 kDa subunit proteins [283]. The role of the protein shell in the formation of the hydrous ferric oxide core of ferritin is poorly understood. An ESEEM study of VO^{2+}-appoferitin revealed the presence of ^{14}N-nuclei, coordinated *cis* to the vanadyl ion, with hyperfine coupling $A_{iso} \sim 6.7$ MHz at pH 5.5 and $A_{iso} \sim 6.5$ MHz at pH 7.4 [65]. Analysis of the proton sum-combination harmonics in multifrequency two-pulse ESEEM for samples prepared is either H_2O or D_2O reveal the presence of a solvent-exchangeable hydrogen located very near the perpendicular plane of the vanadyl complex, approximately ~ 2.6 Å from the vanadium center [65]. These ESEEM results were interpreted in terms of a binding site that accommodates VO^{2+} with one aquo plus one histidine ligand, and with other coordination positions filled by protein carboxylate donors [65].

6.4.3.7. D-Xylose isomerase. The intracellular enzyme D-xylose isomerase from *Streptomyces ridiginosus* catalyses in vivo the reversible isomerization of α-D-xylose to α-D-xylulose [284]. The VO^{2+} ion inhibits the enzymatic activity, after binding in one of the two metal binding-sites (site B). ESEEM data demonstrate the existence of an equatorially coordinated nitrogen from a histidine, with $A_{iso} =$ 6 MHz [68]. A detailed analysis of the basic and the combination harmonics of this nitrogen in orientation selective two-pulse ESEEM, including second-order treatment and complete simulation of the $g_{\|}$ and $g_{\perp}$ spectra, allowed the determination of the nuclear quadrupole and hyperfine tensor principal directions [68], Fig. 37.

Analysis of the sum-combination harmonics in four-pulse data revealed the presence of two protons, e.g. having dipolar couplings of 2.3 and 3.6 MHz which translate to distances of 3.25 and 2.8 Å from the metal, respectively.

6.4.3.8. Particulate methane mono-oxygenase. The particulate methane mono-oxygenase (pMMO) is a copper protein, [285] and is much less well-characterized than the soluble MMO (sMMO) whose active site contains a non-heme binuclear iron cluster. The number of copper ions strongly bound by pMMO is large, up to 15 copper ions per pMMO unit, and it has been suggested that they are primarily arranged in multinuclear clusters that are unlike other multinuclear copper centers found in metallobiochemistry [285]. Recently, three-pulse ESEEM and pulsed-ENDOR revealed that the C-clusters of pMMO have two distinct sets of pMMO copper-sites, i.e. one with multiple ^{14}N nuclei weakly coupled, i.e. $A_{iso} \sim 2.2$ MHz to the metal spin, in addition to one with at least one strongly bound nitrogen, $A \sim 38$ MHz [145]. Both nitrogens were assigned to imidazole from histidines of pMMO, and based on this it was suggested that the active site is located at the periplasm interface [145].

Recently ESEEM spectroscopy has been applied for the first time to organs of an animal, e.g. the kidney and liver of a rat treated with vandyl sulfate [286]. For both organs, ^{14}N-modualtion was detected, typical of nitrogens coordinated to vanadyl. From the coupling parameters determined by ESEEM, e.g. $A_{iso} = 5.2$ MHz for the kidney and 5.0 MHz for the liver, it was postulated that the nitrogens originate from either the Lys ε-amine or the N-terminal α-amine of a protein [286].

6.5. Co^{2+}

6.5.1. General characteristics

The study of oxygen affinity in oxygenated ferrous, Fe^{2+}, globins is not amenable for EPR study since they are EPR silent. Replacing the heme with cobalt protoporphyrin IX [287] may result in an oxygenated hemoprotein that has a slower auto-oxidation rate and a metal center ($S = 1/2$) amenable for EPR studies. ESEEM spectra of oxyCo hemoproteins and model compounds are useful probes for the ionicity of the cobalt–dioxygen bond [288–292].

6.5.2. Synthetic Co compounds

In low-spin $Co^{2+}(dmg)_2X_2$ (dmg = Bis(dimathylglyoxime), $X = CH_3OH$ or pyridine) [293] ESEEM signal had been observed from the equatorial directly coordinated ^{14}N-nuclei (Fig. 38).

Their hyperfine coupling is equivalent being $A_{iso} = 2.1$ MHz when CH_3OH is axially coordinated and $A_{iso} = 1.7$ MHz when pyridine is axially coordinated. This

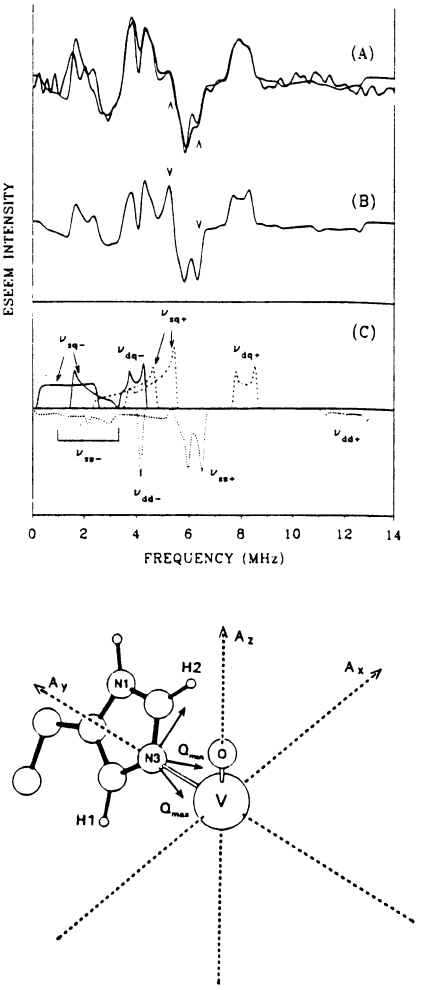

Fig. 37. (top) Cosine FT of two-pulse ESEEM (A, thick line) of VO^{2+} D-xylose isomerase, recorded at $H = 3571$ G. Thin lines in A and B are simulations, both for one histidine nitrogen with $A_{iso} = 5.65$ MHz, but different ^{51}V hyperfine tensors: $A(^{51}V) = (63, 63, 182$ G) in (A), $A(^{51}V) = (62, 64, 182$ G) in (B). In (C) an explanatory deconvolution of the ESEEM spectrum is presented, where the shapes of the various ^{14}N nuclear transitions are explicitly marked. (Bottom) Structural mode of histidine coordination in VO^{2+} D-xylose isomerase, based on the ESEEM data. Reprinted from Ref. [68] with permission. Copyright 1995 American Chemical Society.

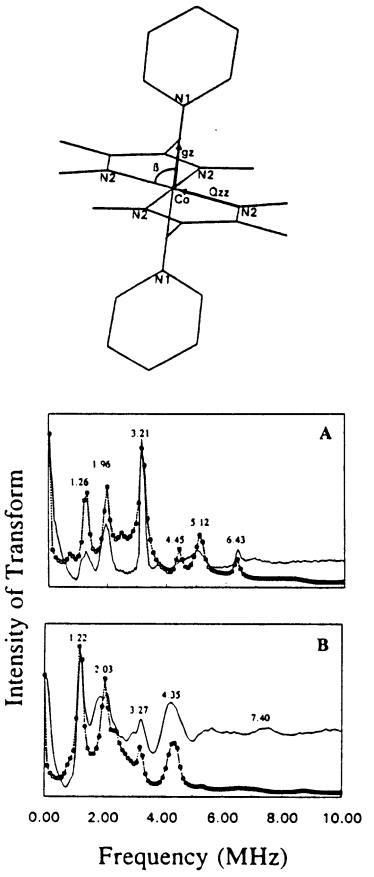

Fig. 38. Three-pulse ESEEM (solid lines) and simulations (dashed lines) of (A) $Co^{2+}(dmg)_2(CH_3OH)_2$ and (B) of $Co^{2+}(dmg)_2(^{15}N(py)_2$ (dmg = bis-dimethylglyoxime).The structure of the *trans*-(dmg)bis(pyridine)-cobalt(II) complex is shown on the top. Reprinted from Ref. [293] with permission. Copyright 1995 American Chemical Society.

reduction of the hyperfine coupling shows that the unpaired electron, localized on the d_{z^2} cobalt orbital, is decreased upon coordination of pyridine. The principle axis of the quadrupole interaction is found to lie along the Co–N σ bond in the equatorial dmg plane. This result is in contrast to what is seen for the low-spin iron porphine (TPP) complexes [209] where the principal quadrupole axis deviates by, e.g. 45° from the equatorial plane.

In high-spin Co($S = 3/2$) complexes, in contrast to the low spin compound, no modulation from equatorial directly coordinated nitrogens is resolved, [294]. In high-spin cobalt the three unpaired electron occupy the $d_{x^2-y^2}$, d_{z^2} plus one of the other d orbitals, a configuration which allows strong hyperfine coupling with the equatorial nitrogens, and this renders them non-detectable by ESEEM. When axial imidazole is coordinated, ESEEM modulations are resolved yielding an $A_{iso} = 1.3$

MHz, assigned to the non-coordinated remote nitrogen. Based on shifts of the two-pulse combination lines from weakly coupled protons, the distance between coordinated water protons from the cobalt was estimated to be ~ 2.9 Å [294].

6.5.3. Co-substituted hemoproteins

ESEEM spectra of oxyCo globins arise from coupling of the unpaired electron on bound O_2 [295] to the Co-bound N_ε of the proximal histidyl imidazole [288,289]. The interpretation of the ESEEM results was based on a molecular orbital model for the cobalt–dioxygen unit [295] that contains a fully occupied σ-bonding orbital,

$$|\Psi_1\rangle = sp^2(N_\varepsilon) + d_{z^2}(Co^{2+}, \downarrow) + \pi^*(O_2, \uparrow)$$

and a half-occupied anti-bonding orbital

$$|\Psi_2\rangle = \pi^*(O_2, \uparrow),$$

where N_ε is an axially coordinated imidazole nitrogen (Fig. 39).

This model, predicts that electron nuclear hyperfine coupling to the axial nitrogen N_ε occurs through spin polarization of the fully occupied $|\Psi_1\rangle$ [296]. Accordingly, a decrease in the cobalt character in $|\Psi_1\rangle$ or increase of the ionicity of the cobalt–dioxygen bond, results in a decreased spin transfer at the N_ε nucleus, that is a decreased hyperfine coupling for N_ε. Moreover, an increased sp^2 lone-pair donation from N_ε to cobalt is predicted for increased cobalt character in $|\Psi_1\rangle$ or decreased cobalt–dioxygen bonding, [295,296], and this in turn would result in reduced nuclear quadrupole coupling parameters [288,289].

Within this context, ESEEM studies revealed that the nuclear hyperfine and nuclear quadrupole couplings to an axial ^{14}N reflect the degree of oxygen character or ionicity of the cobalt–dioxygen bond [288–290] which in turn is correlated with the oxygen affinity [291]. The ionicity of the Co-dioxygen bond is influenced by hydrogen bonding, polar amino acids or polar solvents: all three factors increase the ionicity of the Co-dioxygen bond and can be probed by ESEEM via the

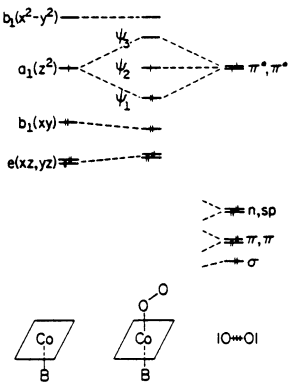

Fig. 39. Molecular orbital model for the coordination of dioxygen to cobalt(II) complexes. Reprinted from Ref. [295] with permission. Copyright 1976 American Chemical Society.

subsequent reduction of the ^{14}N-nuclear quadrupole coupling of the axial histidine [290].

In an ESEEM study of $(\alpha Co–O_2)_2(\beta Fe–O_2)_2$ and $(\alpha Fe–O_2)_2(\beta Co–O_2)_2$ hybrid hemoglobins, e.g. where the iron was selectively substituted by cobalt in either the α- or the β-subunit, smaller N_ε hyperfine and quadrupole couplings were found for the oxyCo α rather than for the oxyCo β-subunits [291]. Furthermore, these ESEEM experiments on D_2O versus H_2O hybrid protein indicated that hydrogen bonds to the bound O_2 are present both in oxyCo α and oxyCo β-subunits, see Fig. 40.

The smaller hyperfine coupling observed for the oxyCo α subunits was attributed to a more ionic and therefore shorter cobalt–dioxygen bond, whereas the reduced nuclear quadrupole coupling indicates increased overlap of the sp^2 hybrid of N_ε with the cobalt d_{z^2} and thus a shorter $Co–N_\varepsilon$ bond. These results were considered to be consistent with a crystal structure of $(\alpha Fe–O_2)_2(\beta Fe–O_2)_2$ [297] which shows shorter Fe–O and $Fe–N_\varepsilon$ bonds for the oxyFe α-subunits, and higher oxygen affinity for the oxyCo α than for oxyCo β subunits [298].

More recently, a parallel ESEEM and extended absorption X-ray structure (EXAFS) study of [oxyCo]-[TPP]-[1-methylimidazole] revealed that increasing the polarity of the solvent results in shortening of the cobalt-axial nitrogen ($Co–N_\varepsilon$) bond, from 2.12 (for 100% toluene) to 1.94 Å, (for 1:1 toluene–dichlormoethane). No shortening of the cobalt–dioxygen bond was resolved in these studies [292]. The increased polarity of the solvent increases the oxygen affinity of the metal due to an increase in the ionicity of the cobalt–dioxygen bond that is manifested in reduction of the electron nuclear coupling to the axial nitrogen and shortening of the ($Co–N_\varepsilon$) bond.

The observed increase in the ionicity of the oxygen character in the $|\Psi_1\rangle = sp^2(N_\varepsilon) + d_{z^2}(Co^{2+}) + \pi^*(O_2)$ orbital signifies a shift towards the $sp^2(N_\varepsilon) + d_{z^2}(Co^{3+}) + sp^2(O_2^{\bullet -})$ structure [292]. This makes the binding of molecular oxygen to cobalt bear some resemblance to the binding to ferrous heme iron where the bonding orbital is considered to be of the form $sp^2(N_\varepsilon) + d_{z^2}(Fe^{3+}) + sp^2(O_2^{\bullet -})$, i.e. an oxidation process [299]. This similarity was invoked in order to explain the parallel trends observed in oxygen affinity for native ferrous and cobalt substituted hemoproteins [292].

6.5.4. Bleomycin

The bleomycins are members of a family of antibiotic glycopeptides that in vitro break DNA in a O_2-dependent oxidation of drug-bound Fe^{2+}. It is considered that the in vivo antitumor activity of bleomycins is based on the same reaction [300]. ESEEM spectra of $[Cu^{2+}]$- and $[Co^{2+}(S = 1/2)]$-bleomycin revealed low-frequency modulations which were assigned to the remote nitrogen of a coordinated imidazole. ^{14}N-modulations were also detected for $[Fe^{2+}(S = 1/2)]$-bleomycin, but with no further evaluation [301].

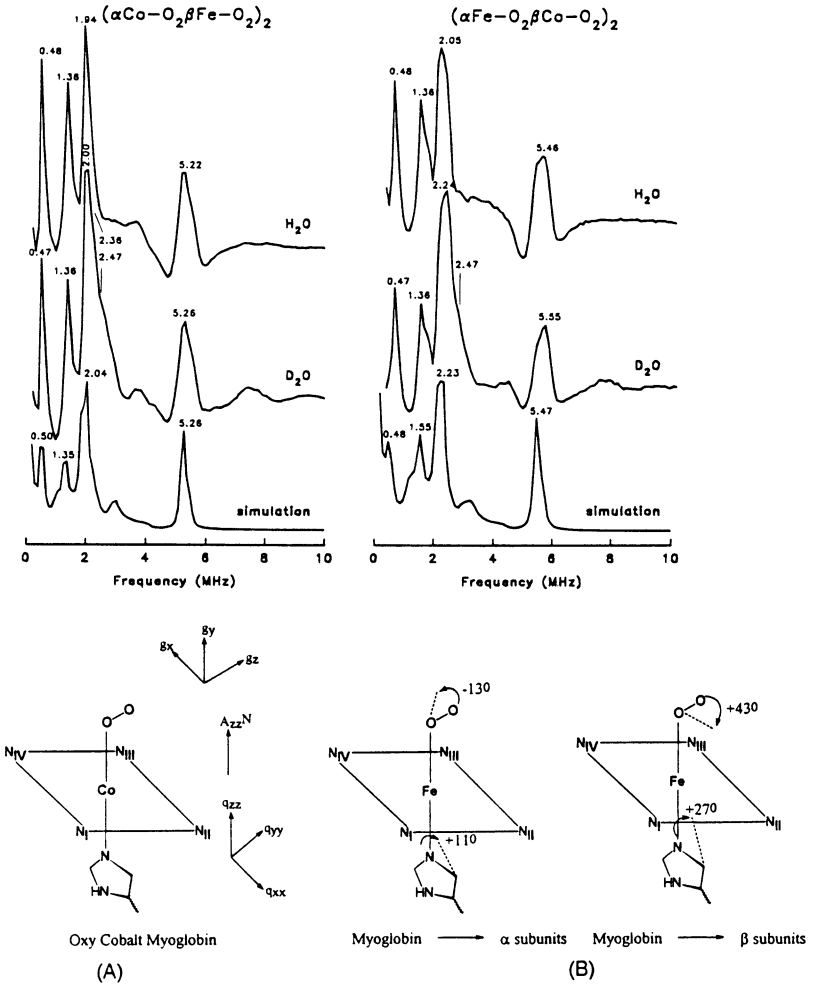

Fig. 40. Top: (Left panel) ESEEM spectrum of $(\alpha Co–O2\beta Fe–O_2)_2$ hemoglobin in H_2O (pH 6.78) and D_2O (pD 7.06), respectively. (Right panel) ESEEM spectrum of $(\alpha Fe–O2\beta Co–O_2)_2$ hemoglobin in H_2O (pH 6.78) and D_2O (pD 7.06), respectively. Bottom: (A) Schematic representation of the magnetic tensor orientation. (B) Comparison of the molecular structure of the heme site of oxyferrous myoglobin and hemeglobin. Dotted lines represent the positions of the O–O bond and the proximal imidazole C_δ–C_ε axis in the ocyFe hemoglomin units. Reprinted from Ref. [291] with permission. Copyright 1995 American Chemical Society.

6.6. Manganese

6.6.1. General characteristics

The $^{55}Mn^{2+}$ ion has nuclear spin $I = 5/2$ and is usually encountered in the high-spin $S = 5/2$ state [2]. The formulas developed by Mims to describe the two- and three-pulse ESEEM for $S = 1/2$ spins [11] are not directly applicable in the case

of Mn ($S = 5/2$). This is due to the small zero-field splitting, $D \sim hv$, which does not allow the effective $S = 1/2$ formalism [1] to be applied (see Section 3.6). Recently, the theory of two-pulse ESEEM for $S = 5/2$ electron spin has been described [83,111] but this is applicable only to weakly coupled $I = 1/2$ nuclei. In Ref. [83] the analysis was based on a simplified picture where the total ESEEM is considered to be the sum of contributions from transitions between successive M_S levels [83]. Coffino and Peisach [111] performed analytical calculations based on the density matrix formalism [3,11] and concluded that the zero field splitting term, although assumed to be small, gives rise to angle selection effects in ESEEM spectra of Mn^{2+} ($S = 5/2$). So far, the theory for other, interesting and commonly encountered cases, i.e. ESEEM due to ^{14}N($I = 1$) coupling to Mn^{2+} ($S = 5/2$), is not available.

6.6.2. Synthetic Mn compounds

In an early report [302], the ESEEM due to deuterium coupled to Mn^{2+} was evaluated based on comparison of the signals from one ^2H coupled to Mn^{2+}, e.g. form Mn^{2+}-EDTA, and six deuterium nuclei, e.g. from Mn^{2+}-$(^2H_2O)_6$ [302]. In another case, quantitative analysis of the data from weakly coupled protons has been worked out, considering the Mn^{2+} spin as a pseudo $S' = 1/2$ system [303]. In an alternative approach, the relative ^2H–Mn distances in Mn^{2+} complexes with deuterated malate have been deduced from the relative intensity of the ^2H peaks in the frequency-domain ESEEM spectra [304].

Due to the non-availability of theoretical ESEEM data for ^{14}N–Mn^{2+}, the interpretation of the ESEEM data for ^{14}N coupled to manganese, has been based exclusively on comparison with pertinent ESEEM spectra for simple model Mn complexes, see for example Fig. 41. Usually no estimation for the coupling parameters, hyperfine or quadrupole, is reported.

Thus the interpretation of ESEEM for ^{14}N coupled to Mn^{2+} remain qualitative and no identification of the nitrogen type can be achieved from the coupling parameters, as for example in the ceases of Cu^{2+} and VO^{2+} complexes.

6.6.3. Mn-proteins

6.6.3.1. Cytochrome c oxidase. The ligation environment of a tightly bound Mn^{2+} in cytochrome *c* oxidase from *Rhodobacter sphaeroides* has been characterized by EPR and ESEEM [305]. Multifrequency three-pulse ESEEM results provide direct evidence for a nitrogen ligand to the Mn^{2+}, which is assigned to a histidine by comparison with ESEEM studies of Mn^{2+}-bound lectins [306] and specifically to His-411 in subunit 1 on the basis of mutagenesis studies [307]. From these results a partial model of the Mn^{2+} binding site has been constructed, Fig. 42.

From the ESEEM data, the His-411 is assigned as a ligand, whereas Asp-412 may serve as a hydrogen bond acceptor and form a hydrogen bond with the water molecule ligated to the metal.

6.6.3.2. Tartrate dehydrogenase. Tartrate dehydrogenase (TDH) is induced in *Pseudomonas putida* by growth on (+)-tartrate as the sole carbon source and

catalyzes the first step in the catabolism of tartrate, the NAD^+-dependent oxidation of (+)-tartrate to oxaloglycolate. TDH requires a divalent metal ion for catalytic activity and shows a strong preference for Mn^{2+} [121]. Mn^{2+}·tartrate dehydrogenase·substrate complexes have been examined by ESEEM spectroscopy [308]. The occurrence of dipolar interactions between Mn^{2+} and ^2H on [^{2}H]pyruvate and [4-^{2}H]NAD(H) confirms that Mn^{2+} binds at the enzyme active site. The tartrate analogue oxalate was observed to have a significant effect on the binding of NAD(H). Oxalate appears to constrain the binding of NAD(H) so that the nicotinamide portion of the cofactor is held in close proximity to Mn^{2+}. Oxalate also affected $^{133}Cs^+(I = 7/2)$ binding. The intensity of the ^{133}Cs ESEEM signal increased in the presence of oxalate, which suggests that oxalate facilitates binding of Cs^+ to the active site or that Cs^+ binds closer to Mn^{2+} when oxalate is present [308], see Fig. 43. In addition to signals from substrates, ESEEM spectra revealed ^{14}N signals that arose from coordination to Mn^{2+} by nitrogen-containing ligands from the protein. However, the identity of this ligand or ligands remains obscure.

Fig. 43 illustrates a possible arrangement of the substrates in the active site of TDH. Mn^{2+} is shown with one nitrogen-containing ligand, although there may be more than one.

6.6.3.3. F-type H^+-ATPase. The metal binding sites of isolated F1 ATPase from spinach chloroplasts (CF1) and from the thermophilic bacterium *Bacillus* PS3 (TF1) have been studied by EPR and pulsed EPR spectroscopy using Mn(II) as a

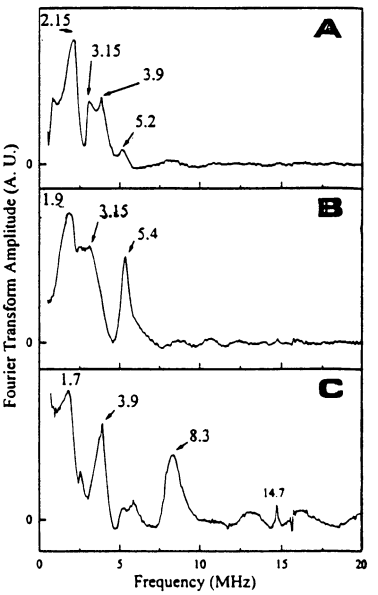

Fig. 41. Three-pulse ESEEM for frozen solution samples of $Mn^{2+}(S = 5/2)$ complexed with glycine (A), imidazole (B), and ATP (C), recorded at $H = 3460$ G, 9.68 GHz, $\tau = 136$ ns. Reprinted from Ref. [309] with permission. Copyright 1996 American Chemical Society.

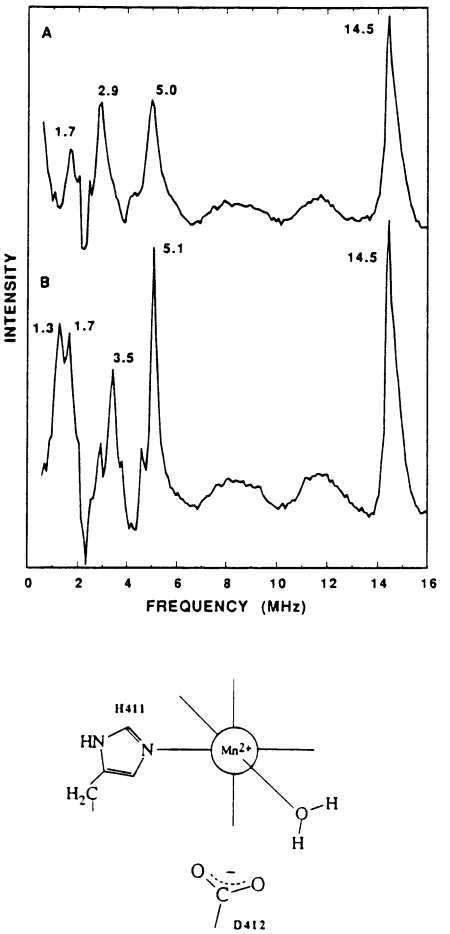

Fig. 42. Three-pulse ESEEM spectra of (A) oxidized ($H = 3375$ G, 8.98 GHz, $\tau = 225$ ns) and (B) reduced ($H = 3375$ G, 8.97 GHz, $\tau = 225$ ns), *Rhodopseudomonas sphaeroides* cytochrome *c* oxidase containing 0.7 Mn/enzyme. A partial model of the Mn binding site is depicted. While Asp-412 is shown as deprotonated, the actual protonation state of this residue is not known. Reprinted from Ref. [305] with permission. Copyright 1995 American Chemical Society.

paramagnetic probe [309]. The ESEEM spectra of complexes of Mn(II) with CF1 were recorded for different Mn/CF1 rations. For a complex with 0.8 Mn/CF1, the ESEEM spectrum shows two frequencies at 3.7 and 8.6 MHz that are attributed to the magnetic coupling with ^{31}P with a hyperfine coupling constant of $|A| \sim 5.3$ MHz, reflecting the interaction with a phosphate group from the endogenous ADP molecule. For Mn(II) complexes with higher Mn/CF1 ratios, new frequency components below ~ 5 MHz are resolved in the spectra in addition to the peaks from ^{31}P. Similar experiments for a Mn(II) complex with TF1 (0.4 Mn/TF1) showed no interaction with ^{31}P. Instead modulations are detected in the ESEEM

below ~ 5 MHz that are attributed to a ^{14}N ligand. This is tentatively attributed to the deprotonated amine of Lys-162 from a β subunit [309]. Addition of the substrate ATP to this Mn·TF1 complex leads to the formation of a ternary Mn·TF1·ATP complex with coordination of the Mn(II) by a phosphate group from the ATP as judged from the ESEEM results ($|A(^{31}P)| \sim 4.5$ MHz). An increase in the hyperfine coupling constant of ^{31}P of the phosphate bound to Mn(II) to $|A(^{31}P)| \sim 5.1$ MHz is observed after incubation of the ternary complex at room temperature. This may reflect conformational changes of catalytic significance that occur in the nucleotide-binding site during hydrolysis of ATP to ADP by this complex [309].

6.6.3.4. Lectins. Lectins are cell-agglutinating metalloproteins that bind to specific carbohydrate determinants. They contain Mn^{2+} and Ca^{2+}, which are both required for maximal saccharide-binding activities. However, only in the case of Con A has the role of the metal ions been elucidated in detail. The X-ray crystallo-

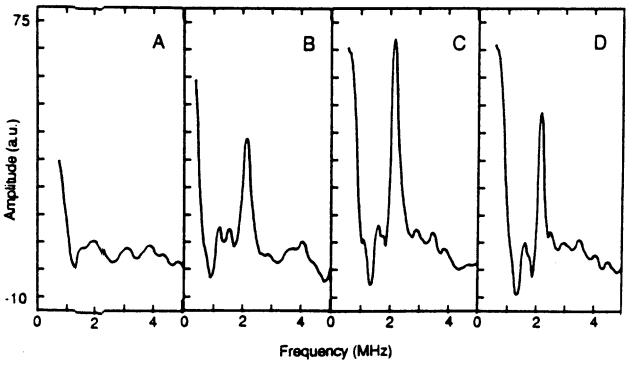

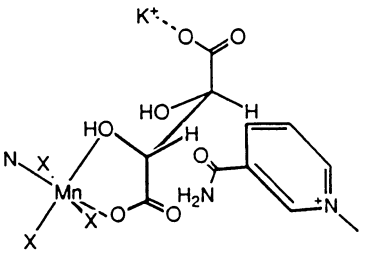

Fig. 43. Three-pulse ESEEM of Mn-tartrate dehydrogenase(TDH)-[4-^{2}H]NAD(H) complexes. (A) Mn-TDH-[4-^{2}H]NAD$^+$; (B) Mn-TDH-[4-^{2}H]NAD$^+$-oxalate; (C) Mn-TDH-(R)[4-^{2}H]NADH-oxalate; (D) Mn-TDH-(S)[4-^{2}H]NADH-oxalate. Data were collected at 1.8 K, $H = 3325$ G, 9.30 GHz, $\tau = 212$ ns. A schematic representation of the Mn binding site is presented at the bottom of the figure. Tartrate is shown as a ligand to Mn, which has one nitrogen ligand, although there may be more than one. Reprinted from Ref. [308] with permission. Copyright 1991 American Chemical Society.

graphic structure of Con A shows the Mn^{2+} and Ca^{2+} distance to be 4.25 Å, with the latter adjacent to the carbohydrate-binding site [310]. ESEEM experiments have been used to investigate the Mn^{2+}-binding site in a series of lectins including concanavalin A, pea lectin, isolectin A from lentil, soybean agglutinin, *Erythrina indica* lectin, and *Lotus tetragonolobus* isolectin A [306]. Together with model studies, the results provided direct evidence for a single nitrogen atom of a conserved residue bonded directly to Mn^{2+} in all of the above systems. ESEEM measurements of the lectins exchanged with deuterium oxide, together with model studies, provided evidence for the presence of two water molecules coordinated to the Mn^{2+} in all of the proteins [306]. Binding of saccharides was observed to have little effect on the structural features of the Mn^{2+} site in the lectins as determined by ESEEM.

6.6.3.5. N-ras p21. p21 is a guanine nucleotide binding protein of $M_r \sim 21\ 000$ encoded by *ras* genes [311]. Nuclear couplings from $^{31}P_\beta$ ($A_{iso} = 4.7$ MHz, $T = 0.86$ MHz) and $^{31}P_\alpha$($A_{iso} = 0$ MHz, $T = 0.21$ MHz) of the GDP were resolved [83,312] in a multifrequency ESEEM study of Mn^{2+}·GDP complexes of *N-ras* p21. From the anisotropic couplings, the distances between $^{31}P_\alpha$, $^{31}P_\beta$ and the Mn^{2+} atom were estimated to be ~ 5.3 and ~ 3.3 Å, respectively in good agreement with crystallographic data. ^{15}N modulations from serine-17 amide were observed, originating from a dipolar coupling $T = -0.15$ MHz which is translated to an effective ^{15}N–Mn distance of ~ 4 Å. Other ESEEM studies revealed that an aspartate residue is indirectly coordinated to Mn through a water molecule [120]. Based on ESEEM data for [^{2}H-3]Thr-labeled Mn^{2+}·GMPPNP·p21, the distance between the Mn(II) and the deuterium-label of the hydroxy group of Thr35 in frozen aqueous solution was estimated to be ~ 4.9 Å [313]. Recently, a detailed ESEEM study revealed that the Mn(II)·nucleotide binding site is accessible to solvent and to cryoprotectants, and the glycerol binds in the first coordination sphere of the metal [314].

6.6.3.6. Creatine kinase and concanavalin A. ESEEM spectroscopy has been used to detect Mn(II)-ligand superhyperfine couplings in complexes with creatine kinase and in concanavalin A [131]. In transition-state analogue complexes of creatine kinase (enzyme-Mn^{II}ADP-anion-creatine), superhyperfine interactions from the directly coordinated nitrogen of the thiocyanate, NCS^-, ligand give envelope modulations. ESEEM data recorded for the ^{14}N and ^{15}N forms of thiocyanate confirmed the assignment of the modulations to the nitrogen of NCS^-. From the ^{15}N spectrum, the apparent nitrogen coupling was estimated to be ~ 3.8 MHz [131]. On the other hand, the nitrogen of coordinated NO_3^-, which is two bonds removed from the paramagnetic center, does not produce detectable modulations. Attempts to observe ESEEM from ^{17}O (40 atom% enrichment) in the phosphate groups of ADP were without success.

In spectra for Mn(II) concanavalin A, modulations are detected due to the nitrogen of the coordinated histidine residue. Complexes prepared in ^2H_2O give strong signals due to weakly coupled ^2H. For Mn(II)-doped single crystals of

sodium pyrophosphate, signals are observed in the frequency domain spectra that are due to coupling from ^{31}P. Phosphorus signals from the ADP ligand in complexes with creatine kinase showed approximately the same coupling constant but have a much broader line width [131].

6.6.3.7. Glutamine synthetase. Glutamine synthetase catalyzes the synthesis of glutamine from glutamate, ammonia and ATP. The X-ray crystal structure has been reported [315]. Glutamine synthetase has an absolute requirement for two divalent metal ions per subunit for catalysis. EPR and ESEEM were used to study the environment of Mn^{2+} bound to the tight (n_1) metal ion binding site of glutamine synthetase in the presence of analogues of the tetrahedral adduct, L-methionine (*S*)-sulfoximine [Met(O)(NH)–S] and L-methionine (*R*)-sulfoximine [Met(O)(NH)-R] [133]. Superhyperfine coupling due to the ^{14}N nucleus of the imine nitrogen of the sulfoximine moiety of Met(O)(NH)–S but not of Met(O)(NH)-R has been detected by ESEEM spectroscopy. Two intense peaks are evident in the presence of Met(O)(NH)–S with frequencies at 1.7 and 3.3 MHz [133]. These peaks are absent when [^{15}N]imine-labeled Met(O)(NH) is used, indicating the presence of the sulfoximine nitrogen of Met(O)(NH)–S in the inner coordination sphere of the metal ion. Also supporting this conclusion is the fact that no peaks at 1.7 and 3.3 MHz were found when L-methionine sulfone or phosphinothricin was bound in place of Met(O)(NH).

6.6.4. Multinuclear Mn-centers

Multinuclear manganese complexes are utilized in a number of metalloenzymes [316]. Prominent examples are manganese catalase [316] and the oxygen-evolving complex (OEC) of Photosystem II [317]. Recently ESEEM spectroscopy has been used to study binuclear Mn(III)Mn(IV) complexes with effective $S = 1/2$ ground states, in part to provide spectroscopic and structural evidence for multinuclear Mn enzymes [126,318,319].

Dipolar interactions measured with ^1H- and ^2H-ESEEM in combination with ^1H-pulsed ENDOR allowed the determination of Mn–H distances in a μ-alkoxo bridged Mn(III)Mn(IV) complex [318]. Analysis of proton ENDOR and combination frequencies in two-pulse ESEEM, Fig. 44(A,B), gives radial Mn(III)–H distances of 2.65 and 2.47 Å for protons of ligated water and a distance of 2.65 Å for the alcohol proton of ligated methanol, Fig. 44(C). A time-domain ESEEM pattern for the methyl-ligated system was simulated by using three purely dipolar proton interactions of $T_{dip} = 2.19$, 3.60 and 5.71 MHz. Analysis of these couplings was performed based on a model where the coupled proton experiences a point dipolar interaction with each Mn [318], giving Mn(III)–H distances of 3.0, 3.5 and 4.0 Å for the three methyl protons.

^{14}N modulations have been resolved in ESEEM spectra for[$(tacn)_2Mn^{III}Mn^{IV}(\mu\text{-}O)_2(\mu\text{-}Ac)](Bph_4)_2$ [126] and [$(bpy)_4Mn^{III}Mn^{IV}(\mu\text{-}O)_2](ClO_4)_3$ [320] with comparable coupling parameters, e.g. $A_{eff} = 2.8$ and 2.0 MHz, $e^2qQ/h = 2.5$ and 2.3 MHz for both complexes, respectively [126,320]. These weak couplings were assigned to the equatorial nitrogens bound to the Mn^{III} side of the complex [126,320].

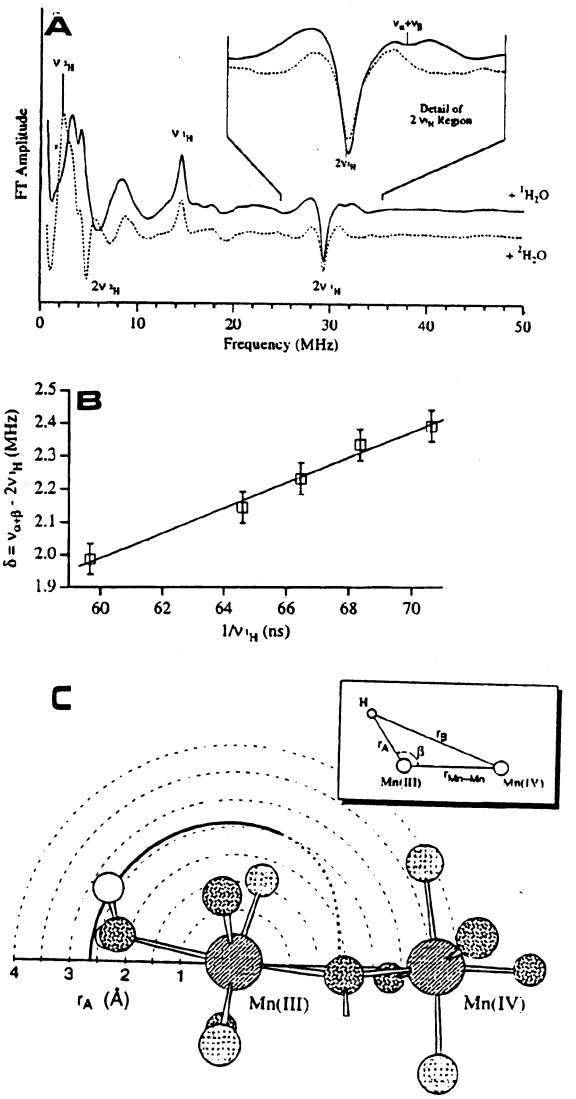

Fig. 44. (A) Two-pulse ESEEM ($T = 4.2$ K, $H = 3437$ G, 10.228 GHz, $\tau = 120$ ns) of a symmetric Mn(III)Mn(IV)(2-OH-3,5-Cl2-SALPN)$_2$ complex ligated by H_2O or ^2H_2O. The inset shows an expanded view of the ^1H sum combination region, from which the dipolar interaction of the bound water can be determined. (B) Graph showing the dipolar-induced shift from $2\nu(^1H)$, δ, in the two-pulse ESEEM across the EPR spectrum. The magnetic fields are 3327, 3437, 3535, 3937 G. (C) Contour plot showing where the hyperfine value, A_y, is held constant at 8.4 MHz, determined from the experiment. Superimposed on the polar plot is a model showing water bound to the complex. The inset shows the schematic representation of the geometry of Mn(III) and Mn(IV),and a water proton. Reprinted from Ref. [318] with permission. Copyright 1997 American Chemical Society.

The compound $[(bisimMe_2en_2)_2Mn^{III}Mn^{IV}(\mu\text{-}O)_2](ClO_4)_3H_2O$ was synthesized and studied by EPR and ESEEM [319]. Low-frequency ^{14}N-modulations, resolved by ESEEM, in frozen aqueous solution of the complex were tentatively assigned to directly coordinated nitrogens on the Mn^{III} ion [319], although an alternative assignment, i.e. coordination to remote nitrogens of the imidazole, was not excluded. Noticeably no 'matrix' proton peak, expected at ~ 15 MHz, was resolved indicating that even in aqueous media the Mn^{III}–Mn^{II} core is isolated from the solvent. The complex is characterized by a 16-line 'multiline' EPR signal, typical of Mn^{III}–Mn^{II} ($S = 1/2$) complexes [316]. Upon UV-irradiation of the complex in aqueous borate buffer (pH 10) at 77 K, a new EPR signal, attributed to the, weak, magnetic interaction between an imidazole radical coupled to the Mn^{III}–Mn^{II} pair was formed. ESEEM spectra at magnetic field corresponding to manganese resonances indicate that that the coordination environment of the Mn^{III}–Mn^{II} pair is not modified upon UV-irradiation [319].

6.6.4.1. Catalase. Catalase enzymes promote the catalytic disproportionation of hydrogen peroxide, a toxic molecule produced by aerobic metabolism in all aerobic cells, to water and molecular oxygen. Superoxidized catalase has an isolated ground $S = 1/2$ state which is characterized by a 16-line EPR spectrum and is believed to contain an isolated (μ-oxo)$_2$(μ-carboxylato)-bridged Mn(III)Mn(IV)$_2$ core [321].

ESEEM investigation of the superoxidized Mn(III)Mn(IV) enzyme of *Thermus thermophilus* by two groups [320,322], revealed nitrogen modulations assigned to one ^{14}N atom. In the early work [322] this coupling ($e^2qQ/h = 2.44$ MHz, $\eta = 0.44$, $A_{iso} = 2.3$ MHz) was assigned to the remote nitrogen of a histidine. In the recent work [320], similar ^{14}N couplings were found ($e^2qQ/h = 2.34$ MHz, $\eta = 0.51$, $A_{iso} = 2.45$ MHz), but the assignment was different. This was based on ESEEM experiments in enzymes where reductive methylation treatment resulted in methylation of 64% of the lysine residues but only 3% of the histidines. The ESEEM is profoundly modified by the methylation treatment, changing from $A_{iso} = 2.45$ MHz to a larger value; taking into account analysis of the changes in the amino-acid composition of the enzyme that is induced by the reductive methylation, it was proposed that the coupled ^{14}N belongs to the ε-amino group of a lysine residue bridging the two metal ions in Mn(III)Mn(IV) catalase [320]. The assignment to a directly coordinated nitrogen is corroborated by ESEEM data in model compounds [126,320] and more recent ESEEM data on the Mn(III)Mn(IV) catalase from *Lactobacillus plantarum* [67]. However, in Ref. [67], the observed ^{14}N coupling ($e^2qQ/h = 2.29$ MHz, $\eta = 0.58$, $A_{iso} = 2.88$ MHz), was assigned to the coordinated nitrogen of a histidine. This was based on the quadrupole coupling parameters and EXAFS data, which suggested histidine coordination to the binuclear cluster [67]. Cyanide or azide binding altered this nitrogen coupling, but without binding to the manganese cluster. Instead, it was suggested that azide binds to a protein-derived site, causing indirect perturbations in the Mn_2(μ-oxo)$_2$ geometry, e.g. a slight flattening of the Mn_2 core [67].

In Ref. [320], $^{14}NH_4Cl$ binding to Mn(III)Mn(IV) resulted in a spectrum, resembling the ESEEM pattern for the ammonia inhibited S_2-state of the man-

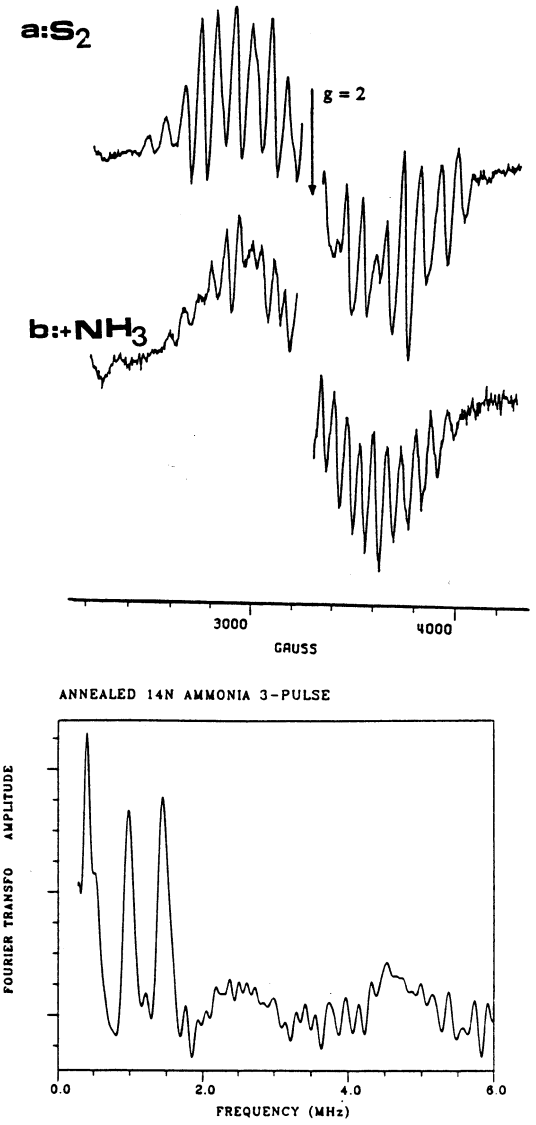

Fig. 45. (a) S2 multiline EPR signal from the Mn cluster of Photosystem II, obtained after illumination at 200 K. (b) The modified multiline EPR signal seen after treatment with ammonia. The three-pulse ESEEM spectrum ($T = 4.2$ K, $H = 3500$ G, 9.246 GHz, $\tau = 200$ ns) of for the $\ll$ anealed $\gg$ $^{14}NH_4Cl$-treated sample. Reprinted from Ref. [323] with permission. Copyright 1989 American Chemical Society.

ganese cluster of Photosystem II, see Fig. 45. Based on this similarity, it was proposed that in catalase, like in Photosystem II, the ^{14}N atom of ammonia bridges the two Mn ions in the Mn(III)Mn(IV) complex [320].

6.6.4.2. Manganese cluster of Photosystem II. Photosystem II (Photosystem II) couples photooxidation of the primary chlorophyll species P_{680} to the cyclic oxidation of H_2O to molecular oxygen [317]. The water oxidation chemistry occurs in an OEC consisting of a tetranuclear manganese cluster and a redox-active tyrosine, with Y_Z as an essential cofactor [317]. The OEC and also most of the other cofactors of Photosystem II have been intensively studied by ESEEM. For example, the stable tyrosine Y_D [149,324,325], the tyrosine Y_Z, [325] the intermediate electron acceptor pheophytin [86] and the semiquinone of the iron–quinone complex [66,326–328]. The oxygen evolution cycle involves five 'S' states, S_0–S_4, where the subscript refers to the number of electron equivalents removed from the OEC, referenced to the most reduced state S_0 [317,329].

6.6.4.3. ESEEM on the S_2 state. Of the various S states, S_2 is the most extensively studied one, based on the characteristic 'multiline' signal at $g = 2$, see Fig. 45(a), and alternative EPR signals at $g \sim 4$ [317]. The first ESEEM study of the $g = 2$ 'multiline' EPR signal from the S_2-state, using Photosystem II membranes from spinach, revealed a broad structured peak centered at ~ 5 MHz [323].

ESEEM experiments on ^{14}N- and ^{15}N-labeled Photosystem II from cyanobacteria [141] and spinach [142] proved that this peak is due to ^{14}N coupling to the manganese cluster with a hyperfine coupling of $A_{iso} \sim 5$ MHz. Whether this nitrogen is ligated or simply close to the manganese cluster remains to be clarified. Definitive assignment of this nitrogen coupling to an imidazole was provided by ESEEM data on Photosystem II from cyanobacterium *Synechosystic* PCC 6803 selectively labeled with ^{15}N at the two nitrogen sites of the imidazole side-chain of all the histidine residues [140]. Recently, ESEEM experiments were performed for the S_2 signal in lyophilized Photosystem II resuspended in $H_2^{17}O$ [129]. Modulations at the ^{17}O Larmor frequency were resolved but they were assigned to paramagnetic centers different from the manganese cluster. The absence of a detectable ^{17}O effect was considered by the authors as evidence that, in the S_2 state, oxygen does not interact with the manganese species responsible for the multiline signal [129]. The Cl^- ion is an essential cofactor of the OEC in Photosystem II. In an effort to examine possible binding of Cl^- at or near the manganese cluster, ESEEM experiments were performed for salt-washed Photosystem II reconstituted with either $CaCl_2$ or $CaBr_2$ [330]. Division of the time-domain ESEEM data for Cl^- versus Br^- treated Photosystem II resulted in a spectrum containing peaks at the Larmor frequencies of chloride and bromide. These features were absent in EGTA- or sulfate-treated Photosystem II reconstituted with either $CaCl_2$ or $CaBr_2$. These findings were interpreted as possible evidence for the existence of an exchangeable chloride site in the vicinity of the manganese cluster.

Recently, the interaction between various ^2H-labeled alcohols and the manganese-cluster of Photosystem II was examined by ESEEM [331,332]. Modulations due to deuterons from methanol were resolved in the S_2 [331,332], as well as in the S_0 and S_1 states [331]. Detailed analysis of the ESEEM data lead to the conclusion that small alcohols, e.g. ethanol, methanol, are directly ligated, e.g. one molecule of alcohol, to the manganese cluster in the S_2 state [332]. Evidence for the limited

access of *n*-propanol was found, but no evidence for 2-propanol or DMSO access was uncovered. Specifically, for methanol the maximal Mn–H distances were estimated to be in the range 3.7–5.6 Å (assuming a dimer-of-dimers configuration for the $(Mn)_4$ cluster) or 3.6–4.9Å (for a symmetric-cubane structure) [332].

6.6.4.4. Modified S_2 multiline signals. A number of biochemical treatments lead to the formation of an S_2 state characterized by multiline EPR signals with distinctly altered multiline patterns [142,317,333]. Cases of modified S_2 signals, which have been studied by ESEEM, include Ca^{2+}-depleted Photosystem II followed by EGTA or pyrophosphate treatment [142] or NH_3-treated Photosystem II [323], see Fig. 45(b).

NH_3 binds reversibly at the OEC; comparative ESEEM experiments on a modified multiline S_2 signal generated in Photosystem II membranes treated with either $^{14}NH_4Cl$ or $^{15}NH_4Cl$ revealed a nitrogen coupling ($A_{iso} = 2.29$ MHz, $e^2qQ/h = 1.61$ MHz, $\eta = 0.59$ for ^{14}N), see Fig. 45. These data show that a NH_3-derived ligand binds to the manganese cluster of Photosystem II during the S_1 to S_2 transition [323]. Based on the nuclear quadrupole coupling parameters it was postulated that this NH_3-derived ligand is an amine (NH_2) bridge between metal ions which is derived via a mechanism which involves deprotonation of NH_3 by the manganese cluster in the S_2 state.

In Ca^{2+}-depleted/EGTA treated Photosystem II, nitrogen modulations were detected by ESEEM in ^{14}N- and ^{15}N-labelled Photosystem II [142]. The ESEEM pattern observed in Ca^{2+}-depleted/pyrophosphate-treated Photosystem II was strikingly similar to that of a UV-generated imidazole radical. Based on this it was postulated that a histidine is also responsible for the modulations in the pyrophosphate-treated Photosystem II. A peak at 4.1 MHz in the ESEEM spectrum of Ca^{2+}-depleted/EGTA-treated Photosystem II was considered to be due to a slightly modified coupling of the nitrogen seen in normal S_2, i.e. from the histidine [140]. This was taken as evidence that calcium depletion and/or EGTA treatment alters this, histidine, coupling to the Mn cluster. Comparison of ESEEM for EGTA versus pyrophosphate treated Photosystem II, after Ca^{2+}-depletion, showed that EGTA is responsible for modulations, which give rise to a peak at 3.5 MHz indicating that EGTA binds to or near to the Mn cluster.

ESEEM has been applied on a new multiline signal from the OEC, originating from a Mn(II)–Mn(III) ($S = 1/2$) state, generated by incubation of Photosystem II with nitric oxide (NO) at -30°C [334]. The ESEEM data recorded on ^{14}NO- and ^{15}NO-treated Photosystem II showed weak ^{15}N modulations from distant NO molecules. Together with pulsed ENDOR data, this was taken as evidence that the NO-induced EPR signal is due to a reducing effect, instead of ligation, of NO onto the Mn-cluster [334].

A distinct multiline signal can be detected in the S_0-state, but only in the presence of methanol [335,336]. ESEEM and HYSCORE spectroscopy on the S_0-state in the presence of deuterated methanol revealed specific methanol modulations in the vicinity of the Mn-cluster [331], characterized by ^2H-dipolar coupling of ~ 0.5 MHz.

6.6.4.5. ESEEM on the split-S_3 signal. Upon illuminating the Ca^{2+}-depleted Photosystem II in the S_2 state, a broad derivative EPR signal with a splitting of 130–160 G centered at $g = 2$ appears [142].This signal has been called the 'split S_3-state signal' although it has not been clearly correlated with the normal S_3 state, since the latter is not detectable by EPR in untreated Photosystem II. Similar 'split-S_3 signals' had been observed in Cl-depleted, NH_4Cl-treated and acetate-treated Photosystem II Fig. 46, see Ref. [317] and references therein, although the g-value and the widths of the signals depend on the specific treatment.

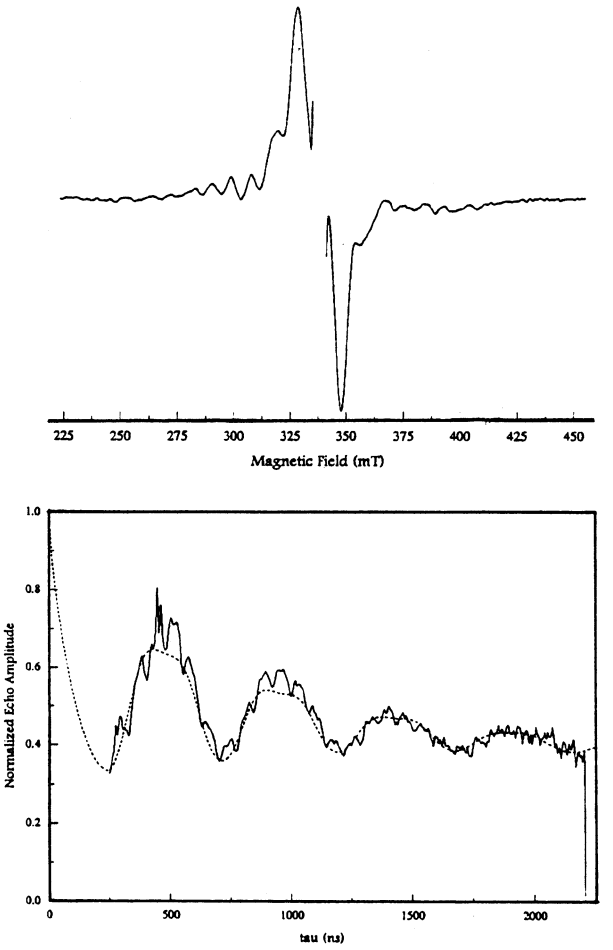

Fig. 46. (Top): Light minus-annealed 'split-S3' EPR spectrum of acetate-treated Photosystem II reaction center cores. (Bottom) Experimental (solid line) and simulated (dashed line) two-pulse ESEEM recorded at $H = 3200$ G, ($T = 1.8$ K, 8.82 GHz). Simulation parameters ($S = 1/2$, $I = 1$, ^{2}H nucleus): $A_{iso} = 0$ MHz, $T_{dip} = 0.42$ MHz. Reprinted from Ref. [105] with permission. Copyright 1998 American Chemical Society.

Although the assignment of the signal to a radical broadened by magnetic interactions with the manganese is generally accepted, the molecular origin of this radical has been intensively debated, with possibilities including oxidizing histidine [337,338] or the redox-active tyrosine Y_Z [339,340]. ESEEM data on the split S_3 signal in Ca^{2+}-depleted pyrophosphate-treated Photosystem II contained modulations at $\sim$ 6 MHz, probably from the ^{31}P nucleus of pyrophosphate [142]. Nitrogen modulations observed in this split-S_3 signal, were similar to those seen in the modified S_2 state and this indicates that nitrogen coupling is not altered in the S_3 state compared to the S_2 state in Ca^{2+}-depleted Photosystem II [142]. More recently, ESEEM data for the split S_3 signal were obtained from acetate-treated *Synechocystis*-Photosystem II core complexes containing either protonated or deuterated tyrosine (d_7-Tyr) [340]. The ratio of ^2H- by ^1H-ESEEM data contained ^2H modulations similar to those seen in the ESEEM spectra of deuterated Y_Z. This was interpreted as evidence that the radical responsible for the split S_3 signal in acetate-treated Photosystem II is the tyrosine Y_Z radical interacting with the S_2 state of the Mn cluster, e.g. a $S_2Y_Z^o$ state [340]. Based on this assignment the split signal was used as a paramagnetic-probe to study the proximity of deuterons into the vicinity of Y_Z. ESEEM data were recorded for the split-signal in acetate-treated [105,341] or Ca^{2+}-depleted [342] Photosystem II in H_2O-enridhed buffer. In all cases, modulations from weakly coupled deuterons ($A_{iso} \sim 0$) were resolved. In acetate-treated Photosystem II [341], simulation of the time-domain ESEEM by two deuteron couplings with an average $T_{dip} = 0.57$ MHz, led to the conclusion that Y_Z trapped in the split signal form participates in two hydrogen bonds [341]. Different conclusions were drawn in Ref. [105], where the ESEEM data in acetate-treated Photosystem II, see Fig. 46, required four deuteron couplings, with $T_{dip} =$ 0.42 MHz. The disagreement between the two groups, may be due to the inappropriateness of the formulation for $S = 1/2$, $I = 1$ used to analyze the ESEEM spectra for the split signal which probably has $S = 1$ character [105]. In Ca^{2+}-depleted Photosystem II, two deuterium nuclei ($T_{dip} = 0.48$ MHz) were needed to fit ESEEM data for the split-signal [342]. The two proximal deuterons were considered to correspond to a bifurcated hydrogen bond [342]; one of the hydrogen bond donors to Y_Z in Ca^{2+}-depleted Photosystem II was assigned to D1-His-190 while the second to either H_2O ligated to the manganese-cluster or an endogenous protein donor [342].

In Ref. [341] a 0.117 MHz dipolar interaction was estimated by fitting time-domain ESEEM data for the split signal in methyl-deuterated acetate treated Photosystem II. This dipolar coupling was modeled with a 3.1 Å distance between a ^2H from an acetate methyl group and the phenoxy oxygen of Y_Z [341].

6.7. Nickel

6.7.1. Synthetic nickel compounds

Two-pulse [344] and four-pulse [36] ESEEM studies at the X-band, aimed at measuring the superhyperfine coupling between protons of axially bound H_2O molecules and the nickel ion in $Ni^{3+}(CN)_4(H_20)^{2-}$. The shifts observed for the ^1H

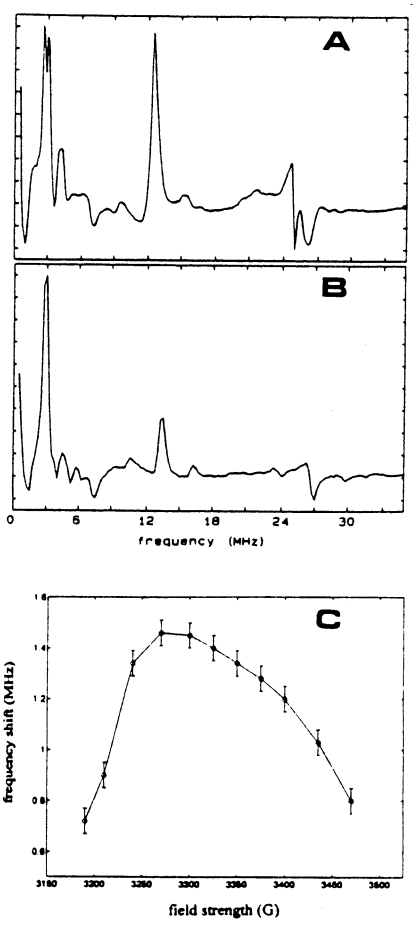

Fig. 47. Two-pulse ESEEM spectra (A) for $Ni^{3+}(CN)_4(H_2O)_2$ collected at $g = 2.17$, and (B) for $Ni^{3+}(CN)_4(py)_2$ collected at $g = 2.11$. (C) Plot of the shift in the ^1H sum-combination line from twice the ^1H Larmor frequency across the EPR spectrum, for $Ni^{3+}(CN)_4(H_2O)_2$. Shifts were measured from the peak maxima of the two-pulse ESEEM spectra. The profile of such a plot is informative about the relative geometrical arrangement of the water protons relative to the g-tensor of the complex. Reprinted from Ref. [36] with permission. Copyright 1994 American Chemical Society.

sum-combination line were found to vary between 0.1–1.8 MHz in aqueous solution Fig. 47(A), but were absent in pyridine solution, see Fig. 47(B). The profile of the shift versus the magnetic field strength across the EPR line, see Fig. 47(C), is characteristic of the Ni–H distance, the orientation of the principal axis of the hyperfine coupling tensor with respect to the g-tensor [344].

The axial proton's hyperfine coupling as determined from the four-pulse ESEEM are $|A_{iso}| = 2.5 \pm 0.5$ MHz, $r_{eff(Ni-H)} = 2.33 \pm 0.03$ Å and $\theta_n = 18 \pm 3°$ [36]. These results, determined by four-pulse ESEEM, are more accurate then those determined by two-pulse ESEEM, which gave $|A_{iso}| < 4$ MHz, $r_{eff(Ni-H)} = 2.4 \pm 0.1$ Å and

$\theta_n = 12 \pm 5°$ [344], due to the inherent lower resolution of the two-pulse ESEEM experiment as compared to the four-pulse experiment [36].

X-band ESEEM in combination with Q-band pulsed ENDOR was applied to study the electronic structure of the ligands of [Bis(maleinitriledithilato)nickel]$^-$ [Ni(mnt)$_2$]$^-$ [345]. ^{14}N-ESEEM allowed the resolution of coupling tensors ($\boldsymbol{A}$ = [0.13, 0.10, 0.94 MHz], $e^2qQ/h = 3.9$ MHz, $\eta = 0.15$) of the nitrogens from the four CN$^-$, while ENDOR data on ^{13}C labeled compounds allowed the resolution of the couplings for ^{13}C1 ($\boldsymbol{A}$ = [4.6, 4.6, -3.0 MHz]) and ^{13}C2 ($\boldsymbol{A}$ = [2.6, 2.6, 3.4 MHz]) which correspond to p_z spin-densities on the carbons of the order 0.025–0.028. When the cyanides are replaced by fluorines the spin density, delocalized on the ^{19}F$^-$ atoms, is severely reduced, e.g. from 0.028 for the carbon of CN$^-$ to $\sim 4 \times 10^{-5}$ for ^{19}F$^-$ [345]. Based on these spectroscopic data and molecular orbital calculations, a significant fraction of the unpaired spin density $\sim 60\%$ is found to be delocalized on the four sulfur ligands, and only $\sim 25\%$ remains on the Ni orbitals [345]. This can be contrasted to an analogous study of the copper compound of (mnt), i.e. [Cu(mnt)$_2$]$^-$, where only small amounts of the σ delocalization through bond polarization occurs. The significant π delocalization on the 3p-π orbitals of S and the 2p-π orbitals of C found in [Ni(mnt)$_2$]$^-$ supports the notion that the S-donor atoms are intimately involved in the oxidative chemistry associated with Ni sites in hydrogenases and other enzymes with cystein ligation of Ni.

6.7.2. Nickel proteins

6.7.2.1. Hydrogenase. ESEEM data on the Ni–Fe hydrogenase [343] from *Desulfovibrio gigas* in H_2O versus D_2O buffer showed that the nickel site was inaccessible to solvent unless the protein was in its active Ni–C form [346]. The ESEEM spectrum recorded at the Ni resonance $g = 2.22$ of hydrogenase, from *Thiocapsa roseopersicina* reveals nitrogen modulations whose coupling is close to the cancellation condition ~ 2 MHz, probably from an imidazole [346]. Comparative ESEEM studies revealed the existence of a histidine ($A_{iso} = 1.8$ MHz, $e^2qQ/h = 1.68$ MHz, $\eta = 0.48$) coupled to the Ni center of F_{420}-reducing hydrogenase [347,348] whereas this interaction is absent in the methylviologen-reducing hydrogenase [347,348].

6.8. Ti^{3+} ($S = 1/2$)

The trivalent titanium ion, Ti^{3+}, has been frequently cited as a good example for highlighting the crystal-field or ligand-field theory [2], since it is one of the simplest paramagnetic metal ions. Typically Ti^{3+} complexes exhibit almost axial EPR spectra with the axial g-tensor being sensitive to the covalency between the metal and the ligands. Recently, based on an ESEEM study of the hydrated Ti^{3+} ion in the amorphous solid of a 2-propanol/D_2O [349], the hydration structure of the Ti^{3+} ion was inferred. The ESEEM spectra contained only weak ^{1}H or ^{2}D nuclear modulations and their analysis concerned the time-domain signal only. It was found that the hydrated ion in D_{3d} symmetry with the unpaired electron being localized

mainly on the d_{z^2} metal orbital. Because of the strong repulsive interaction of the d_{z^2} orbital and the n_π orbitals of the coordinated D_2O molecules the D–O–D planes are almost parallel to the C_3 axis of the complex [349]. The Ti–O distance was estimated to be ~ 2.2 Å while the angle between the C_3 axis and the Ti–O bond was found to be 60°.

6.9. ESEEM of non-Kramer doublets

The theory of the ESEEM of integer spin systems, see Section 3.7, was applied for direct interpretation of ESEEM data for various diferrous carboxylate bridged non-heme iron proteins, including diferrous methane monooxygen hydroxylases ($MMOH_{red}$) form *Methyloccocus capsulatus* and *Methylosinus trichosporium OB3b* and azido-hemerythrin ($N3H_{red}$) [117], N3-ribonucleotide reductase ($N3R2_{red}$), N3-rubrerythyrin ($N3R_{red}$) and N3-≪chopped≫rubrerythrin ($N3CR_{red}$) which lacks the 39-residue C-terminal FeS_4 domain [118]. The ESEEM experiments were performed at sub-liquid He temperatures $T = 2$ K, in the limit where the external magnetic field (B_0) oriented parallel to the microwave field is small, $B_0 \leq 20$ G [117,118], see Fig. 48. These experiments yielded the ^{14}N-quadrupole tensors very accurately, as well as estimates of hyperfine couplings for nitrogen nuclei from coordinated histidines and from azides. In addition the orientation of the cluster z-axis relative to the histidyl was also obtained, Fig. 49. It is emphasized that the observed ESEEM arises from the coordinated ^{14}N nuclei [118], and this has to be contrasted with the case of the ESEEM of half-integer systems like Fe^{3+} and Cu^{2+}, where it is the non-coordinated nitrogen which is detected by ESEEM at the X-band [7].

For $^{14}N(I = 1)$ nuclei coupled to a non-Kramer spin doublets at a low magnetic field, the pure quadrupole frequencies, relations 21 ($\nu^0 = 2K\eta$, $\nu^- = K(3 - \eta)$, $\nu^+ = K(3 + \eta)$), are predicted to characterize the ESEEM spectrum [118]. The perturbation theory predicts that, at low magnetic fields, the intensities depend explicitly on the orientation of the z-axis, e.g. the direction of the zero-field splitting tensor of the complex, relative to the quadrupole tensor, see Fig. 48(A). In the limit where z is along one (k) quadrupole-axis direction, only the (ij) transition (where $i, j, k = 1, 2, 3$ label the ^{14}N quadrupole levels, and $\nu^+ = \nu_{13}$, $\nu^- = \nu_{12}$, $\nu^0 = \nu_{23}$) appears in the ESEEM spectrum, see Fig. 48(B,C). Accordingly, the relative intensities of the $^{14}N(I = 1)$ transitions for the bound imidazole have been used to determine the orientation of the z-axis of the non-Kramer metal centers relative to the molecular framework of the imidazole plane [118].

A striking finding for $MMOH_{red}$, $R2_{red}$, R_{ox} is that the cluster z-axis appears to take a well-defined orientation relative to the coordinated histidine, Fig. 49. The z-axes were found to lie approximately along the normal plane of the histidine ligand in $N_3Rr(CRred)_{red}$, but roughly along the Fe–N bonds in $MMOH_{red}$. For N_3R2_{red} they take an intermediate orientation, lying in the planes defined by the Fe–N bonds and the histidine normals. This analysis of the ESEEM data for diferrous clusters supports the idea that the direction of the tetragonal zero-field splitting axis of a histidine-bound ferrous ion is fixed by His-Fe bonding. Moreover,

the histidines not only provide a structural framework for the cluster but also play a key-role in determining the electronic state of the O_2-activating diferous state [118]. Thus, the ESEEM spectra on non-Kramer centers provides an important

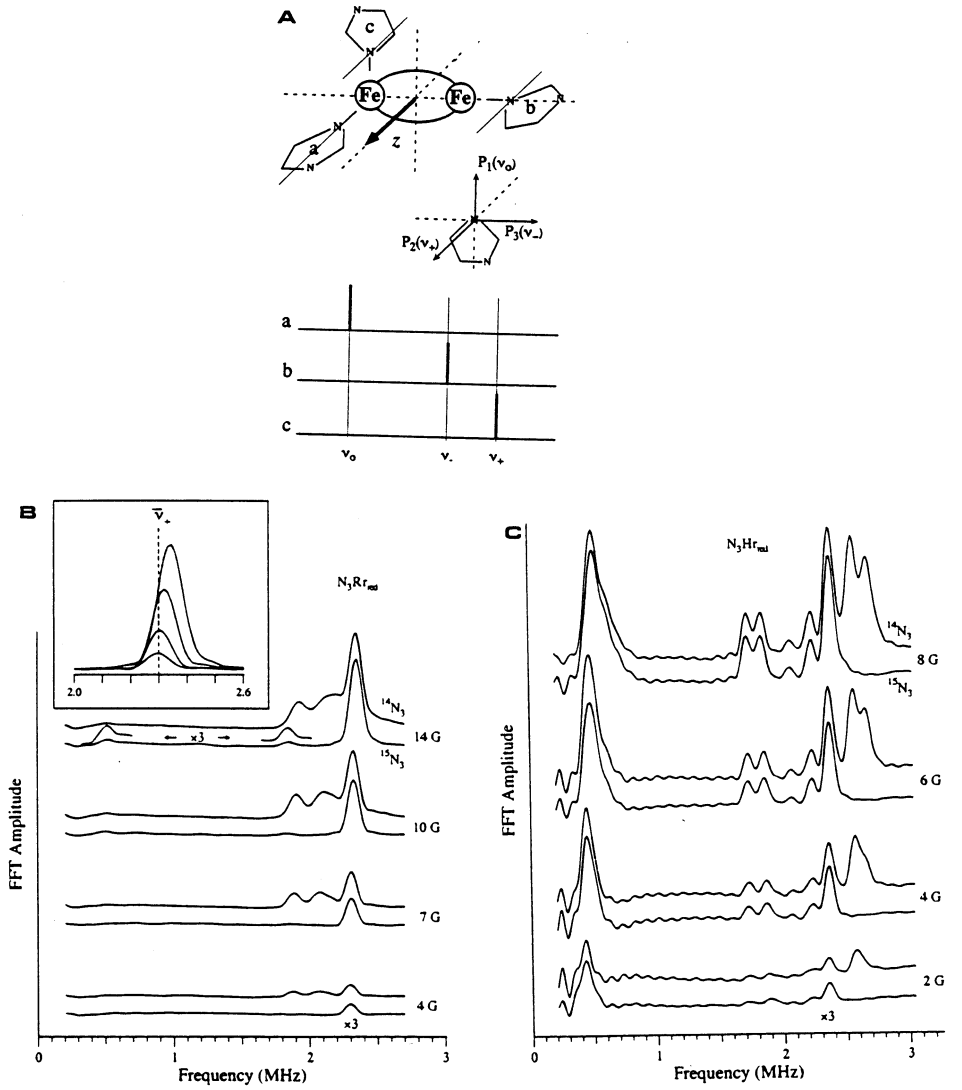

Fig. 48. (A) Orientation of the ^{14}N quadruple axes relative to the histidyl plane (center). Parentheses give the transition observed when B_0 is along that axis. Schematic representation of the diferrous center with three orthogonal histidyl ligands (top) and idealized zero field non-Kramer ESEEM spectra for the three ^{14}N ligands (bottom). (B,C) Three-pulse ESEEM spectra of N_3R_{red} and N_3H_{red}. Upper and lower traces at each value of B_0 are obtained from protein treated with $^{14}N_3^-$ and $^{15}N_3^-$, respectively. (B) $^{14/15}N_3$ R_{red} (inset: expanded view of the v^+ nuclear transition). (C) $^{14/15}N_3H_{red}$. Reprinted from Ref. [118] with permission. Copyright 1997 American Chemical Society.

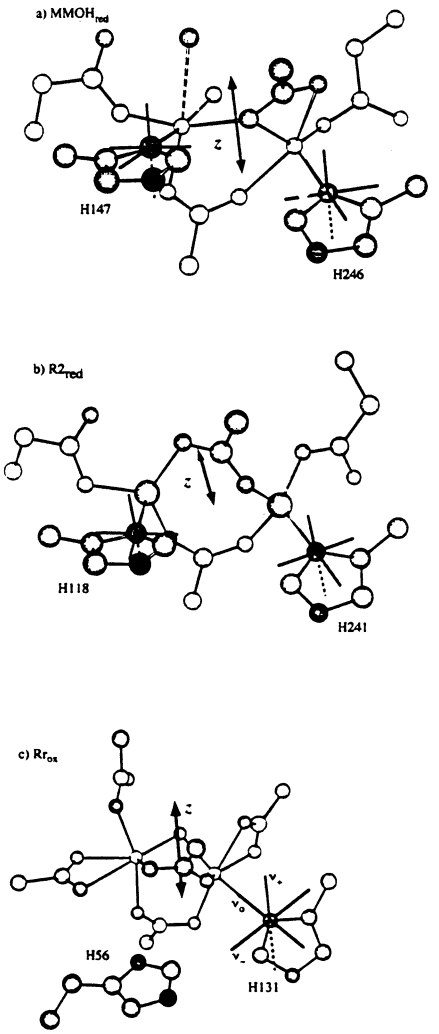

Fig. 49. ^{14}N quadruple axes and proposed cluster z axes superimposed on structures of protein bound diiron clusters. Reprinted from Ref. [118] with permission. Copyright 1997 American Chemical Society.

complement to UV–vis and magnetic circular dichromizim which allow estimation of the magnitude of the crystal-field splitting but not their orientations [350].

7. Conclusions

ESEEM is now established as a high-resolution pulsed-EPR technique and is currently used as a standard tool for the study of paramagnetic centers. ESEEM spectroscopy can allow the identification of ligands, counting their number, deter-

mination of their relative geometrical disposition with respect to the metal coordinates and investigation of the distribution of the molecular orbital over the complex. Most of the existing spectrometers operate at the X-band, and this limits the interactions amenable to study by ESEEM to a certain range. With the advent of the high-frequency high-field pulsed EPR spectrometers, this window is expected to be extended to cover stronger coupling regimes and will also allow orientation selective ESEEM to performed on narrow EPR signals, like those for radicals. The power of the excitation/detection schemes now available is considerable and together with the two-dimensional techniques, it is expected that their application will contribute significantly to the study of metal centers and other paramagnetic systems.

References

[1] A. Abragam, B. Bleaney, Electron Paramagnetic Resonance of Transition Metal Ions, Clarendon Press, Oxford, 1970.
[2] J.R. Pilbrow, EPR of Transition Metal Ions, Clarendon Press, Oxford, 1990.
[3] W.B. Mims, in: S. Geshwind (Ed.), Electron Paramagnetic Resonance, Plenum Press, New York, 1972, pp. 263–285.
[4] G. Feher, Phys. Rev. 103 (1956) 834.
[5] L. Kevan, L.D. Kispert, Electron Nuclear Double Resonance Spectroscopy, Wiley, New York, 1976.
[6] L.G. Rowan, E.L. Hahn, W.B. Mims, Phys. Rev. 137 (1965) 61.
[7] S.A. Dikanov, Y.D. Tsvetkov, Electron Spin Echo Envelope Modulation (ESEEM) Spectroscopy, CRC Press, Boca Raton, FL, 1992.
[8] A.V. Astashkin, S.A. Dikanov, Y.D. Tsvetkov, Chem. Phys. Lett. 122 (1985) 259.
[9] E.J. Reijerse, C.P. Keijers, J. Magn. Res. 71 (1987) 83.
[10] H. Thomann, M. Bernardo, in: L.J. Berliner, J. Reuben (Eds.), Biological Magnetic Resonance, Plenum Press, New York, 1993, pp. 275–322.
[11] (a) W.B. Mims, Phys. Rev. B 5 (1972) 2409. (b) W.B. Mims, Phys. Rev. B 6 (1972) 3543.
[12] L. Kevan, R.N. Schwartz, Time Domain Electron Spin Resonance, Wiley, New York, 1979.
[13] M.K. Bowman, R.J. Massoth, C.S. Yannoni, in: D.M.S. Baguley (Ed.), Pulsed Magnetic Resonance: NMR, ESR, Optics, Oxford Science, New York, 1992, pp. 423–445.
[14] O. Burghaus, M.P. Klein, Chem. Phys. Lett. 243 (1995) 486.
[15] A. Grüpp, M. Mehring, in: L. Kevan, M.K. Bowman (Eds.), Modern Pulsed and Continuos Wave Electron Spin Resonance, Wiley, New York, 1990, pp. 195–230.
[16] C. Gemberle, A. Schweiger, Chem. Rev. 91 (1991) 1481.
[17] P.E. Doan, B.M. Hoffman, Chem. Phys. Lett. 269 (1997) 208.
[18] A. Schweiger, Angew. Chem. Int. Ed. Engl. 30 (1991) 265.
[19] A. Schweiger, in: L. Kevan, M.K. Bowman (Eds.), Modern Pulsed and Continuous Wave Electron Spin Resonance, Wiley, New York, 1990 (Chapter 2).
[20] S.A. Dikanov, A.V. Astashkin, in: A.J. Hoff (Ed.), Advanced EPR: Applications in Biology and Biochemistry, Elsevier, Amsterdam, 1989, pp. 59–115.
[21] C.P. Keijers, E.J. Reijerse, J. Schmidt (Eds.), Pulsed EPR: A New Field of Applications, North-Holland, Amsterdam, 1989.
[22] L. Kevan, M.K. Bowman, Modern Pulsed and Continuos Wave Electron Spin Resonance, Wiley, New York, 1990.
[23] Y.D. Tsvetkov, S.A. Dikanov, in: H. Singel (Ed.), Metal Ions in Biological Systems, vol. 22, Marcel Dekker, New York, 1987, pp. 207–263.

[24] W.B. Mims, J. Peisach, in: L.J. Berliner, J. Reuben (Eds.), Biological Magnetic Resonance, Plenum Press, New York, 1981, pp. 213–263.
[25] W.B. Mims, J. Peisach, in: A.J. Hoff (Ed.), Advanced EPR: Applications Biology and Biochemistry, Elsevier, Amsterdam, 1989, pp. 1–57.
[26] L. Kevan, Acc. Chem. Res. 20 (1987) 1.
[27] S.A. Dikanov, Y.D. Tsvetkov, Electron Spin Echo Envelope Modulation (ESEEM) Spectroscopy, CRC Press, Boca Raton, FL, 1992 (Chapter 16).
[28] L. Kevan, Isr. J. Chem. 29 (1989) 21.
[29] E.L. Hahn, Phys. Rev. 80 (1950) 580.
[30] C.A. Hutchison, D.B. McCay, J. Chem. Phys. 66 (1977) 3311.
[31] A.M. Raitsimring, P. Borbat, T.K. Shokhireva, F.A. Walker, J. Phys. Chem. 100 (1996) 5235.
[32] C. Gemberle, G. Aebli, A. Schweiger, R.R. Ernst, J. Magn. Res. 88 (1990) 241.
[33] A.M. Tyryshkin, S.A. Dikanov, D. Goldfarb, J. Magn. Res. A 105 (1993) 271.
[34] A.M. Tyryshkin, S.A. Dikanov, R.G. Evelo, A.J. Hoff, J. Chem. Phys. 97 (1992) 42.
[35] K. Matar, D. Goldfarb, J. Magn. Res. A111 (1994) 50.
[36] H-I. Lee, J. McCracken, J. Phys. Chem. 98 (1994) 12861.
[37] S. Van doorslaer, A. Schweiger, Chem. Phys. Lett. 281 (1997) 297.
[38] P. Höfer, A. Grupp, H. Nedenführ, M. Mehring, Chem. Phys. Lett. 132 (1986) 279.
[39] A. Schweiger, Appl. Magn. Res. 5 (1993) 229.
[40] G. Jeschke, R. Rakhmatullin, A. Schweiger, J. Magn. Res. 131 (1998) 261].
[41] M. Hubrich, G. Jeschke, A. Schweiger, J. Chem. Phys. 104 (1996) 2172.
[42] R. Song, Y.C. Zhong, C.J. Noble, J.R. Pilbrow, D.R. Hutton, J. Magn. Res. A 117 (1995).
[43] R. Song, Y.C. Zhong, C.J. Noble, J.R. Pilbrow, D.R. Hutton, Chem. Phys. Lett. 237 (1995) 86.
[44] R. Song, J. Chem. Phys. 105 (1996) 9046.
[45] E. Hoffmann, A. Schweiger, Chem. Phys. Lett. 220 (1994) 467.
[46] E.J. Hustedt, A. Schweiger, R.R. Ernst, J. Chem. Phys. 96 (1992) 4954.
[47] J. Sebbach, E. Hoffmann, A. Schweiger, J. Magn. Res. A116 (1995) 221.
[48] R.P.J. Merks, R.J. de Beer, J. Magn. Res. 37 (1980) 305.
[49] P. Höfer, J. Magn. Res. A 111 (1995) 77.
[50] W.B. Mims, J. Magn. Res. 59 (1984) 291.
[51] M. Fauth, A. Schweiger, L. Braunsweiler, J. Forrer, R.R. Ernst, J. Magn. Res. 66 (1986) 74.
[52] H. Cho, S. Pfenninger, C. Gemberle, A. Schweiger, R.R. Ernst, Chem. Phys. Lett. 160 (1989) 391.
[53] A. Ponti, A. Schweiger, J. Chem. Phys. 102 (1995) 5207.
[54] R. Szosenfogel, D. Goldfarb, Mol. Phys. 95 (1998) 1295.
[55] R.P.J. Merks, R.J. de Beer, J. Phys. Chem. 83 (1979) 3319.
[56] D. Van Ormont, K. Nederveen, Chem. Phys. Lett. 82 (1981) 443.
[57] P.A. Narayana, L. Kevan, Magn. Res. Rev. 7 (1983) 239.
[58] W.B. Mims, J.L. Davis, J. Peisach, J. Magn. Res. 86 (1990) 273.
[59] A. Ponti, J. Magn. Res. 130 (1997) 84.
[60] K. Warnke, J. McCracken, J. Chem. Phys. 103 (1995) 6829.
[61] A. Raitsimring, F.A. Walker, J. Am. Chem. Soc. 120 (1998) 991.
[62] L. Kevan, M.K. Bowman, P.A. Narayana, R.K. Boeckman, V.F. Yudanov, Yu.D. Tsvetkov, J. Chem. Phys. 63 (1975) 409.
[63] A.V. Astashkin, Yu.D. Tsvetkov, Appl. Magn. Res. 6 (1994) 411.
[64] E.J. Reijerse, S.A. Dikanov, J. Chem. Phys. 95 (1991) 836.
[65] G. Gerfen, P. Hanna, N.D. Chasteen, D.J. Singel, J. Am. Chem. Soc. 113 (1991) 9513.
[66] Y. Deligiannakis, A. Boussac, A.W. Rutherford, Biochemistry 34 (1995) 16030.
[67] T.L. Stemler, B.E. Sturgeon, D.W. Randall, R.D. Britt, J.E. Penner-Hahn, J. Am. Chem. Soc. 119 (1997) 9215.
[68] S.A. Dikanov, A.M. Tyryshkin, J. Hüttermann, R. Bogumil, H. Witzel, J. Am. Chem. Soc. 117 (1995) 4976.
[69] S. Dikanov, I. Felli, M.-S. Viezzoli, A. Spoyalov, J. Hüttermann, FEBS Lett. 345 (1994) 55.
[70] S. Cosgrove-Larsen, D.J. Singel, J. Phys. Chem. 96 (1992) 9007.
[71] S. Cosgrove-Larsen, D.J. Singel, J. Phys. Chem. 96 (1992) 10594.

[72] S.A. Dikanov, A.A. Shubin, V.N. Parmon, J. Magn. Res. 42 (1981) 474.
[73] M. Romanelli, D. Goldfarb, L. Kevan, Mag. Res. Rev. 13 (1988) 262.
[74] H.J. Flanagan, D.J. Singel, J. Chem. Phys. 87 (1987) 5606.
[75] B.M. Hoffman, V.J. DeRose, P.E. Doan, R.J. Gubriel, A.L.P. Houseman, J. Telser, in: L.J. Berliner, J. Reuben (Eds.), Biological Magnetic Resonance, vol. 13, Plenum Press, New York, 1993, pp. 208–213.
[76] D. Goldfarb, J.-M. Fauth, Y. Tor, A. Shanzer, J. Am. Chem. Soc. 113 (1991) 1941.
[77] G.C. Hurst, T.A. Henderson, R.W. Kreilick, J. Am. Chem. Soc. 107 (1985) 7294.
[78] D.J. Singel, in: A.J. Hoff (Ed.), Advanced EPR: Applications in Biology and Biochemistry, Elsevier, Amsterdam, 1989, pp. 119–133.
[79] A. Lai, H.L. Flanagan, D.J. Singel, J. Chem. Phys. 89 (1988) 7161.
[80] A.M. Tyryshkin, S.A. Dikanov, E.J. Reijerse, J. Magn. Res. A 116 (1995) 10.
[81] Y. Deligiannakis, L. Astrakas, G. Kordas, R. Smith, Phys. Rev B 58 (1998) 11420.
[82] K. Matar, D. Goldfarb, J. Chem. Phys. 96 (1992) 6464.
[83] R.G. Larsen, C.J. Halkides, D.J. Singel, J. Chem. Phys. 98 (1993) 6704.
[84] W.B. Mims, J. Peisach, J. Chem. Phys. 69 (1978) 4921.
[85] A.V. Astashkin, S.A. Dikanov, Yu.D. Tsvetkov, J. Struct. Chem. 25 (1984) 45.
[86] Y. Deligiannakis, A.W. Rutherford, J. Am. Chem. Soc. 119 (1997) 4471.
[87] S.A. Dikanov, L. Xun, A.B. Karpiel, A.M. Tyryshkin, M.K. Bowman, J. Am. Chem. Soc. 118 (1996) 8406.
[88] S.A. Dikanov, C. Burgard, J. Hüttermann, Chem. Phys. Lett. 212 (1993) 493.
[89] H.L. Van Camp, R.H. Sands, J.A. Fee, J. Chem. Phys. 75 (1981) 2098.
[90] H.J. Sholl, J. Hüttermann, J. Phys. Chem. 96 (1992) 9684.
[91] J. Jeener, Ampére International Summer School, Basko Polje, Yogoslavia, 1971.
[92] J.J. Shane, Dissertation, University of Nijmegen, 1993.
[93] S.A. Dikanov, M.K. Bowman, J. Magn. Res. A 116 (1995) 128.
[94] A. Pöppl, L. Kevan, J. Phys. Chem. 100 (1996) 3387.
[95] L. Astrakas, Y. Deligiannakis, G. Mitrikas, G. Kordas, J. Chem. Phys. 109 (1998) 8692.
[96] J.I. Martinez, P.J. Alonso, C.G. Moreno, M. Medina, Biochemistry 36 (1997) 15526.
[97] H. Käss, J. Rautter, P. Höffer, W. Lubitz, J. Phys. Chem. 99 (1995) 436.
[98] S.A. Dikanov, R.M. Davidov, A. Gräslund, M.K. Bowman, J. Am. Chem. Soc. 120 (1998) 6797.
[99] C.J. Bender, A.C. Rozenweig, S.J. Lippard, J. Peisach, J. Biol. Chem. 269 (1994) 15993.
[100] S.A. Dikanov, M.K. Bowman, J. Biol. Inorg. Chem. 3 (1998) 18.
[101] A. Poppl, R. Bottcher, G. Volkel, J. Magn. Res. A 120 (1996) 214.
[102] D. Goldfarb, V. Kofman, J. Libman, A. Shanzer, R. Rahmatouline, S. VanDoorslaer, A. Schweiger, J. Am. Chem. Soc. 120 (1998) 7020.
[103] T.-L. Lin, Chem. Rev. 84 (1984) 1.
[104] A. DeGroot, R. Evelo, A.J. Hoff, J. Magn. Res. 66 (1986) 331.
[105] P. Dorlet, M. Di Valentin, G.T. Babcock, J.L. McCracken, J. Phys. Chem. 102 (1998) 8239.
[106] V. DeRose, C.-H. Kim, W.E. Newton, D.R. Dean, B.M. Hoffman, Biochemistry 34 (1995) 2809.
[107] Y. Deligiannakis, N. Ioannidis, V. Petrouleas, in: G. Garab (Ed.), Photosynthesis: Mechanisms and Effects, vol. II, Kluwer Academic, Dordrecht, 1998, p. 1233.
[108] S.S. Eaton, J. Dubach, G.R. Eaton, G. Thurman, D.R. Ambruso, J. Biol. Chem. 265 (1990) 7138.
[109] G.W. Ludwig, H.H. Woodbury, in: F. Seitz, D. Turnbull (Eds.), Solid State Physics, vol. 13, Academic Press, New York, 1962, p. 277.
[110] A.E. True, M.N. Nelson, R.A. Venters, W.H. Orme-Johnson, B.M. Hoffmann, J. Am. Chem. Soc. 110 (1988) 1935.
[111] A.R. Coffino, J. Peisach, J. Chem. Phys. 97 (1992) 3072.
[112] B. Bleaney, H.E.D. Scovil, Philos. Mag. 43 (1952) 999.
[113] S. Griffith, Phys. Rev. 132 (1963) 316.
[114] M.P. Hendrich, M.P. Debruner, Biophys. J. 56 (1989) 489.
[115] K.K. Surreus, M.P. Hendrich, P.D. Christie, D. Rottgerd, W.H. Orme-Johnson, E. Münk, J. Am. Chem. Soc. 114 (1992) 8579.
[116] B.M. Hoffman, J. Phys. Chem. 98 (1994) 11657.

[117] B.M. Hoffman, E. Sturgeon, P.E. Doan, V.J. DeRose, K.E. Lieu, S.J. Lippard, J. Am. Chem. Soc. 116 (1994) 6023.
[118] E. Sturgeon, P.E. Doan, K.E. Lieu, D. Burdi, W.H. Tong, J.M. Nocek, N. Gupta, J. Stubbe, D.M. Kurtz, S.J. Lippard, B.M. Hoffman, J. Am. Chem. Soc. 119 (1997) 375.
[119] P.A. Snetsinger, J.B. Cornelius, R.B. Clarkson, M.K. Bowman, R.L. Belford, J. Phys. Chem. 92 (1988) 3696.
[120] C.J. Halkides, C. Farar, R.G. Larsen, A.G. Redfield, D.J. Singel, Biochemistry 33 (1994) 4019.
[121] P.A. Tipton, J. McCracken, J.B. Cornellius, J. Peisach, Biochemistry 28 (1989) 5720.
[122] J. Dubach, S.S. Eaton, G.R. Eaton, Biophys. J. 59 (1991) 1092.
[123] S.S. Eaton, J. Dubach, K.M. More, G.R. Eaton, G. Thurman, D.R. Ambruso, J. Biol. Chem. 264 (1989) 4776.
[124] J. Zweier, P. Aisen, J. Peisach, W.B. Mims, J. Biol. Chem. 254 (1979) 3512.
[125] J. Zweier, J. Peisach, W.B. Mims, J. Biol. Chem. 257 (1982) 10314.
[126] K.O. Schafer, R. Bittl, W. Zweygart, F. Lentzian, G. Haselorst, T. Weyhermuller, K. Wieghardt, W. Lubitz, J. Am. Chem. Soc. 120 (1998) 13104.
[127] C.E. Sass, L. Kevan, J. Phys. Chem. 92 (1988) 5192.
[128] H. Thomann, H. Kim, C. Chiu, L.R. Dalton, B.H. Robinson, Mol. Cryst. Liq. Cryst. 117 (1985) 455.
[129] S. Turconi, D. MacLachlan, P.J. Bratt, J.H.A. Nugent, M.C.W. Evans, Biochemistry 36 (1997) 897.
[130] H. Thoman, M. Bernardo, D. Goldfard, P.M.H. Kroneck, V. Ulltich, J. Am. Chem. Soc. 117 (1995) 8243.
[131] R. LoBrutto, G.W. Smithers, G.H. Reed, W.H. Orme-Johnson, S.L. Tan, J.S. Lee Jr., Biochemistry 25 (1986) 5654.
[132] R.S. Magliozzo, J. McCracken, J. Peisach, Biochemistry 26 (1987) 7923.
[133] C.D. Eads, R. LoBrutto, A. Kumar, J.J. Villafranca, Biochemistry 27 (1988) 165.
[134] S.A. Dikanov, R.I. Samoilova, J.A. Smieja, M.K. Bowman, J. Am. Chem. Soc. 117 (1995) 10579.
[135] S.A. Dikanov, A.P. Spoyalov, J. Hüttermann, J. Chem. Phys. 100 (1994) 7973.
[136] G.J. Gerfen, D.J. Singel, J. Chem. Phys. 100 (1994) 4127.
[137] J.B. Cornelius, J. McCracken, R.B. Clarkson, R.L. Belford, J. Peisach, J. Phys. Chem. 94 (1990) 6977.
[138] C. Zhang, G.D. Markham, R. LoBrutto, Biochemistry 32 (1993) 9866.
[139] Y. Deligiannakis, A. Boussac, H. Bottin, V. Perrier, O. Barzu, A.-M. Gilles, Biochemistry 36 (1997) 9446.
[140] X.-S. Tang, B.A. Diner, B. Larsen, M.L. Gilchrist Jr., G.A. Lorrigan, R.D. Britt, Proc. Nat. Acad. Sci. USA 91 (1994) 704.
[141] V.J. DeRose, V.K. Yachandra, A.E. McDermott, R.D. Britt, K. Sauer, M.P. Klein, Biochemistry 30 (1991) 1335.
[142] J.-L. Zimmermann, A. Boussac, A.W. Rutherford, Biochemistry 32 (1993) 4831.
[143] J. Hanley, Y. Deligiannakis, F. MacMillan, H. Bottin, A.W. Rutherord, Biochemistry 36 (1997) 11543.
[144] M. Mac, N.R. Bowlby, G.T. Babcock, J. McCracken, J. Am. Chem. Soc. 120 (1998) 13215.
[145] S.J. Elliot, D.W. Randal, R.D. Britt, S.I. Chan, J. Am. Chem. Soc. 120 (1998) 3247.
[146] R.G. Larsen, C. Halkides, A.G. Redfield, D.J. Singel, J. Am. Chem. Soc. 114 (1992) 9608.
[147] R.G. Larsen, G.J. Gerfen, D.J. Singel, Appl. Magn. Res. 3 (1992) 369.
[148] H. Thomman, M. Beranrdo, J.M. McCormick, S. Pulver, K.K. Andersson, J.D. Lipscomb, E.I. Solomon, J. Am. Chem. Soc. 115 (1993) 8881.
[149] R.G. Evelo, A.J. Hoff, S.A. Dikanov, Chem. Phys. Lett. 157 (1989) 25.
[150] T.F. Prisner, Adv. Magn. Res. 20 (1998) 245.
[151] J.W.A. Coremans, O.G. Poluektov, E.J.J. Groenen, G.W. Canters, H. Nar, A. Messerschmidt, J. Am. Chem. Soc. 119 (1997) 4726.
[152] N.W. Atherton, Principles of Electron Spin Resonsnce, Elis Horwood/Prentice Hall, London, 1993 (Chapter 5).
[153] P.A. Snetsinger, N.D. Chasteen, H.V. Milligen, J. Am. Chem. Soc. 112 (1990) 8155.

[154] C.P. Scholes, A. Lapidot, R. Mascarenhas, T. Inubushi, R.A. Isaacson, G. Feher, J. Am. Chem. Soc. 104 (1982) 2724.
[155] W.B. Mims, J. Peisach, J.L. Davis, J. Chem. Phys. 66 (1977) 5536.
[156] R. Magliozzo, J. Peisach, Biochemistry 32 (1993) 8446.
[157] J.R. Morton, K.F. Preston, J. Magn. Res. 30 (1978) 577.
[158] C.H. Towens, B.P. Dailey, J. Chem. Phys. 17 (1949) 782.
[159] E.A. Lucken, Nuclear Quadruple Coupling Constants, Academic Press, New York, 1969.
[160] I.H. Ashby, C.P. Cheng, T.L. Brown, J. Am. Chem. Soc. 100 (1978) 6057.
[161] F. Jiang, J. McCracken, J. Peisach, J. Am. Chem. Soc. 112 (1990) 9035.
[162] F. Jiang, K.D. Karlin, J. Peisach, Inorg. Chem. 32 (1993) 2576.
[163] V. Kofman, S.A. Dikanov, A. Haran, J. Libman, A. Shanzer, D. Goldfarb, J. Am. Chem. Soc. 117 (1995) 383.
[164] M.J. Colaneri, J. Peisach, J. Am. Chem. Soc. 114 (1992) 5335.
[165] J. McCracken, S. Pember, S.J. Benkovic, J.J. Villafranca, R.J. Miller, J. Peisach, J. Am. Chem. Soc. 110 (1988) 1069.
[166] S.J. Lippard, J.M. Berg, Principles of Bioinorganic Chemistry, University Science Books, Mill Valey, CA, 1994.
[167] R.H. Holm, P. Kennepohl, E.I. Solomon, Chem. Rev. 96 (1996) 2239.
[168] K.D. Karlin, Z. Tyeklar (Eds.), Bioinorganic Chemistry of Copper, Chapman and Hall, New York, 1993.
[169] E.I. Solomon, A.A. Gewrith, T.D. Westmoreland, in: A.J. Hoff (Ed.), Advanced EPR, Applications in Biology and Biochemistry, Elsevier, Amsterdam, 1989 (Chapter 25).
[170] J. Peisach, in: K.D. Karlin, Z. Tyeklar (Eds.), Bioinorganic Chemistry of Copper, Chapman and Hall, New York, 1993, pp. 21–33.
[171] M.J. Colaneri, J.A. Potenza, H.J. Schugar, J. Peisach, J. Am. Chem. Soc. 112 (1990) 9451.
[172] F. Jiang, J. Peisach, Inorg. Chem. 33 (1994) 1348.
[173] F. Jiang, J. Peisach, L.-J. Ming, L. Que, V.J. Chen, Biochemistry 30 (1991) 11437.
[174] M. Romanelli, R. Basosi, Chem. Phys. Lett. 143 (1988) 404.
[175] M. Louloudi, Y. Deligiannakis, N. Hadjiliadis, Inorg. Chem. 37 (1998) 6847.
[176] M. Louloudi, Y. Deligiannakis, J.P. Tuchagues, B. Donnadieu, N. Hadjiliadis, Inorg. Chem. 36 (1997) 6335.
[177] F. Jiang, R.R. Conry, L. Bubacco, Z. Tyeklar, R.R. Jacobson, K.D. Karlin, J. Peisach, J. Am. Chem. Soc. 115 (1993) 2093.
[178] P.M. Schosseler, B. Wehrli, A. Schweiger, Inorg. Chem. 36 (1997) 4490.
[179] V. Kofman, J.J. Shane, S.A. Dikanov, M.K. Bowman, J. Libman, A. Shanzer, D. Goldfarb, J. Am. Chem. Soc. 117 (1995) 12771.
[180] C.P. Keizers, D. Smaathrost, Chem. Phys. Lett. 69 (1980) 348.
[181] R. Krimse, J. Stach, U. Abram, W. Dietzch, R. Böttcher, M.C.M. Grinbau, C.P. Keijers, Inorg. Chem. 23 (1984) 3333.
[182] J.A. Tainer, E.D. Getzoff, K.M. Beem, J.S. Richardson, D.C. Richardson, J. Mol. Biol. 160 (1982) 181.
[183] J.A. Fee, J. Peisach, W.B. Mims, J. Biol. Chem. 256 (1981) 1910.
[184] R. Gubriel, R. Peoples, P.E. Doan, J.F. Cline, J. McCracken, J. Peisach, B.M. Hoffman, J.S. Valentine, Inorg. Chem. 32 (1993) 1813.
[185] A. Messerschmidt, A. Rossi, R. Ladenstein, R. Huber, M. Bolognesi, G. Gartti, A. Marchesini, R. Petruzzelli, A. Finazzi-Agro, J. Mol. Biol. 206 (1989) 513.
[186] B. Mondovi, M.T. Graziani, W.B. Mims, J. Peisach, Biochemistry 16 (1977) 4198.
[187] L. Avigliano, J.L. Davis, M.T. Graziani, A. Marchesini, W.B. Mims, B. Mondovi, J. Peisach, FEBS Lett. 136 (1981) 80.
[188] J. Lu, C.J. Bender, J. McCracken, J. Peisach, J.C. Severns, D.R. McMillin, Biochemistry 31 (1992) 6265.

[189] D. Goldfarb, J.-M. Fauth, O. Farver, I. Pecht, Appl. Magn. Res. 3 (1992) 333.
[190] J. McCracken, P.R. Desai, N. Papadopoulos, J. Villafranca, J. Peisach, J. Am. Chem. Soc. 27 (1988) 4133.
[191] S. Balasubramanian, R.T. Carr, C.J. Bemder, J. Peisach, S.J. Benkovic, Biochemistry 33 (1994) 8532.
[192] D.J. Kosman, J. Peisach, W.B. Mims, Biochemistry 19 (1980) 1304.
[193] H. Thomann, M. Bernardo, M.J. Baldwin, M.D. Lowery, E.I. Solomon, J. Am. Chem. Soc. 113 (1991) 5913.
[194] W.B. Mims, J. Peisach, Biochemistry 15 (1976) 3863.
[195] W.B. Mims, J. Peisach, J. Biol. Chem. 254 (1979) 4321.
[196] C.J. Bender, J. Peisach, J. Chem. Soc. Faraday Trans. 94 (1998) 375.
[197] A. Messerschmidt, R. Ladenstein, R. Huber, M. Bolognesi, L. Avigliano, R. Petruzzelli, A. Rossi, A. Finazzi-Agro, J. Mol. Biol. 224 (1992) 179.
[198] H. Nar, A. Messerschmidt, R. Huber, M. van de Kamp, G.W. Canters, J. Mol. Biol. 221 (1991) 765.
[199] V. Kofman, O. Farver, I. Pecht, D. Goldfarb, J. Am. Chem. Soc. 118 (1996) 1201.
[200] J.W.A. Coremans, M. vanGastel, O.G. Poluektov, E.J.J. Groenen, T. denBlaauwen, G. van Pouderoyen, G.W. Canters, H. Nar, C. Hammann, A. Messerschmidt, Chem. Phys. Lett. 235 (1995) 202.
[201] R.L. Walter, S.H. Halick, A.M. Friedman, R.C. Blake, H.P. Proctor, M. Stoham, J. Mol. Biol. 263 (1996) 730.
[202] C.J. Bender, D.R. Casimiro, J. Peisach, H.J. Dyson, J. Chem. Soc. Faraday Trans. 93 (1997) 3967.
[203] M. Wikström, Nature 266 (1977) 271.
[204] S.I. Chan, P.M. Li, Biochemistry 29 (1990) 1.
[205] R.J. Gurbiel, Y.C. Fann, K.K. Surerus, M.M. Werst, S.M. Musser, P.E. Doan, S.I. Chan, J.A. Fee, B.M. Hoffman, J. Am. Chem. Soc. 115 (1993) 10888.
[206] A.P. Hansen, R.D. Britt, M.P. Klein, C.J. Bender, G.T. Babcock, Biochemistry 32 (1993) 13718.
[207] D.H. Ellerton, N.F. Ellerton, H.A. Robinson, Prog. Biophys. Mol. Biol. 41 (1983) 143.
[208] B. Linzen, N.M. Soeter, A.F. Riggs, H.J. Schneider, W. Shartau, M.D. Moore, E. Yocota, P.Q. Behrens, H. Nakashima, T. Takagi, T. Nemoto, H.J. Verijken, H.J. Bak, A. Beintema, A. Volbeda, W.P.J. Gaykema, W.G.J. Hol, Science 229 (1985) 519.
[209] R.S. Magliozzo, L. Bubacco, J. McCracken, F. Jiang, M. Beltramini, B. Salvato, J. Peisach, Biochemistry 34 (1995) 1513.
[210] L. Bubacco, R.S. Magliozzo, M.D. Wirt, M. Beltramini, B. Salvato, J. Peisach, Biochemistry 34 (1995) 1524.
[211] B.A. Springer, S.G. Sligar, J.S. Olson, G.N. Philips, Chem. Rev. 94 (1994) 699.
[212] M. Momentau, C.A. Reed, Chem. Rev. 94 (1994) 659.
[213] J. Peisach, W.B. Mims, J.L. Davis, J. Biol. Chem. 254 (1979) 12379.
[214] R.S. Magliozzo, J. Peisach, Biochemistry 31 (1992) 189.
[215] R.S. Magliozzo, J. McCracken, J. Peisach, Biochemistry 26 (1987) 7923.
[216] R. LoBrutto, Y.-H. Wei, R. Mascarenhas, C.P. Scholes, T.F. King, J. Biol. Chem. 258 (1983) 7437.
[217] T.G. Brown, B.M. Hoffman, Mol. Phys. 39 (1980) 1073.
[218] T. Harami, J. Chem. Phys. 71 (1979) 1309.
[219] J.L. Theodorakis, E.A.E. Gerber, J. McCracken, J. Peisach, A. Schejter, E. Margoliash, Biochim. Biophys. Acta 1252 (1995) 103.
[220] S.E. Groth, A. Nagashisa, S.L. Tan, W.H. Orme-Johnson, J. Am. Chem. Soc. 105 (1983) 7445.
[221] D. Goldfarb, M. Bernardo, H. Thomann, P.M.H. Kroneck, V. Ullrich, J. Am. Chem. Soc. 118 (1996) 2686.
[222] H. Aissaoui, R. Bachmann, A. Schweiger, W.-D. Woggon, Angew. Chem. Int. Ed. Engl. 37 (1998) 2998.

[223] D. Chasteen, Adv. Inorg. Chem. 5 (1983) 210.
[224] B.F. Anderson, H.M. Baker, E.J. Donson, G.E. Norris, S.V. Rumbal, J.M. Watters, E.N. Bakers, Proc. Nat. Acad. Sci. USA 84 (1987) 1769.
[225] S. Bailey, R.W. Evans, R.C. Garrat, B. Gorinsky, S. Hasnain, C. Horsdurgh, H. Jhoti, P.F. Lindley, A. Mudin, R. Sarra, J.L. Watson, Biochemistry 27 (1988) 5804.
[226] G.W. Bates, M.R. Schlabach, J. Biol. Chem. 250 (1975) 2177.
[227] J.E. Roberts, T.G. Brown, B.M. Hoffman, P. Aisen, Biochim. Biophys. Acta 747 (1983) 49.
[228] S.K. Swope, N.D. Chasteen, K.E. Weber, D.C. Harris, J. Am. Chem. Soc. 110 (1988) 3855.
[229] P.A. Snetsinger, N.D. Chasteen, J.B. Cornellius, D.J. Singel, J. Phys. Chem. 96 (1992) 7917.
[230] V. Petrouleas, B.A. Diner, Biochim. Biophys. Acta 1015 (1990) 131.
[231] A.L Feig, S.L. Lippard, Chem. Rev. 94 (1994) 759.
[232] R.E. Stencamp, Chem. Rev. 106 (1994) 715.
[233] B.C. Antanaidis, J. Peisach, W.M. Mims, P. Aisen, J. Biol. Chem. 260 (1985) 4572.
[234] K. Doi, J. McCracken, J. Peisach, P. Aisen, J. Biol. Chem. 263 (1988) 5757.
[235] R. Cammack, in: R. Cammack, A.G. Sykes (Eds.), Advances in Inorganic Chemisrty: Iron Sulfur Proteins, Academic Press, San Diego, CA, 1992, pp. 281–322.
[236] R.D. Britt, K. Sauer, M.P. Klein, D.B. Knaff, A. Kriacunas, C.A. Yu, L. Yu, R. Malkin, Biochemistry 30 (1991) 1892.
[237] J.K. Shergill, R. Cammack, Biochim. Biophys. Acta 1185 (1994) 35.
[238] J.K. Shergill, C.L. Joannou, J.R. Mason, R. Cammack, Biochemistry 34 (1995) 16533.
[239] R. Cammack, A. Chapman, J. McCracken, J.B. Cornelius, J. Peisach, J.H. Weiner, Biochim. Biophys. Acta 956 (1988) 307.
[240] R. Cammack, A. Chapman, J. McCracken, J. Peisach, J. Chem. Soc. Faraday Trans. 87 (1991) 3203.
[241] J.K. Shergill, R. Cammack, J.H. Weiner, J. Chem. Soc. Faraday Trans. 87 (1991) 3199.
[242] J.K. Shergill, R. Cammack, Biochim. Biophys. Acta 1185 (1994) 43.
[243] A. Dikanov, A.M. Tyryshkin, I. Felli, E.J. Reijerse, J. Hüttermann, J. Magn. Res. Ser. B 108 (1995) 99.
[244] A. Riedel, S. Fentzner, M. Rampp, F. Lingens, U. Liebl, J.L. Zimmermann, W. Nitchke, J. Biol. Chem. 270 (1995) 30869.
[245] J.K. Shergill, M.-P. Gollineli, R. Cammack, J. Meyer, Biochemistry 35 (1996) 12842.
[246] S.A. Dikanov, R.M. Davydov, L. Xun, M.K. Bowman, J. Magn. Res. Ser. B 112 (1996) 289.
[247] J.F. Cline, B.M. Hoffman, W.B. Mims, E. LaHaie, D.P. Ballou, J.A. Fee, J. Biol. Chem. 260 (1985) 3251.
[248] H. Thomann, M. Berardo, M.W.W. Adams, J. Am. Chem. Soc. 113 (1991) 7044.
[249] M. Kumar, W.-P. Lu, A. Smith, S.W. Ragsdale, J. McCracken, J. Am. Chem. Soc. 117 (1995) 2929.
[250] B.K. Burges, D.L. Lowe, Chem. Rev. 96 (1996) 2983.
[251] J.B. Howard, D.C. Rees, Chem. Rev. 96 (1996) 260.
[252] T.V. Morgan, J. McCracken, W.H. Orme-Johnson, W.B. Mims, L.E. Mortenson, J. Peisach, Biochemistry 29 (1990) 3077.
[253] H. Thomann, T.V. Morgan, H. Jin, S.J.N. Burgmayer, R.E. Bare, E.I. Stiefel, J. Am. Chem. Soc. 109 (1987) 7913.
[254] H. Thomann, M. Bernardo, W.E. Newton, D.R. Dean, Proc. Nat. Acad. Sci. USA 88 (1991) 6620.
[255] H.-I. Lee, K.S. Thrasher, D.R. Dean, W.E. Newton, B.M. Hoffman, Biochemistry 37 (1998) 13370.
[256] W.R. Hagen, W.A.M. van den Berg, W.M.A.M. van Dongen, E.J. Reijerse, P.J.M. van Ken, J. Chem. Soc. Faraday Trans. 94 (1998) 2969.
[257] R. Hille, Chem. Rev. 96 (1996) 2757.
[258] A.P. Pacheco, P. Basu, P. Borbat, A.M. Raitsimring, J. Enemark, Inorg. Chem. 35 (1996) 7001.
[259] A.M. Raitsimring, A. Pachenco, J.H. Enemark, J. Am. Chem. Soc. 120 (1998) 11263.
[260] G.A. Lorigan, R.D. Britt, J.H. Kim, R. Hille, Biochim. Biophys. Acta 1185 (1994) 284.

[261] N.D. Chasteen, in: L.J. Berliner, J. Reuben (Eds.), Biological Magnetic Resonance, vol. 3, Plenum Press, New York, 1981, pp. 53–119.
[262] J. Ballhausen, H.B. Gray, Inorg. Chem. 1 (1962) 111.
[263] A.V. Astashkin, S.A. Dikanov, Yu.D. Tsvetkov, J. Struct. Chem. 26 (1985) 3.
[264] S. Eaton, G.R. Eaton, in: N.D. Chasteen (Ed.), Vanadium in Biological Systems, Kluwer Academic, Dordrecht, 1990, pp. 199–222.
[265] W. Makinen, D. Mustafi, in: H. Sigel (Ed.), Metal Ions in Biological Systems, vol. 30, Marcel Dekker, New York, 1995, pp. 89–127.
[266] S.A. Dikanov, V.F. Yydanov, Yu.D. Tsvetkov, J. Magn. Res. 34 (1979) 631.
[267] M. Narayana, C.S. Narasimhan, L. Kevan, J. Chem. Soc. Faraday Trans. 81 (1985) 137.
[268] A. Togni, G. Rist, G. Rihs, A. Schweiger, J. Am. Chem. Soc. 115 (1993) 1908.
[269] K.Fukui Ohya-Nishiguchi, H. Kamada, J. Phys. Chem. 97 (1993) 1185.
[270] K. Fukui, O. Nishiguchi, H. Kamada, Inorg. Chem. 36 (1997) 5518.
[271] K. Fukui, H. Ohya-Nishiguchi, H. Kamada, Inorg. Chem. 38 (1998) 2326.
[272] R. LoBrutto, B.J. Hamstra, G.L. Colpas, V.L. Pecoraro, W.D. Frash, J. Am. Chem. Soc. 120 (1998) 4410.
[273] E.J. Reijerse, A.M. Tyryshkin, S.A. Dikanov, J. Magn. Res. 131 (1998) 295.
[274] E.J. Reijerse, J.J. Shane, E. deBoer, D. Collison, in: N.D. Yudanov (Ed.), Electron Magnetic Resonance of Disordered Systems, World Scientific, Singapore, 1989, p. 189.
[275] H.L. Flanagan, D.J. Singel, J. Chem. Phys. 89 (1988) 2585.
[276] A.L.P. Houseman, R. LoBrutto, W.D. Frash, Biochemistry 34 (1995) 3277.
[277] J. Petersen, T.R. Hawkes, D.J. Lowe, J. Am. Chem. Soc. 42 (1998) 10972.
[278] A. Messerschmidt, R. Wever, Proc. Nat. Acad. Sci. USA 93 (1996) 392.
[279] E. deBoer, C. Keizers, A.A.K. Klaasen, E.J. Reijerse, D. Collison, C.D. Garner, R. Wever, FEBS Lett. 235 (1988) 93.
[280] B.J. Hamstra, A.L.P. Houseman, G.J. Colpas, J.W. Kampf, R. LoBrutto, W.D. Frash, V.L. Pecoraro, Inorg. Chem. 36 (1997) 4866.
[281] A. Hauseman, L. Morgan, R. LoBrutto, W.D. Frash, Biochemistry 33 (1994) 4910.
[282] C. Buy, T. Matsui, S. Rianambininstoa, C. Sigalat, G. Girault, J.L. Zimmermann, Biochemistry 35 (1996) 14281.
[283] R.R. Crichton, Struct. Bonding 17 (1973) 66.
[284] W.P. Chen, Process Biochem. 15 (1980) 30.
[285] H.-H.T. Nguyen, K.H. Nakagawa, B. Hedman, S.J. Elliot, M.E. Lidstrom, K.O. Hodgson, S.I. Chan, J. Am. Chem. Soc. 118 (1996) 12766.
[286] K. Fukui, H. Ohya-Nishiguchi, M. Nakai, H. Sakurai, H. Kamada, FEBS Lett. 368 (1995) 31.
[287] B.M. Hoffman, D.H. Petering, Proc. Nat. Acad. Sci. USA 67 (1970) 637.
[288] H. Lee, M. Ikea-Saito, T. Yonetani, R.S. Magliozo, J. Peisach, Biochemistry 31 (1992) 7274.
[289] H.C. Lee, J.B. Wittenberg, J. Peisach, Biochemistry 32 (1993) 11500.
[290] H.C. Lee, J. Peisach, Y. Dou, M. Ikeda-Saito, Biochemistry 33 (1994) 7609.
[291] H.C. Lee, J. Peisach, A. Tsuneshige, T. Yonaetani, Biochemistry 34 (1995) 6883.
[292] H.C. Lee, E. Scheuring, J. Peisach, M.R. Chance, J. Am. Chem. Soc. 119 (1997) 12201.
[293] M.D. Wirt, C. Bender, J. Peisach, Inorg. Chem. 34 (1995) 1663.
[294] P.C. Kang, G.R. Eaton, S.S. Eaton, Inorg. Chem. 34 (1994) 3660.
[295] B.S. Tvorog, D.J. Kitko, R.S. Drago, J. Am. Chem. Soc. 98 (1976) 5144.
[296] B.B. Wayland, M.E. Abd-Elmageed, J. Am. Chem. Soc. 98 (1974) 4809.
[297] B. Shanaan, J. Mol. Biol. 171 (1983) 31.
[298] K. Imai, M. Ikeda-Saito, H. Yamamoto, T. Yonetani, J. Biol. Chem. 138 (1980) 635.
[299] C.A. Reed, S.K. Cheung, Proc. Nat. Acad. Sci. USA 74 (1977) 1780.
[300] H. Umezawa, in: S.M. Hecht (Ed.), Bleomycin, Springer–Verlag, New–York, 1979, pp. 24–36.
[301] R.M. Burger, A.D. Adler, S.B. Horwitz, W.B. Mims, J. Peisach, Biochemistry 20 (1981) 1701.
[302] E.H. Serpescu, J. McCracken, J. Peisach, A.S. Mildvan, Biochemistry 27 (1988) 8034.

[303] Z. Levi, A.M. Raitsimring, D. Goldfarb, J. Phys. Chem. 95 (1991) 7831.
[304] P.A. Tipton, T.P. Quinn, J. Peisach, P.F. Cook, Protein Sci. 5 (1996) 1648.
[305] M.P. Espe, J.P. Hosler, S. Ferguson-Miller, G.T. Babcock, J. McCracken, Biochemistry 34 (1995) 7593.
[306] J. McCracken, J. Peisach, L. Bhattacharyya, F. Brewer, Biochemistry 30 (1991) 4486.
[307] J.P. Hosler, M.P. Espe, M.P. Zhen, G.T. Babcock, S. Ferguson-Miller, Biochemistry 34 (1995) 7586.
[308] P.A. Tipton, J. Peisach, Biochemistry 30 (1991) 739.
[309] C. Buy, G. Girault, J.-L. Zimmermann, Biochemistry 35 (1996) 9880.
[310] K.D. Hardman, R.C. Agarwal, M.J. Freiser, J. Mol. Biol. 157 (1982) 69.
[311] J.A. Grand, D. Owen, Biochem. J. 279 (1991) 609.
[312] R.G. Larsen, C.J. Halkides, A.G. Redfield, D.J. Singel, J.Am. Chem. Soc. 114 (1992) 9608.
[313] C.T. Farrar, C.J. Halkides, D.J. Singel, Struture 5 (1997) 1055.
[314] C.J. Halkides, C.T. Farrar, D.J. Singel, J. Magn. Res. 134 (1998) 142.
[315] R.J. Almassy, C.A. Janson, R. Hamlin, N.-H. Xuong, D. Eisenberg, Nature (London) 323 (1986) 304.
[316] G.C. Dismukes, Chem. Rev. 96 (1996) 2909.
[317] V.K. Yachandra, K. Sauer, M.P. Klein, Chem. Rev. 96 (1996) 2927.
[318] D.W. Randall, A. Gelasco, M.T. Caudle, V.L. Pecoraro, R.D. Britt, J. Am. Chem. Soc. 119 (1997) 4481.
[319] Y.-M. Frapard, A. Boussac, R. Albach, E. Anxolabehere-Mallard, M. Delroisse, J.-B. Verlhac, G. Blondin, J.-J. Girerd, J. Guilhem, M. Cesario, A.W. Rutherford, D. Lexa, J. Am. Chem. Soc. 116 (1996) 2669.
[320] A. Ivancich, V. Barynin, J. -L. Zimmermann, Biochemistry 34 (1995) 6628.
[321] J.E. Penner-Hahn, in: V.L. Pecoraro (Ed.), Manganese Redox Enzymes, VCH, New York, 1992, pp. 29–45.
[322] S.A. Dikanov, Y.D. Tsvetkov, S.V. Khangulov, M.G. Goldfeld, Dokl. Akad. Nauk SSSR 302 (1988) 1255.
[323] R.D. Britt, J.-L. Zimmermann, K. Sauer, M.P. Klein, J. Am. Chem. Soc. 111 (1989) 3522.
[324] K. Warncke, G.T. Babcock, J. McCracken, J. Am. Chem. Soc. 116 (1994) 7332.
[325] C. Tommos, X.-S. Tang, K. Warnke, C.W. Hoganson, S. Styring, J. McCracken, G.T. Babcock, J. Am. Chem. Soc. 117 (1995) 10325.
[326] A.V. Astashkin, A. Kawamori, Y. Kodera, S. Kuroiwa, K. Akabori, J. Chem. Phys. 102 (1995) 5583.
[327] Y. Deligiannakis, C. Jegerschold, A.W. Rutherford, Chem. Phys. Lett. 270 (1997) 564.
[328] A.V. Astashkin, S. Kuroia, A. Kawamori, K. Akabori, J. Chem. Phys. 108 (1998) 10143.
[329] A.W. Rutherford, Trends Biol. Sci. 14 (1989) 227.
[330] A. Boussac, Chem. Phys. 194 (1995) 409.
[331] A. Boussac, Y. Deligiannakis, A.W. Rutherford, in: G. Garab (Ed.), Photosynthesis: Mechanisms and Effects, vol. II, Kluwer Academic, Dordrecht, 1998, p. 1117.
[332] D.A. Force, D.W. Randall, G.A. Lorigan, K.L. Clemens, R.D. Britt, J. Am. Chem. Soc. 120 (1998) 13321.
[333] A. Boussac, A.W. Rutherford, Biochem. Soc. Trans. 22 (1994) 352.
[334] J. Sarrou, N. Ioannidis, Y. Deligiannakis, V. Petrouleas, Biochemistry 37 (1998) 3581.
[335] J. Messinger, J.H.A. Nugent, M.C.W. Evans, Biochemistry 36 (1997) 11055.
[336] K.A. Ahrling, S. Peterson, S. Styring, Biochemistry 36 (1997) 13148.
[337] A. Boussac, J.-L. Zimmermann, A.W. Rutherford, Nature 347 (1990) 303.
[338] A. Boussac, A.W. Rutherford, Biochemistry 31 (1992) 7441.
[339] M.L. Gilchrist, J.A. Bail, D.W. Randall, R.D. Britt, Proc. Nat. Acad. Sci. 92 (1995) 9545.
[340] X.-S. Tang, D.W. Randall, D.A. Force, B.A. Diner, R.D. Britt, J. Am. Chem. Soc. 118 (1996) 7638.
[341] D.A. Force, D.W. Randall, R.D. Britt, Biochemistry 36 (1997) 12062.
[342] C. Tommos, J. McCracken, S. Styring, G.T. Babcock, J. Am. Chem. Soc. 120 (1998) 10441.
[343] J.C. Salerno, The Bioinorganic Chemistry of Nickel, VCH, New York, 1988 (Chapter 3).
[344] J. McCracken, S. Friedberg, J. Phys. Chem. 98 (1994) 467.

[345] J.E. Huyett, S.B. Choudhury, D.M. Eichhorn, P.A. Bryngelson, M.J. Maroney, B.M. Hoffman, Inorg. Chem. 37 (1998) 1361.
[346] A. Chapman, R. Cammack, C.E. Hatchikian, J. McCracken, J. Peisach, FEBS Lett. 242 (1988) 134.
[347] R. Cammack, K.L. Kovacs, J. McCracken, J. Peisach, Eur. J. Biochem. 182 (1989) 363.
[348] S.L. Tan, J.A. Fox, N. Kojima, C.T. Walsh, W.H. Orme-Johnson, J. Am. Chem. Soc. 106 (1984) 3064.
[349] H. Tachikawa, T. Ichikawa, H. Yoshida, J. Am. Chem. Soc. 112 (1990) 977.
[350] E.I. Solomon, Y. Zhang, Acc. Chem. Res. 25 (1992) 12409.
[351] C. Ostermeier, A. Harrenga, H. Michel, Proc. Nat. Acad. Sci. USA 94 (1997) 10547.